

# Development of Nanodevices Based on VO<sub>2</sub> Thin Films

zur Erlangung des akademischen Grades

Doktor der Ingenieurwissenschaften

von der KIT-Fakultät für Maschinenbau  
des Karlsruher Instituts für Technologie (KIT)

genehmigte

Dissertation

von

M.Sc. Sanaz Rastjoo

Tag der mündlichen Prüfung: 08. Mai 2020

Erster Gutachter: Prof. Dr. Manfred Kohl

Zweiter Gutachter: Prof. Dr. Alfred Ludwig





This document is licensed under a Creative Commons Attribution-ShareAlike 4.0 International License (CC BY-SA 4.0):  
<https://creativecommons.org/licenses/by-sa/4.0/deed.en>



# Acknowledgments

First, I would like to express my sincere gratitude to my supervisor Prof. Dr Manfred Kohl for giving me the chance to work on the fascinating subject in the field of smart materials and nanodevices. I want to thank him for his scientific support as well as providing me the freedom to develop and pursue my own research ideas, moreover, for giving me the opportunity to present my research on international conferences.

I would like to thank our collaboration partners at Ruhr-Universität Bochum RUB, to Prof. Dr. Alfred Ludwig as the co-supervisor of this thesis, and, to Xiao Wang for deposition of VO<sub>2</sub>-based thin films and interesting discussions.

Many thanks to the previous and present members of the research group FuE1-SMD. My grateful thanks to Daria Kohler, Sandeep Ummethala, Florian Brüderlin, Hinnerk Ossmer and Randy Fechner, not only for their scientific support, also, for being there as precious friends and help me through difficulties.

I thank all the students who have supported me during last years as HiWi or master students.

I would like to thank all technical and administrative staff at the institute of microstructure technology IMT. Especially, Alban Muslija, who helped me in developing a new etching method of VO<sub>2</sub>-based thin films. Furthermore, my thanks to Lothar Hahn and Andreas Bacher for the e-beam lithography process.

Finally, my numerous thanks to my friends and family, especially to Ali Tamizifar for his kind and endless support.



# Abstract

Vanadium dioxide ( $\text{VO}_2$ ) is a multifunctional smart material, which exhibits a reversible martensitic transformation at  $67^\circ\text{C}$ . The transformation is accompanied with an insulator-metal transition as well as drastic changes in optical properties in the infrared- (IR-) wavelength range. This work focuses on three main goals. First, the design, fabrication and evaluation of free-standing  $\text{VO}_2$ -based test devices for systematic studies on size effects. Second, development of first-of-its kind  $\text{VO}_2$ -based nanoactuators. Third, to use this understanding for development of a demonstrator device for application in nanophotonics.

In this work,  $\text{VO}_2$  and  $\text{VMoO}_2$  films are deposited using reactive magnetron sputtering at Ruhr-Universität Bochum (RUB). In order to achieve free-standing  $\text{VO}_2$ -based nanostructures, flexible nanofabrication methods on silicon- (Si-) based substrates are established. Two top-down fabrication processes are presented, in which the substrate is nanomachined either before or after film deposition using electron beam lithography (EBL) and reactive ion etching (RIE). By direct nanomachining of  $\text{VO}_2$ -based films, free-standing nanostructures with lateral widths down to 100 nm are fabricated. Another approach of nanofabrication involves  $\text{VO}_2$  deposition on substrates with Si nanopillars. These processes enable downscaling of  $\text{VO}_2$  structures reaching the scale of grain size and, thus, oligocrystalline configurations.

For electrical characterization, a four-terminal setup is designed inside a thermostat under quasi-stationary conditions. Electrical resistance characteristics of  $\text{VMoO}_2$  nanobridges indicate that the phase transformation persists down to a lateral width of at least 200 nm. However, results show no significant size-dependence of the transition temperature on the lateral width. As a major effect, the electrical resistance drop upon the insulator-metal transition in  $\text{VMoO}_2$  nanobridges is larger compared to a reference film, which increases for decreasing widths. For mechanical characterization, out-of-plane deflection of bi-morph cantilevers are investigated in-situ inside a scanning electron microscope (SEM) either by Joule heating using nanomanipulators or by altering the sample temperature homogeneously using a micro heating-cooling stage. The out-of-plane deflection of Cr/ $\text{VMoO}_2$  nanoactuators reveals the shape memory effect (SME) even for the smallest lateral width of 300 nm. A large relative actuation stroke  $\Delta s/l$  of up to 15 % is observed for nanoactuators with a beam width of 600 nm.

The operation concept of the  $\text{VO}_2$ -based photonic device is to modulate the propagation of light in Si waveguides based on the insulator-metal transition in  $\text{VO}_2$  films. The experimental results from temperature-dependent optical transmission measurements show a reduction in the transmission for the hot (metal) state compared to the cold (insulator) state allowing for *on/off* optical switching.



# Kurzfassung

Vanadiumdioxid ( $\text{VO}_2$ ) ist ein multifunktionales, intelligentes Material, das bei  $67\text{ }^\circ\text{C}$  eine reversible martensitische Phasenumwandlung zeigt. Die Phasenumwandlung geht sowohl mit einem Isolator-Metall-Übergang als auch mit drastischen Änderungen der optischen Eigenschaften im Infrarotbereich einher. Diese Arbeit hat drei Hauptziele: Erstens sollen freistehende  $\text{VO}_2$ -basierte Teststrukturen entworfen, hergestellt und untersucht werden, um mögliche Größeneffekte systematisch zu analysieren. Zweitens sollen neuartige  $\text{VO}_2$ -basierte Nanoaktoren entwickelt werden und drittens soll das gewonnene Verständnis für die Entwicklung eines nanophotonischen Demonstratorgerätes werden.

Im Rahmen dieser Arbeit werden  $\text{VO}_2$ - und  $\text{VMoO}_2$ -Dünnschichten mittels reaktivem Magnetronspütern an der Ruhr-Universität Bochum (RUB) hergestellt. Um freistehende  $\text{VO}_2$ -basierte Nanostrukturen zu erhalten, werden flexible Nanofabrikationsmethoden für Silizium- (Si-) basierte Substrate entwickelt. Es werden zwei Top-Down-Fertigungsverfahren vorgestellt, bei denen das Substrat entweder vor oder nach der Schichtabscheidung mittels Elektronenstrahlolithographie (EBL) und reaktivem Ionenätzen (RIE) nanostrukturiert wird. Durch die direkte Nanostrukturierung von  $\text{VO}_2$ -basierten Dünnschichten können freistehende Nanostrukturen mit lateralen Breiten bis zu  $100\text{ nm}$  hergestellt werden. In einem weiteren Fabrikationsprozess wird  $\text{VO}_2$  auf strukturierten Substraten mit Si-Nanosäulen. Beide Prozesse ermöglichen es  $\text{VO}_2$ -Strukturen, bis auf die Größenordnung der Korngröße zu miniaturisieren und somit oligokristalline Strukturen herzustellen.

Für die elektrische Charakterisierung der  $\text{VO}_2$  Strukturen wird eine Vierleiter-Messanordnung in einem Thermostaten entwickelt, der quasi-stationäre Temperaturbedingungen ermöglicht. Elektrischen Widerstandsmessungen an den  $\text{VMoO}_2$ -Nanobrücken zeigen, dass die Phasenumwandlung mindestens bis zu einer lateralen Breite von  $200\text{ nm}$  auftritt. Die Übergangstemperatur zeigt keine signifikante Größenabhängigkeit von der lateralen Breite. Ein wesentlicher Unterschied der Nanostrukturen im Vergleich zu einer durchgängigen  $\text{VMoO}_2$ -Dünnschicht besteht darin, dass der elektrische Widerstandsabfall beim Isolator-Metall-Übergang in  $\text{VMoO}_2$ -Nanobrücken größer ist. Der Widerstandsabfall erhöht sich mit abnehmender lateraler Breite. Cr/ $\text{VMoO}_2$ -Bimorph-Nanoaktoren werden mechanisch untersucht indem sie in-situ in einem Rasterelektronenmikroskop (REM) einer Temperaturänderung unterworfen werden und dabei die Auslenkung gemessen wird. Die Temperaturänderung wird entweder durch Joulesche Wärme mit Hilfe von Nanomanipulatoren erreicht, oder durch eine homogene Änderung der Proben temperatur mit Hilfe eines Mikro-Heiz-Kühltesches. Die Auslenkung von Cr/ $\text{VMoO}_2$ -Nanoaktoren zeigt den Formgedächtniseffekt (SME) selbst bei der kleinsten untersuchten lateralen Breite von  $300\text{ nm}$ . Nanoaktoren

mit einer Balkenbreite von 600 nm erreichen einen großen relativen Faktor bezogen auf die Balkenlänge von 15 %, der bei einer Balkenbreite von 300 nm auf 8 % abnimmt.

Das Funktionsprinzip der VO<sub>2</sub>-basierten photonischen Bauelemente besteht darin, die Lichtausbreitung in Si-Wellenleitern auf der Grundlage des Isolator-Metall-Übergangs in VO<sub>2</sub>-Schichten zu modulieren. Temperaturabhängige optische Transmissionsmessungen zeigen, dass die Transmission beim Übergang vom heißen (Metall-) zum kalten (Isolator-)Zustand verringert, wodurch optisches Ein/Ausschalten ermöglicht wird.

# Publications

## Journal Publications

- S. Rastjoo, X. Wang, A. Ludwig, M. Kohl, Top-down fabrication and transformation properties of vanadium dioxide nanostructures, *J. Appl. Phys.* 125 (2019) 225104.
- S. Rastjoo, R. Fechner, L. Bumke, M. Kötz, E. Quandt, M. Kohl, Development and co-integration of a SMA / Si bimorph nanoactuator for Si photonic circuits, *Microelectron. Eng.* 225 (2020) 111257.

## Conference Contributions

- S. Rastjoo, X. Wang, A. Ludwig, M. Kohl, Fabrication of vanadium dioxide-based film nanostructures for nanoactuation, 43<sup>rd</sup> Int. Conf. Micro Nano Eng., Braga (2017). (Invited poster pitch, poster presentations)
- S. Rastjoo, X. Wang, A. Ludwig, M. Kohl Fabrication and transformation properties of vanadium dioxide nanoactuators, Int. Conf. Shape Mem. Superelastic Technol. SMST, Konstanz (2019). (Oral presentation)
- S. Rastjoo, X. Wang, A. Ludwig, M. Kohl, Transformation and actuation properties of vanadium dioxide-based nanostructures, 4<sup>th</sup> Euro Intell. Mater. 2019, Kiel (2019). (Oral presentation)
- S. Rastjoo, R. Fechner, M. Kötz, M. Kohl, Optical waveguide switching based on a co-integrated SMA bimorph actuator, 45<sup>th</sup> Int. Conf. Micro Nano Eng., Rhodes (2019). (Oral presentation)
- S. Rastjoo, R. Fechner, L. Bumke, E. Quandt, M. Kohl, Development of co-integrated shape memory actuators for silicon micro- and nanomechanics, 17th Int. Conf. New Actuator Syst. Appl., Mannheim (2020). (Accepted for oral presentation)

## Acknowledged in

- M. Kohl, M. Gueltig, F. Wendler, Coupled simulation of thermomagnetic energy generation based on NiMnGa heusler alloy films, *Shape Mem. Superelasticity.* 4 (2018) 242–255.
- F. Lambrecht, N. Sagardiluz, M. Gueltig, I.R. Aseguinolaza, V.A. Chernenko, M. Kohl, Martensitic transformation in NiMnGa/Si bimorph nanoactuators with ultra-low hysteresis, *Appl. Phys. Lett.* 110 (2017) 213104.



# Contents

<b>Acknowledgments</b> .....	<b>i</b>
<b>Abstract</b> .....	<b>iii</b>
<b>Kurzfassung</b> .....	<b>v</b>
<b>Publications</b> .....	<b>vii</b>
<b>Contents</b> .....	<b>ix</b>
<b>List of Abbreviations</b> .....	<b>xi</b>
<b>1 Introduction</b> .....	<b>1</b>
<b>2 Smart Materials</b> .....	<b>5</b>
2.1 Shape Memory Materials.....	5
2.1.1 Martensitic Transformation in Shape Memory Materials.....	6
2.2 Vanadium Dioxide.....	9
2.2.1 Crystal Structure and Mechanical Properties .....	9
2.2.2 Energy Band Diagram and Electrical Properties .....	11
2.2.3 Lattice Dynamics and Optical Properties.....	12
<b>3 Silicon Photonics</b> .....	<b>13</b>
3.1 Fundamentals of Light Propagation in Materials .....	13
3.1.1 Electromagnetic Waves in Silicon-Based Structures.....	14
3.2 Optical Loss Mechanisms.....	15
<b>4 Nanofabrication and Characterization Techniques</b> .....	<b>17</b>
4.1 Electron Beam Physical Vapor Deposition .....	17
4.2 Reactive Magnetron Sputtering .....	18
4.3 Electron Beam Lithography.....	19
4.4 Etching Techniques .....	21
4.4.1 Reactive Ion Etching .....	21
4.4.2 Wet Etching.....	22
4.5 Ellipsometry .....	23
4.6 Four-Terminal Electrical Measurement.....	24
<b>5 Fabrication of Vanadium Dioxide-Based Nanostructures</b> .....	<b>27</b>
5.1 Vanadium Dioxide-Based Thin Films.....	27
5.2 Nanomachining of Substrate Prior to Film Deposition .....	29
5.3 Direct Nanomachining of Vanadium Dioxide-Based Films.....	32
5.3.1 Fabrication of Bimorph Nanoactuators .....	34
5.4 VO <sub>2</sub> Nanopillars .....	35

5.5 Summary .....	36
<b>6 Electrical and Mechanical Performance of Vanadium Dioxide-Based Nanostructures .....</b>	<b>37</b>
6.1 Electrical Properties .....	37
6.1.1 Temperature-Dependent Electrical Resistance Characteristics of VO <sub>2</sub> -Based Films .....	37
6.1.2 Temperature-Dependent Electrical Resistance of VMOO <sub>2</sub> Nanobridges ..	41
6.2 In-Situ Nanoactuation .....	49
6.2.1 Nanoactuation by Homogeneous Temperature Control .....	49
6.2.2 Nanoactuation by Joule Heating .....	55
6.3 Summary .....	57
<b>7 Development of Optical Devices Based on Vanadium Dioxide .....</b>	<b>59</b>
7.1 Optical Properties of VO <sub>2</sub> Films Determined by Ellipsometry .....	59
7.2 Concept of Device Design .....	60
7.3 Proof-of-Concept by FEM Simulation .....	62
7.4 Fabrication .....	68
7.5 Optical Transmission Measurements .....	70
7.5.1 Optical Measurement Setup.....	70
7.5.2 Measurement Routine.....	71
7.6 Summary .....	73
<b>8 Summary and Conclusion.....</b>	<b>75</b>
<b>9 Outlook.....</b>	<b>79</b>
<b>Appendix A .....</b>	<b>83</b>
Ellipsometry Models of VO <sub>x</sub> -Based Films .....	83
<b>Appendix B.....</b>	<b>85</b>
Optimization of Thickness Ratio in Bilayer Cantilevers.....	85
<b>Appendix C .....</b>	<b>87</b>
Challenges of Nanofabrication Based on EBL and RIE.....	87
<b>References .....</b>	<b>89</b>

# List of Abbreviations

3D	Three dimensional
CCP	Capacitive coupled plasma
CHF <sub>3</sub>	Trifluoromethane
CPD	Critical point drying
EBL	Electron beam lithography
EBPVD	Electron beam physical vapor deposition
ER	Extinction ratio
FEM	Finite element method
FIB	Focused ion beam
FWHM	Full width at half maximum
HBr	Hydrogen Bromide
HF	Hydrofluoric
HSQ	Hydrogen silsesquioxane
IL	Insertion loss
IR	Infrared
MHCS	Micro heating-cooling stage
MEMS	Micro electro-mechanical system
NEMS	Nano electro-mechanical system
NIR	Near Infrared
Ni-Ti	Nickel-titanium
OSA	Optical spectrum analyzer
PIPED	Silicon-plasmonic internal-photoemission detector
PMMA	Poly(methyl methacrylate)

PTFE	Polytetrafluoroethylene
PVD	Physical vapor deposition
RBS	Rutherford backscattering spectroscopy
RF	Radiofrequency
RIE	Reactive ion etching
SEM	Scanning electron microscope
SF6	Sulfur hexafluoride
Si	Silicon
SMA	Shape memory alloy
SME	Shape memory effect
SMM	Shape memory material
SOI	Silicon on insulator
SPP	Surface plasmon polaritons
TE	Transverse electric
TM	Transverse magnetic
TMAH	Tetramethylammonium hydroxide
VO2	Vanadium dioxide
XRD	X-Ray diffraction

# 1 Introduction

The continuous demand for low-cost and large-scale production made development of miniaturized devices one of the main concerns in various fields such as in semiconductor technologies, photonics and biomedical applications in the past fifty years [1]. Aiming at miniaturized devices with multifunctional properties, new concepts need to be established, which enable integration of various components, passive as well as active on a single substrate. In order to increase the performance of devices in micro and nano scale, not only innovative fabrication techniques are required, but developing novel materials and investigating their properties is in focus of many ongoing studies as well.

For the first time in 1969, S.E. Miller [2] proposed the term *integrated optics* to highlight the similarity between planar optical circuits and the well-developed integrated micro-electronic circuits. Integration on a single chip, requires miniaturization of different photonic devices, where combining and interconnecting them is realized through optical waveguide structures [2]. Currently, different concepts are being developed to modify the propagation of light in a waveguide including either active or passive switching methods. These concepts comprise coupling of the light between fixed waveguides, changing the direction of the waveguide as well as the evanescent coupling or modifying the refractive index of the material [3,4].

Regarding active switching, the co-integration of micro and nano electro mechanical systems (MEMS and NEMS) and optical devices have led to various technological and scientific achievements in recent years [3]. State-of-the-art technologies include photonic crystal slab waveguides with integrated bimorph cantilevers [5], Mach-Zehnder interferometer configurations [6] and resonant structures such as electrostatically actuated ring resonators [3,7,8]. These devices require relatively large footprints, typically in the order of a few hundreds of microns [3]. Passive switching can be achieved by integration of a material with nonlinear properties into silicon (Si), e.g. graphene [9], organic materials [10] and alternatively the multifunctional vanadium dioxide VO<sub>2</sub>.

A group of materials, so-called *smart materials* show great potential for development of devices in small dimensions, due to their favorable scaling behavior and multifunctional property. *Shape memory materials* (SMM) are a class of *smart materials* exhibiting martensitic phase transformation. The transformation can be induced either by changing the temperature or by applying an external stress, through which, SMMs exhibit particular thermomechanical behavior and shape memory capabilities [11]. Accordingly, SMMs and shape memory alloys (SMMA) are widely used in variety of applications such as actuation, energy harvesting and elastocaloric cooling [12–15]. Providing high energy densities in the order of  $10^7$  J/m<sup>3</sup>, SMAs can greatly contribute to further downsizing of

actively controlled photonic components. However, fabrication complexities and experimental challenges as well as fundamental physical constraints could be obstacles towards realizing nano-scaled structured based on SMMs. Up to now, bimorph nanoactuators based on SMA are fabricated with lateral dimensions down to 50 nm [16,17]. First optical waveguide switches have been developed having a footprint of  $10 \mu\text{m}^2$ , where optical switching between outputs of two sustainable waveguides in close vicinity of each other is enabled by the out-of-plane deflection of a SMA/Si nanoactuator [18,19].

Besides conventional SMMs, e.g. Ni-Ti and Cu-based SMAs, shape memory effect (SME) is investigated in polymers and ceramics as well, among which,  $\text{VO}_2$  has attracted interest of numerous studies in recent years.

It was first in 1959 that Morin reported on the reversible insulator-metal transition in  $\text{VO}_2$  at the temperature of around  $67^\circ\text{C}$  [20]. The transition caused by a crystal structure transformation is accompanied with drastic changes in physical properties such as in optical transmittance or thermal conductivity. The phase transformation in  $\text{VO}_2$  can be induced by diverse external stimuli including optical, thermal or electric and magnetic fields [21].

Device performance is principally dependent on the size, doping, morphology and crystallinity of  $\text{VO}_2$  [22–24]. It has been previously shown for polycrystalline oxides that decreasing the size of structures in thickness and lateral width down to the scale of grains results in considerable enhancement of mechanical strength and reduced internal mismatch stress during martensitic transformation [25]. Accordingly, by decreasing characteristic dimensions of  $\text{VO}_2$  structures, grain-related defects are expected to be reduced, thus, mechanical as well as electrical performances could improve.

Furthermore, the insulator-metal transition in  $\text{VO}_2$  leads to drastic changes in the refractive index and the optical absorption coefficient particularly in the infrared (IR) wavelength region [26], which makes  $\text{VO}_2$  a material for optical devices and for applications in telecommunications [27–29]. Due to its multifunctional properties  $\text{VO}_2$  is a great candidate for both passive and active optical switching as well as for the development of novel smart devices [21,30,31].

Up to now, various bottom-up and top-down methods have been reported for the fabrication of  $\text{VO}_2$ -based structures. Nevertheless, achieving free-standing nanostructures to study size dependence is challenging. Based on previous top-down approaches,  $\text{VO}_2$  structures have been developed on the micrometer region. For instance,  $\text{VO}_2$  beams have been fabricated either by deposition of  $\text{VO}_2$  films on pre-structured substrates [32] or by subtractive methods using photolithography [33]. Another approach to realize nanostructures is based on bottom-up processes. Particularly, bottom-up methods are applied to create monocrystalline structures, where martensitic transformation properties can be investigated in  $\text{VO}_2$  crystals. These methods usually involve the random growth of individual nanowires on substrates [34–38] followed by the challenging process of transferring

grown nanowires to a target substrate. A possible method is described in [38], where positioning of nanowires on the target substrate is achieved by creating interconnections using an e-beam induced deposition (EBID) of Pt contacts. Alternatively, after deposition of VO<sub>2</sub>-based films on planar substrates, single crystalline nanowires can be created by the focused ion beam (FIB) milling, which is a complex and a time-consuming process [25,39]. Hence, it is essential to overcome limitations in the nanofabrication technology for investigations on multifunctional properties of VO<sub>2</sub> in the nanoscale.

### **Thesis Objectives**

Goal of this thesis is to explore, develop and demonstrate novel nanostructures and devices based on VO<sub>2</sub> thin films to study their electrical and thermo-mechanical properties including their size dependencies. For this purpose, nanofabrication methods need to be established, which enable not only patterning of films on planar substrates but realizing free-standing VO<sub>2</sub>-based nanomachines as well. New characterization techniques have to be developed to accomplish a profound understanding of multifunctional properties of VO<sub>2</sub> in the nano-scale regime. This knowledge is then applied to demonstrate proof-of-principle photonic devices. Here, the focus is on a VO<sub>2</sub>-based nanoswitches to control the propagation of light in a Si waveguide using the insulator-metal transition. This development is supported by finite element method (FEM) simulations of the optical switching performance.

### **Thesis Outline**

This thesis consists of 9 chapters.

Chapter 2 starts with an introduction to *smart materials* and martensitic transformation. Afterwards, the phenomenology of the insulator-metal transition in VO<sub>2</sub> is described regarding its crystal structure and energy band diagram.

Chapter 3 describes fundamentals of silicon photonics including the propagation principle of electromagnetic waves in solids, basic Si-based structures and the corresponding optical loss mechanisms.

In chapter 4, various techniques of nanofabrication and characterization of materials and devices are introduced including physical vapor deposition (PVD), electron beam lithography (EBL), ellipsometry and four-terminal electrical measurements.

Chapter 5 explains the deposition of VO<sub>2</sub>-based thin films by reactive magnetron sputtering and different top-down and bottom-up fabrication procedures developed to realize free-standing nanostructures based on VO<sub>2</sub> films.

Chapter 6 is dedicated to scaling and size effects in VO<sub>2</sub>-based micro and nanostructures. In particular, the temperature-dependent electrical resistance of VMO<sub>2</sub> free-standing nanobridges is studied with respect to a reference film. Furthermore, the actuation of Cr/VMO<sub>2</sub> nano double-beams is investigated in-situ inside a SEM through Joule heating and homogeneous temperature control.

Chapter 7 presents a VO<sub>2</sub>-based photonic demonstrator device using the metal-insulator transition in a VO<sub>2</sub> nanostructure to control the propagation of light in a Si waveguide on a silicon on insulator (SOI) platform. The device performance is investigated by FEM simulations and by optical transmission measurements.

Chapters 8 and 9 summarize and give an outlook on future challenges to investigate scaling/size effects, nanoactuation and photonics applications, respectively.

## 2 Smart Materials

*Smart materials* are special materials with intrinsic sensing and/or actuating capabilities which are controlled by external stimuli, such as temperature, electric field, stress, light etc. Different types of smart materials include e.g. piezoelectric materials, photovoltaic materials, ferroelectrics etc. [40].

*Multifunctional materials* are a group of *smart materials*, which can implement multiple tasks in a system. *Multifunctional materials* combine enhanced structural or mechanical performances such as high strengths and stiffness, with at least one additional functionality related to a material property, e.g. optical or electrical characteristics. Typically, *multifunctional materials* can be *autonomic*, i.e. they can sense and respond to external stimuli with smallest external intervening. Furthermore, they can be *adaptive*, i.e. they can readjust their functionality or structural performance depending on circumstances [41]. The multifunctionality of materials can be exploited from macro down to nano scales including microrobotics and NEMS [16,42]. These materials have great potentials in development of high-performances devices, while enabling down-sizing [21,41,43–46].

*Shape memory materials* (SMMs) belong to active multifunctional materials, which exhibit a mechanical response to various stimuli including external stress, thermal, electric and magnetic fields [47]. The following sections give an introduction to shape memory materials including *shape memory alloys* (SMA) and oxides like vanadium dioxide ( $\text{VO}_2$ ) regarding their crystallographic structure and phase transformation properties. Afterwards, the target material of this work, namely, vanadium dioxide, and its multifunctional properties are introduced and discussed in detail.

### 2.1 Shape Memory Materials

Shape memory materials are a class of smart materials exhibiting the exceptional property of remembering their original shape, which is described by the shape memory effect (SME) [46]. SME was first found in a SMA Au-47.5 at % Cd alloy in 1951 by Chang and Read [48], but still unutilized until 1963, when it was published with the discovery in NiTi by Buehler *et al.* [49]. Today, besides conventional SMAs, such as NiTiCu or CuZnAl [50,51], a whole series of shape memory material systems are known exhibiting the SME. This includes polymers, e.g. PTFE (polytetrafluoroethylene) and ceramics, e.g.  $\text{ZrO}_2$  or  $\text{VO}_2$ , in which shape memory properties are observed [11,43,47]. The phenomenology of the SME is described in the following section.

### 2.1.1 Martensitic Transformation in Shape Memory Materials

Shape memory materials commonly exhibit two stable phases having different crystal structures: a high and a low temperature phase, austenite and martensite phases, respectively. The austenite phase is usually cubic, whereas the martensite phase has a lower symmetry of crystal lattice. Generally, there are multiple *variants* of martensites having different crystal orientations. The transformation between austenite and martensite phases is called a *martensitic transformation*, which is a diffusionless first order transition that is enabled by shear lattice distortions [11,46]. Upon cooling from austenite, formation of self-accommodated martensitic variants leads to a *twinned* assembly. In this case, variants with specific crystallographic orientations are equally distributed over the sample and, thus, the averaged macroscopic shape change is negligible. If a mechanical load is applied, the most unfavorably oriented portions will realign to twinned martensites. This leads to the formation of *detwinned* martensite and results in a macroscopic shape change. Figure 2.1 depicts a schematic of crystal structures in the stress-temperature phase diagram of a SMA.

By increasing the temperature of the material in the detwinned martensite, it transforms to austenite and undergoes a complete shape recovery. This process defines the SME or more precisely the *one-way* SME. The martensitic transformation is associated with a hysteresis and involves four characteristic transformation temperatures. Upon cooling, austenite begins to transform to martensite at the martensitic start temperature  $T_{Ms}$  until it fully transforms to the martensite at the martensitic finish temperature  $T_{Mf}$ . By reverse transformation, martensite starts to transform to austenite at the austenitic start temperature  $T_{As}$ , and subsequently, the transformation is completed at the austenitic finish temperature  $T_{Af}$  [52], as depicted in Figure 2.1.

The martensitic transformation can also be induced by applying a sufficiently large mechanical load to a sample in austenite state, i.e. at temperatures above  $T_{Af}$ , which results in transformation to the detwinned martensite. If the material is mechanically relieved, a complete shape recovery occurs. This behavior is known as the *pseudoelastic effect*.

For a better understanding, the thermodynamic aspects of the phase transformation in shape memory materials are further described in the following.

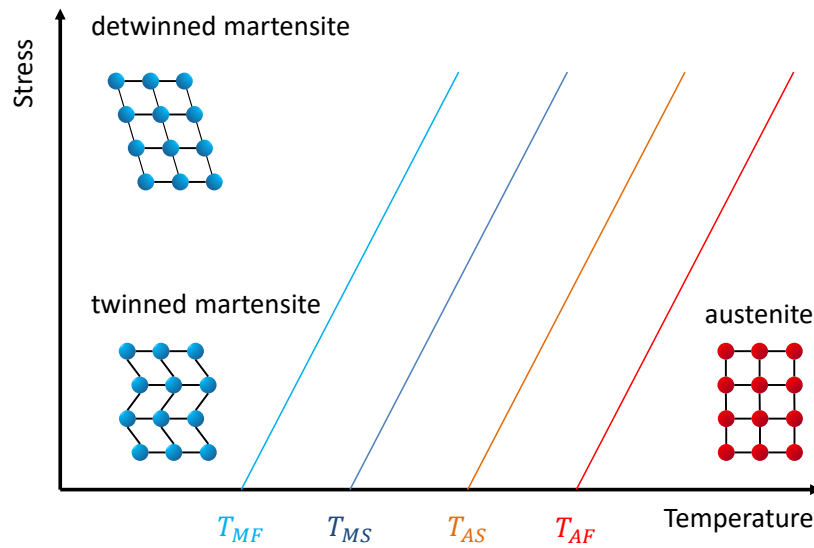


**Figure 2.1:** Schematic stress-temperature phase diagram of a SMA. The shape change associated with the phase transformation for a single crystal with six unit-cells is illustrated.  $T_{MF}$  and  $T_{MS}$  are the martensitic finish and start temperatures, respectively.  $T_{AS}$  and  $T_{Af}$  indicate the austenite start and finish temperatures, respectively. Adapted from [53].

### Thermodynamics of Phase Transformation

The martensitic transformation can be explained in terms of thermomechanical potentials of austenite and martensite states. The Seelecke-Müller-Achenbach model describes the evolution of martensitic fractions based on thermally activated processes [54]. For simplification, a one-dimensional system is assumed with one austenite (A) and two martensite states ( $M^-$  and  $M^+$ ) and only one transformation temperature ( $T_{tr}$ ). The Gibbs free energy of the system is given by

$$G = U - ST - P\Delta \quad (2.1)$$

where,  $U$  and  $S$  indicate the internal energy and entropy, respectively.  $T$  is the temperature,  $P$  the applied external load and  $\Delta$  the shear length. Figures 2.2a, b1 and c1 illustrate the effective potential energy of the system at zero external load  $P = 0$ . At the transformation temperature  $T_{tr}$ , austenite and martensite are in the thermodynamic equilibrium, thus, the Gibbs free energy indicates local minima for A,  $M^-$  and  $M^+$  states. For temperatures higher than  $T_{tr}$ , the austenite local minimum is lower than the martensite minima, thus, the austenite A is the stable state. Accordingly, at temperatures below  $T_{tr}$ , the martensite minima decrease, hence, martensite phase is energetically the more favorable state.

Under application of an external load  $\pm P$ , the minimum of the potential well of one of the martensite variants decreases.

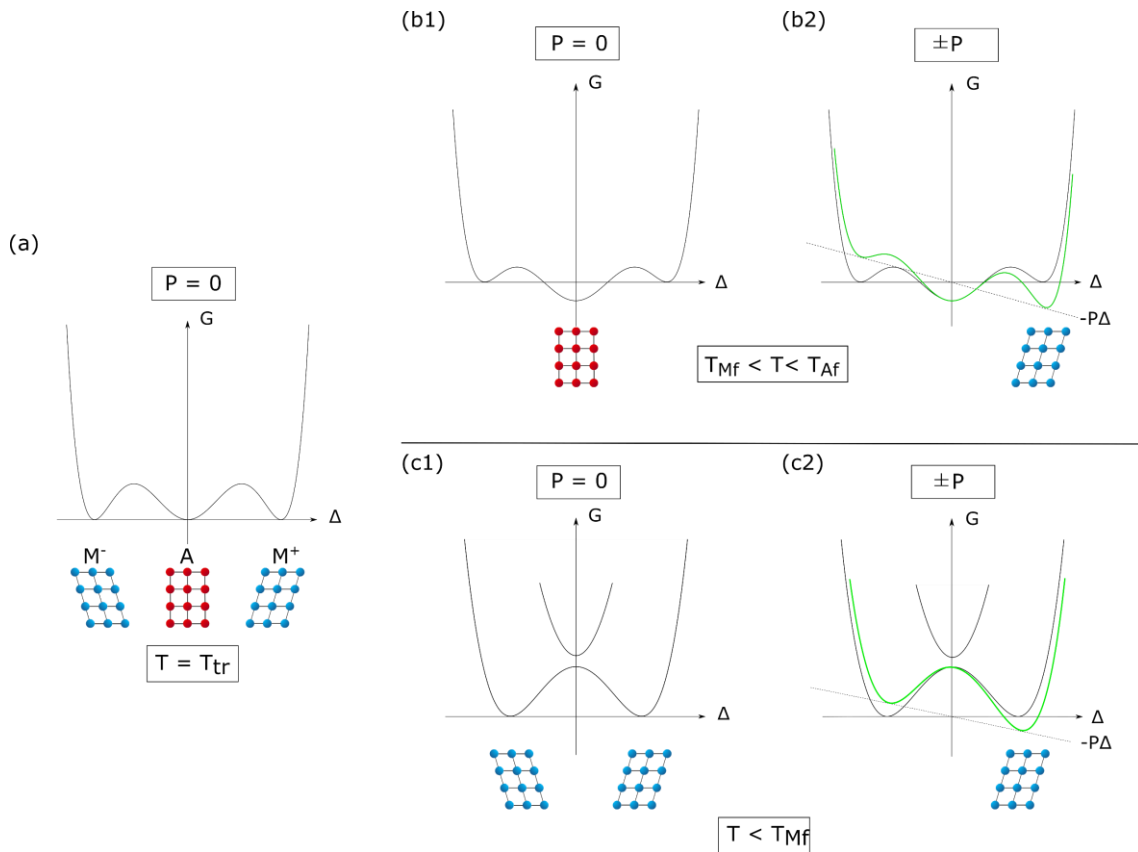


**Figure 2.2:** Effective potential energy landscape of a shape memory material and illustration of unit-cells. Abbreviations A,  $M^-$  and  $M^+$  stand for austenite and two martensite variants, respectively.  $T_{tr}$  is the transition temperature at zero external load  $P = 0$ . (a) At  $T = T_{tr}$  and  $P = 0$ , all three crystal structures of A,  $M^-$  and  $M^+$  coexist. (b1) At  $T_{Mf} < T < T_{Af}$  and  $P = 0$ , A and M phase coexist. (b2) By applying an external load  $\pm P$ , the minimum of the potential well of one of martensites variants decrease to lower than the minimum of A. (c1) At  $T < T_{Mf}$  and  $P = 0$ , both  $M^-$  and  $M^+$  can coexist and, (c2) at  $T < T_{Mf}$  and  $\pm P$ , either  $M^-$  or  $M^+$  will be the only stable state [11,55,56].

For temperatures below  $T_{Mf}$ , this leads to the formation of a specific martensite variant, either  $M^-$  and  $M^+$  (Figure 2.2 c2) and for temperatures higher than  $T_{Af}$ , the external load induces a phase transformation to one of the martensite phases (Figure 2.2 b2). Though, by further increase of temperature, austenite will be the only stable state [11,55,56].

### Clausius-Clapeyron Relation

The theoretical derivation of the stress-induced phase transformation is determined from the Clausius-Clapeyron relation [57,58]. The Clausius-Clapeyron relation is a macroscopic model, which describes the correlation between the pressure and temperature for conditions of equilibrium between two phases in a pressure-temperature phase diagram. The Clausius-Clapeyron relation is derived from the Gibbs free energy at the equilibrium

state [58]. For simplification, the one-dimensional model is considered with equal stiffness and thermal expansion coefficient for austenite and martensite phases. Consequently, a linear dependence on temperature is obtained by [47,58]:

$$\frac{dP}{dT} = -\frac{\Delta H\rho}{\varepsilon^{\text{tr}}T_{\text{tr}}} = c \quad (2.2)$$

where  $dP$  and  $dT$  are variations in stress and temperature, respectively.  $\Delta H$  indicates the enthalpy of transformation,  $\rho$  the density of the material and  $\varepsilon^{\text{tr}}$  the transformation strain.

## 2.2 Vanadium Dioxide

Vanadium dioxide  $\text{VO}_2$  is a *multifunctional material*, which goes through a reversible structural phase transformation at a temperature of around  $67^\circ\text{C}$ . This transformation can be prompted by diverse stimuli including electrical, optical, mechanical, electromechanical or magnetic perturbations. Owing its multistimuli responsive transformation,  $\text{VO}_2$  is known as an interesting *smart material* and has been extensively studied in recent years [21,30,59].

The structural phase transformation in  $\text{VO}_2$  is also accompanied with an insulator-metal transition, through which material properties change drastically, including its mechanical, electrical and optical characteristics. The following sections describe the phenomenology of the transformation in  $\text{VO}_2$  regarding its crystal structure and the energy band diagram.

### 2.2.1 Crystal Structure and Mechanical Properties

Above transformation temperature  $T > T_{\text{tr}}$ ,  $\text{VO}_2$  adopts a tetragonal rutile structure R, which belongs to the space group of  $P4_2/m$  with unit cell parameters  $a = b \approx 4.55 \text{ \AA}$  and  $c \approx 2.85 \text{ \AA}$  [60,61] (Figure 2.3c).

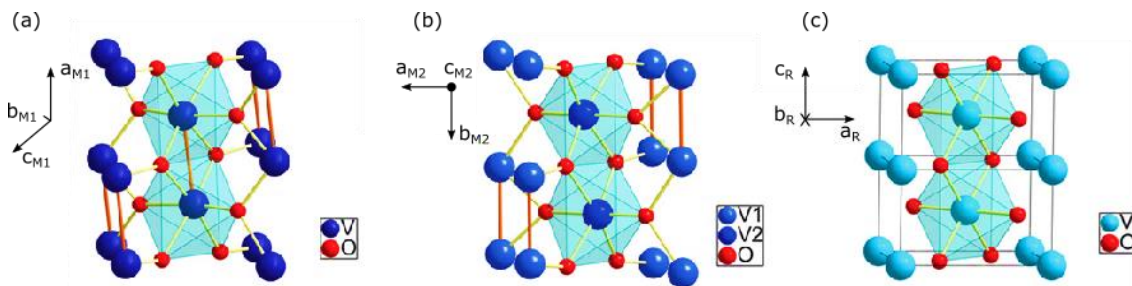


**Figure 2.3:** Schematic depiction of  $\text{VO}_2$  crystal structures for the (a) monoclinic M1 phase at  $T < T_{\text{tr}}$ , (b) the monoclinic M2 phase at  $T < T_{\text{tr}}$  and (c) the tetragonal R phase at  $T > T_{\text{tr}}$ . Adapted from [62].

At temperatures below  $T_{tr}$  and at ambient pressure, pure  $\text{VO}_2$  has monoclinic structure M1 with space group of  $P2_1/c$  and lattice constants  $a \approx 5.74 \text{ \AA}$ ,  $b \approx 4.52 \text{ \AA}$ ,  $c \approx 5.37 \text{ \AA}$  [60,63]. The M1 unit cell is characterized by pairing of V atoms along the  $a_{M1}$  axis, which corresponds to the  $c$  direction of the parent R phase. As shown in Figure 2.3a, it forms a zig-zag chain of V atoms with the dimer rotation along  $a_{M1}$  [64,65]. Besides the M1, an additional monoclinic structure is identified for pure  $\text{VO}_2$ . The so-called M2 phase is stabilized under an applied stress [60,61,66–68] or by substitutional doping of the pure  $\text{VO}_2$  with a third material such as Al, W or Cr [69–71]. M2 phase belongs to the space group  $C2/m$  with  $a = 9.0664 \text{ \AA}$ ,  $b = 5.7970 \text{ \AA}$ ,  $c = 4.5255 \text{ \AA}$  [64,65]. In M2 unit cell, two types of V atoms coexist. As depicted in Figure 2.3b, V2 types are tilted but not paired and V1 types are dimerized, nevertheless not tilted around the  $b_{M2}$  axis [62]. In addition to M1 and M2 phases, another semiconducting phase may occur under certain circumstances. It has been shown that at low temperatures in association with the stress along the  $c_R$  axis, a triclinic T phase may occur. The T phase shows up as an intermediate structure between M1 and M2 phases [66,72].

It has been demonstrated that depending on the range of temperature and stress, various transformation paths can be triggered for  $\text{VO}_2$ -based materials including M1-R, M1-M2-R and M1-T-M2-R transitions [68,72–74]. The  $R \rightarrow M1$  transformation leads to a spontaneous strain of  $\sim 1\%$  along the  $c_R$  axis and contractions of  $\sim 0.6\%$  and  $\sim 0.1\%$  in the  $a_R$  and  $b_R$  directions, respectively [64,75]. For the  $R \rightarrow M2$ , the transformation strain is up to  $\sim 2\%$  along  $c_R$  [76].

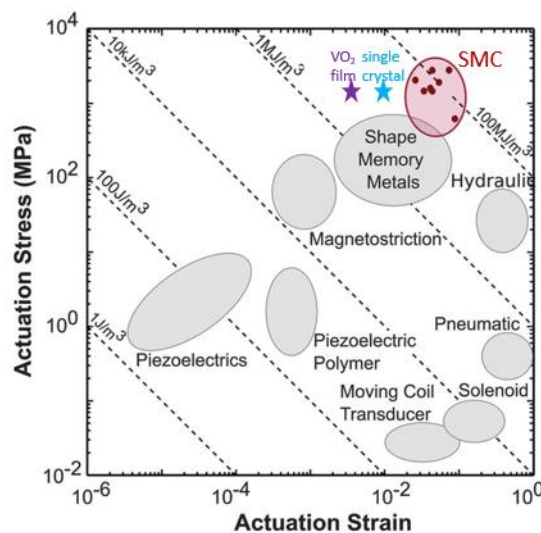


**Figure 2.4:** Comparison of actuation stress and strain diagram for various materials and systems. Dashed lines indicate contours of equal work output densities. Shape memory ceramics (SMC) offer work output values approaching  $100 \text{ MJ/m}^3$ . Stars indicate work outputs of  $\text{VO}_2$  films and single crystals exceeding  $10 \text{ MJ/m}^3$ . Adapted from [45].

Overall, large transformation strains and the high Young's modulus of  $\sim 140$  GPa for both M1 and R phases enable motions with large forces and high work densities [45,77], as it is depicted and compared to other materials and systems in the actuation stress and strain diagram in Figure 2.4.

### 2.2.2 Energy Band Diagram and Electrical Properties

Upon metal-insulating transition in VO<sub>2</sub>, its electrical resistivity declines up to five orders of magnitude [78,79]. There are two main approaches to describe the nature of the insulator-metal transition in VO<sub>2</sub>. The first mechanism was originally proposed by Goodenough and describes a *Peierls-type transition* based on the electronic band theory of *independent electrons*. In contrast, Zylberszejn and Mott attributed the insulator-metal transition to the *Mott-Hubbard* model, driven by strong *electron-electron correlations* [80].

In the primary work of Goodenough, the electronic and band structure of the VO<sub>2</sub> is described by the electronic band theory of independent electrons [81]. Figure 2.5 illustrates a schematic of the energy band diagram of VO<sub>2</sub> in the metal (a) and the insulator (b) state. In this model, two energy bands of  $\pi^*$  and  $d_{\parallel}$  are found around the Fermi energy  $E_F$ .

Upon metal-insulator transition, the crystal lattice distortion leads to an increase in energy of the  $\pi^*$  band above the Fermi level  $E_F$  accompanied by a split of the  $d_{\parallel}$  band. Splitting of the  $d_{\parallel}$  is driven by the dimerization of V chains along the  $c_R$  axis. The reorganization of these bands forms an energy bandgap in the insulating phase M1, as it is depicted in Figure 2.5b.

Up to now, several experimental studies have investigated the electronic structure of VO<sub>2</sub> using optical reflectivity, electrical transport measurements, X-ray photoemission and absorption spectroscopy [31,82–86]. Results from these studies are generally in agreement with Goodenough's model. Later, studies based on new technologies and computer simulations have offered important corrections to this model. Particularly, corrections are suggested to the magnitude of the bandgap in the monoclinic phase based on investigations on M1, M2 and T phases [75,83,86,87]. Moreover, photoemission and UV reflectance experiments revealed that besides structural distortions, a further opening of the bandgap is caused by electron-electron interactions indicating a correlated electronic nature of the transition rooted in the *Mott-Hubbard theory* [80,87,88]. In the work of Yao *et al.* [85], simultaneous tracking of the electrical resistivity and twisting angle of V dimers probed by X-ray absorption fine structure (XAFS) in fine temperature steps revealed a strong dependence of the electrical resistivity on the lattice distortion and found an intermediate monoclinic-like structure but with the metal character. Therefore, they concluded that the phase transformation may be described as a cooperative Peierls and Mott transition, named as *Mott-assisted Peierls* or *Peierls-Mott* models.

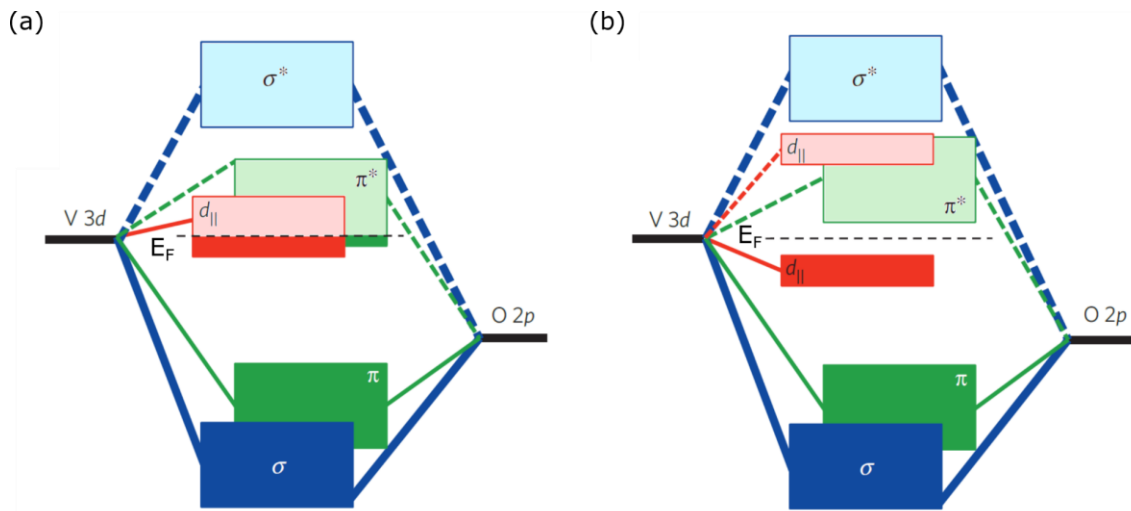


**Figure 2.5:** Schematic depiction of the VO<sub>2</sub> band diagram based on the Goodenough's model for (a) the rutile R crystal structure corresponding to the metal state and (b) the monoclinic M1 structure of the insulator state. The Fermi level is indicated by  $E_F$ . Adapted from [82].

### 2.2.3 Lattice Dynamics and Optical Properties

Optical properties of solids can be explained based on the energy-band structure of the material and the electron-phonon interactions. Different experimental techniques and simulation methods are applied to understand the exact evolution of phonons across the insulator-metal transition in VO<sub>2</sub> [37,89–93]. Studies by means of Raman and IR optical spectrometries revealed a strong broadening in the phonon spectrum of the rutile phase compared to the M1 phase, which is attributed to the strong electron-phonon coupling [31,91,92]. In a simplified model, optical and electronic properties of the VO<sub>2</sub> can be understood from the overall energy band diagram of the metal and insulator phases, as it is shown in Figure 2.5. Through the transition of VO<sub>2</sub> from the monoclinic to the rutile phase, the energy bandgap disappears leading to an insulator-to-metal transition. This results in a significant alteration of optical constants such as the refractive index  $n$  and the extinction coefficient  $\kappa$ , thus, leading to a drastic change in optical transmittance [27,94–97]. In fact, the absorption of light in the metal phase is much stronger compared to the absorption in the insulating phase for a wide range of wavelengths spectrum including the visible range 1.6 - 3.2 eV. In the spectral range below 0.7 eV, i.e. in infrared IR and near infrared NIR range, the insulating phase of the VO<sub>2</sub> is nearly transparent, whereas the metal state is opaque [26,94,98].

# 3 Silicon Photonics

Integrated photonic devices combine basic optical components for light generation, coupling, polarization, modulation etc. on a single chip. A key element in integrated photonics are the optical waveguides, which enable transmission of light in specific directions and interconnection of various photonic components.

Silicon (Si) is a semiconductor that offers a low energy absorption at typical wavelengths used in telecommunications, i.e. 1300 nm and 1550 nm, providing the main requirement for the efficient transmittance of light through photonic devices [99]. Besides appropriate optical properties of Si, its compatibility for low-cost and large-scale fabrications makes it a promising material for manufacturing of micro- and nano photonic components [99].

In this chapter, basic physical principles of optics and photonics are described. In section 3.1.1, key components for coupling and guidance of electromagnetic waves are introduced including Si-based grating couplers and waveguides integrated in a silicon on insulator (SOI) chip. Furthermore, possible optical loss mechanisms, which reduce the efficiency of light transport within a medium, are discussed briefly.

## 3.1 Fundamentals of Light Propagation in Materials

The principle of optic and photonic technologies is based on the interaction of light with matter. The propagation of an electromagnetic wave in a linear, homogeneous and isotropic material is described by Maxwell's equations

$$\begin{aligned}\nabla \cdot \mathbf{D} &= \rho \\ \nabla \cdot \mathbf{B} &= 0 \\ \nabla \times \mathbf{E} &= -\frac{\partial \mathbf{B}}{\partial t} \\ \nabla \times \mathbf{H} &= \mathbf{j} + \frac{\partial \mathbf{D}}{\partial t}\end{aligned}\tag{3.1}$$

where  $\mathbf{E}$  and  $\mathbf{B}$  are electric and magnetic fields, respectively. The displacement field is determined as  $\mathbf{D} = \epsilon \mathbf{E}$  and the magnetizing field as  $\mathbf{H} = \frac{1}{\mu} \mathbf{B}$ , where,  $\epsilon$  and  $\mu$  are material constants for dielectric permittivity and magnetic permeability, respectively.

The transport energy is the flux of the energy carried by the electromagnetic wave and is defined by [100]

$$\mathbf{P} = \mathbf{E} \times \mathbf{H}\tag{3.2}$$

The propagation speed of the electromagnetic wave is determined by  $v = 1/\sqrt{\varepsilon\mu}$ . For propagation in free space, i.e. the speed of light, it is given by  $c = 1/\sqrt{\varepsilon_0\mu_0}$ , where,  $\varepsilon_0$  and  $\mu_0$  are parameters for the dielectric permittivity and the magnetic permeability of the free space, respectively. The propagation speed can be also expressed as a function of speed of light by [100]

$$v = \frac{c}{n} \quad (3.3)$$

where  $n$  represents the refractive index, which is determined by

$$n = \frac{\sqrt{\varepsilon\mu}}{\sqrt{\varepsilon_0\mu_0}}. \quad (3.4)$$

For a non-magnetic, i.e.  $\mu = \mu_0$ , and absorbing material, the dielectric permittivity and therefore, the refractive index are complex quantities. The complex refractive index  $\tilde{n}$  is defined by

$$\tilde{n} = n + i\kappa \quad (3.5)$$

here,  $n$  defines the real refractive index and  $\kappa$  is the extinction coefficient [100].

### 3.1.1 Electromagnetic Waves in Silicon-Based Structures

The transmission of light through a medium depends basically on two main parameters: material properties, such as the complex refractive index and geometry parameters, which enable the confinement of light within a structure. The low photon absorption in Si [99] makes it a promising material for the efficient guidance of the light in photonic components. In the simplest description, light can be confined within structures having higher refractive indices compared to those of surrounding media, due to the total internal reflection at the interphases. Figure 3.1a depicts a schematic of light propagation through a planar Si waveguide embedded on a SiO<sub>2</sub> substrate and a cladding with lower reflective index than Si. The totally confined light in a planar waveguide can be guided, if the condition for constructive interference is fulfilled. This implies that the total phase shift due to the reflection at interfaces should be a multiple of  $2\pi$ , thus, the guidance of the light inside a waveguide is limited to a certain set of propagation angles. This condition leads to specific guided modes having a certain electromagnetic field distribution and propagation velocity. Generally, two types of modes are guided through a rectangular waveguide, i.e. *transverse electric (TE) modes*, with the electrical field parallel to the propagation direction, and *transverse magnetic (TM) modes* with the magnetic field parallel to the propagation direction.

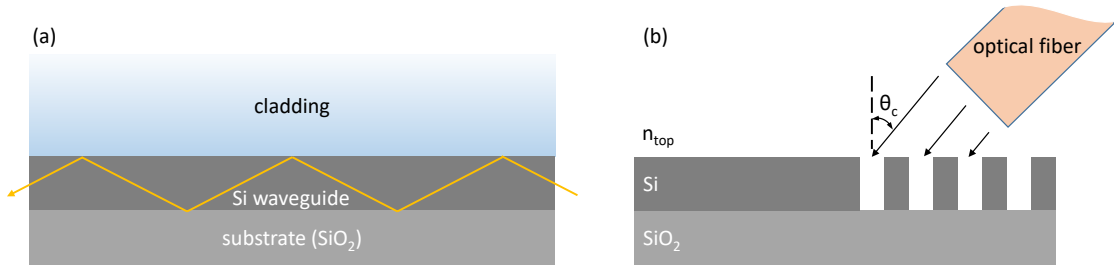


**Figure 3.1:** (a) Schematic illustration of light propagation inside a Si waveguide by total reflection, and (b) Si grating coupler for light coupling from an out-of-plane source by an optical fiber (not to scale).

Achieving monomode channel waveguides is of great importance in integrated photonics and telecommunication applications [101]. Single mode waveguides are realized by reducing the cross-sectional dimensions of waveguides, where only one mode can be guided.

In order to couple light efficiently from an out-of-plane source, e.g. from a laser into a waveguide, a vertical grating coupler is integrated to the input of the waveguide. An additional grating coupler is required at the other end of the waveguide to collect the output signal. The basic operation of a grating couple is determined through the Bragg condition [102]:

$$n_{\text{eff}} = n_{\text{top}} \sin \theta_c + k \frac{\lambda}{\Lambda} \quad (3.6)$$

where  $n_{\text{eff}}$  and  $n_{\text{top}}$  are the effective refractive index of the grating and the refractive index of cladding material on top, respectively.  $\theta_c$  is the coupling angle measured perpendicular to the plane of the grating and the wave vector  $k$  defines the particular diffraction mode.  $\lambda$  is the wavelength of the incident light and the grating period is given by  $\Lambda$ . Figure 3.1b shows a Si grating coupler on a SiO<sub>2</sub> substrate. In addition to mentioned parameters, the depth of the gratings and the fill factor influence the coupling characteristic. The fill factor is the part of the grating period that is occupied by the Si structure. By adjusting the parameters of the grating coupler, its efficiency can be optimized for either TE or TM modes at a given input wavelength [103].

## 3.2 Optical Loss Mechanisms

The propagating light through a waveguide is attenuated through different loss mechanisms, which is mainly ascribed to absorption, scattering and radiation losses [104,105].

#### **Absorption loss**

Light absorption is a major cause of loss in optical components. Through interaction of the electromagnetic wave with the material, the light power is absorbed and transferred into other forms of energy like the thermal energy [104]. The absorption loss depends on the wavelength of the light and the complex refractive index of the medium, as it is discussed above.

#### **Scattering Loss**

The scattering loss is attributed to the fabrication process and usually predominates in Si waveguides [106,107]. The volumetric scattering occurs due to the refractive index inhomogeneity at impurity islands and crystal defects, whereas the surface scattering happens at structure boundaries and interfaces [108]. The surface scattering has a major impact on reducing the efficiency of the optical transmittance in Si waveguides due to the roughness at sidewalls of the waveguide after fabrications through lithographic processes [105,106].

#### **Radiation loss**

The propagating light is not perfectly confined inside the waveguide. In fact, a small fraction of the light wave is guided outside through the evanescent field leading to the power loss by radiation [109]. The energy loss can be described by the tunneling of photons through a potential barrier at boundaries of structures. The larger the refractive index contrast between the waveguide medium and its surrounding, the higher the potential barrier for photons to tunnel, thus, the radiation loss declines. Radiation losses become significant for structures having curved boundaries e.g. for s-shaped waveguides [104].

In addition to the general optical loss mechanisms mentioned above, there is another mechanism termed as the coupling loss. The coupling of the light from an out-of-plane source into an on-chip waveguide is associated by optical losses as a result of the mode-mismatch and the misalignment of the fiber to the on-chip grating [110]

## 4 Nanofabrication and Characterization Techniques

In the following chapter, fabrication technologies to realize the micro and nano devices are introduced. Two common ways for deposition of thin films based on physical vapor deposition (PVD) are explained, namely, electron beam physical vapor deposition EBPVD (section 4.1) and dc-pulsed reactive magnetron sputtering (section 4.2). Methods for nanomachining of substrates based on electron beam lithography (EBL) and different material etching approaches are described in sections 4.3 and 4.4, respectively. Various characterization techniques are used to investigate material properties. Ellipsometry measurements are used to obtain the thickness and optical properties of films, which will be discussed in section 4.5. Furthermore, the four-terminal method to determine the surface electrical resistivity is presented in section 4.6.

### 4.1 Electron Beam Physical Vapor Deposition

A common method to deposit thin films on surfaces is through physical vapor deposition (PVD). The evaporation of solid precursors is realized by diverse physical approaches such as inductive heating, laser or electron beam (e-beam) induced heating. PVD by e-beam, known as EBPVD, provides high deposition rates on large areas [111]. The operation principle is schematically illustrated in Figure 4.1. The electron beam is generated by an electron gun, commonly by field emission of tungsten filaments, is accelerated to a high kinetic energy and then focused on the material/target ingot. The kinetic energy of electrons transforms into thermal energy leading to the material evaporation.

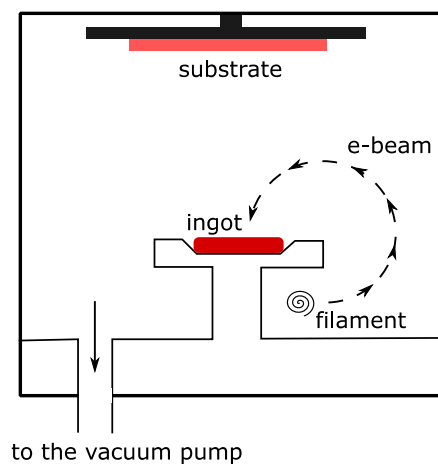


**Figure 4.1:** Sketch of a typical electron beam physical vapor deposition (EBPVD) system.

The generated vapors coat all surfaces in the vacuum chamber, which leads to a homogeneous deposition on the sample/substrate that is placed on the other side of the chamber on top of the ingot.

## 4.2 Reactive Magnetron Sputtering

Magnetron sputtering is a way of PVD to coat layers with thicknesses from a few nanometers up to several micrometers. This method is applicable for the deposition of oxide, nitride and carbide films with at least one metal or metalloid compound and a non-metal component. The metal element is placed on a precursor, so-called target, and the non-metal component is introduced to the chamber through the corresponding reactive gas e.g.  $O_2$  [112]. The operation principle of the reactive magnetron sputter is depicted in Figure 4.2. The metal target is sputtered by energetic positive ions, which consequently generates the metal vapor.

The most commonly used inert gas for this purpose is argon (Ar), which is extracted from a magnetically enhanced glow discharge at a low pressure in the vacuum chamber. In addition, an electrical potential difference is applied between the target (cathode) and the chamber (anode). Due to the magnetic field above the target, a strong electric field develops along the perpendicular direction to the magnetic field. Accordingly, positively charged ions are accelerated towards the target and eject metal atoms, which travel through the chamber and deposit on the substrate surface. The desired compound is formed by the chemical reaction of the sputtered metal with the reactive gas mainly on exposed surfaces [113,114].

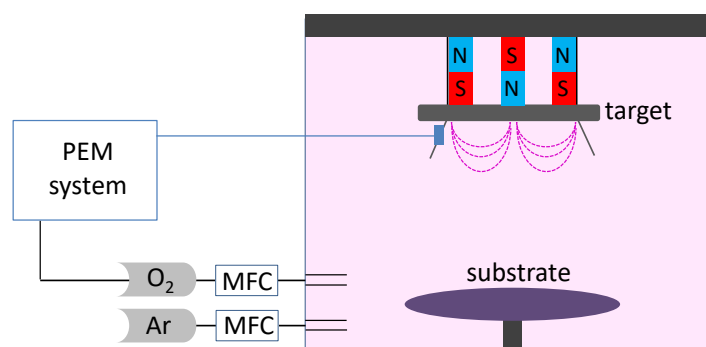


**Figure 4.2:** Schematic illustration of the reactive magnetron sputtering chamber including a plasma emission monitor (PEM) system and mass flow controllers (MFC). The PEM system is coupled to the  $O_2$ -MFC and allows for the dynamic control of the  $O_2$  flow into the chamber. A magnetically confined plasma is created above the target surface and creates positively charged ions, which strike the target. Sputtered atoms from the target spread through the vacuum chamber, collide with reactive gas atoms and deposit on the substrate.

### 4.3 Electron Beam Lithography

Electron Beam Lithography (EBL) is a mask-less technique for fabrication of micro and nano structures. In this method, the focused beam of electrons is used to write single or multi-level patterns onto surfaces.

The EBL process includes three main steps, which are the coating of the sample with a layer of an e-beam resist, the exposure by the e-beam and the development of the resist.

The ability of patterning nanometer-scale features stems from the short wavelength  $\lambda$  of accelerated electrons that is defined by the de-Broglie relation:

$$\lambda = \frac{h}{m \cdot v} \quad (4.1)$$

where  $h$  is the Planck's constant,  $m$  and  $v$  are mass and velocity of the electron, respectively.

Structures presented in this work are patterned using a Raith EBPG5200Z e-beam writer, which operates with an acceleration voltage of 100 kV. The approximated velocity of an electron is 0.55 times the speed of light  $c = 2.99 \cdot 10^8$ , thus, the de-Broglie wavelength of electrons is determined to be around  $0.037 \text{ \AA}$ .

The maximum achievable resolution is in practice limited by the quality of equipment components, such as the electron source and electromagnetic lenses and deflectors, which result in a larger spot of the focused beam. Other limitation factors include the chemical contrast of the resist and the corresponding developer. Furthermore, the interaction of the e-beam with electrons of atoms in the resist generates backscattered electrons. Consequently, the diameter of the focused e-beam  $d$  increases as a function of the resist thickness  $t_R$ , which is defined by

$$d = 0.9 \cdot \left( \frac{t_R}{E} \right)^{1.5} \quad (4.2)$$

where  $E$  is the acceleration energy of the e-beam in keV [115].

Nevertheless, a minimum feature size of around a few nanometers can be realized [115–117]. In addition to the high-resolution patterning, the mask-less process allows for the flexible change of layouts, which is beneficial for research purposes. The e-beam writer provides a graphical interface to create and to visualize layouts of patterns for exposure, through which an e-beam dose variation can be implemented as well. The disadvantage of the EBL is that the writing of patterns by the scanning electron beam is a slow process [118].

In this work, resists are applied by using a spin-coater. Through this method, the sample rotates at a high speed, thus, the fluidic resist is spread on the substrate by centrifugal forces. Depending on the resist and the substrate, the thickness of the resist layer can be adjusted by the rotation speed and it is determined by ellipsometry measurements, as described in section 4.5.

### **E-Beam Resists**

Resists are generally long chains of carbon-based polymers. There are two types of e-beam resists, namely, positive and negative tone resists.

In a negative resist, the e-beam exposure leads to the polymerization and the cross-linking of polymer chains, thus, the part of the resist that is exposed to the e-beam becomes insoluble to the resist developer. In contrast, for positive resists, the part of the resist which is exposed to the e-beam becomes soluble to the resist developer [118].

After spin-coating and exposure by the e-beam, the desired layout of patterns is transferred to the resist by applying the corresponding developer fluid, which removes soluble parts of the resist.

### **Lift-Off Process**

Lift-off is a method for patterning of deposited films. One method to produce patterns with sub-micrometric lateral resolution is by applying a bilayer resist [119]. In this work, a bilayer of the positive PMMA e-beam resist is used. The bottom layer is a slightly more sensitive PMMA with a lower molecular weight, while a PMMA with a higher molecular weight distribution serves as the top resist. Consequently, after e-beam exposure and development, the bottom layer is removed more rapidly than the top layer defining an undercut profile, as it is depicted in Figure 4.3. After material deposition from top, this undercut provides a region, free from deposited sidewalls that is reachable for the resist solver. PMMA is then removed in an acetone-bath using either an ultrasonic or a megasonic cleaner.

### **Alignment Markers**

In order to write multi-level patterns on a single chip, *marker* structures are used to align one layer of the lithography with other layers. The e-beam writer determines the relative position of the e-beam and patterns already existing on the substrate with respect to markers.

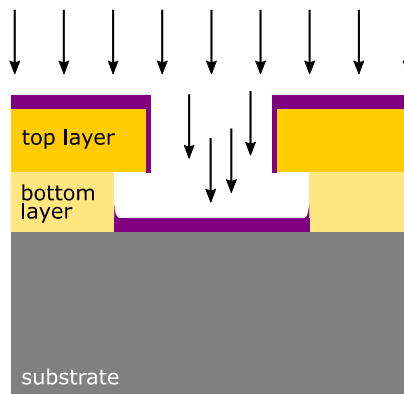


**Figure 4.3:** Sketch of the cross section of a substrate with a coating of PMMA bilayer after deposition. Material will be deposited on surfaces and sidewalls of the top layer. The undercut profile largely prevents the deposition on sidewalls of the bottom layer and below the top layer, providing a region for the contact with acetone in the lift-off process.

A common strategy is to have four markers at corners of the chip to provide translation, rotation and magnification corrections to the e-beam at each chip side. In this work, octagonal gold Au markers are used, which are fabricated by EBL, the deposition of Au by EBPVD and the lift-off process, as it has been described above.

## 4.4 Etching Techniques

Layers of materials are removed by two different etching processes based on either dry or wet etchants. In order to define patterns of structures on a substrate, some regions of a sample need to be covered by a mask to be protected from the etchant. This process involves either hard masks, e.g. other materials that persist the etchant, or patterned resists such as e-beam resists after EBL, as it has been described in the section 4.3. Etching can be chemical, physical or a combination of both processes. The chemical etching occurs isotropic in all directions, whereas the physical etching is an anisotropic process in a defined direction.

### 4.4.1 Reactive Ion Etching

Reactive ion etching (RIE) is a dry etching process. A key attribute to the RIE technique is the capability of the anisotropic chemical etching. The RIE equipment in this work (Plasmalab 100 ICP 380 from Oxford Instrument) consists of a plasma chamber with inlets for process gases. The plasma is initiated by a radiofrequency (RF) power source. Ar gas is excited by a capacitive coupled plasma (CCP) system with two electrodes that create an alternating electric field. Consequently, gas molecules dissociate, creating ions, radicals and free electrons. Free electrons take part in ionization of neutral gas atoms. Then, a DC bias voltage forms on the bottom electrode at the sample holder, which

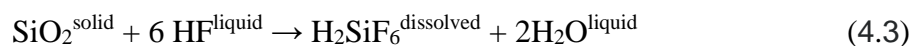
accelerates ions and radicals towards the substrate, where they react at the surface with the material and eject its molecules [120].

### **Cryogenic Etching Technique**

High quality etching of silicon is essential for the development of nano and microelectronic demonstrators and photonic devices [121]. In this work, anisotropic Si etching is one of the main fabrication steps. In order to realize Si structures with smooth sidewalls and high aspect ratios, a cryo process is used inside the RIE at sample temperatures below  $-80\text{ }^{\circ}\text{C}$  and process gases  $\text{O}_2$  and  $\text{SF}_6$ . Ions generated by plasma react chemically with Si at etching surfaces and create passivation layers of  $\text{SiO}_x\text{F}_y$ . During the process, passivation on surfaces perpendicular to the acceleration direction of ions is removed, nonetheless, they remain on sidewalls and prevent etching in the lateral direction. After heating to the room temperature, passivation layers become instable and evaporate away [121,122].

#### **4.4.2 Wet Etching**

Wet etching is a chemical process that uses aqueous solutions for removal of material from a substrate. Liquid etchants diffuse to the material, where, usually, a reduction-oxidation reaction entails the oxidation of the material and dissolves the oxidized material. Byproducts of the reaction are transported away from the reacted surface by convection or diffusion [123]. In this work, wet etching is used to undercut  $\text{SiO}_2$  layers. Therefore, samples are immersed into diluted hydrofluoric (HF) acid. The chemical reaction of the etching is described by



The etching is stopped by wet-to-wet transferring of samples from HF to deionized-water bath.

### **Critical Point Drying**

If samples of nanostructures are introduced to aqueous medium, e.g. after the wet etching with the HF acid, air (evaporative) drying needs to be avoided. Direct evaporation of liquid medium can cause deformation and collapse of free-standing structures, due to the existing surface tension. Alternatively, the critical point drying (CPD) technique is used to reduce the surface tension to zero [124,125]. A schematic of the phase diagram of the process is depicted in Figure 4.4.

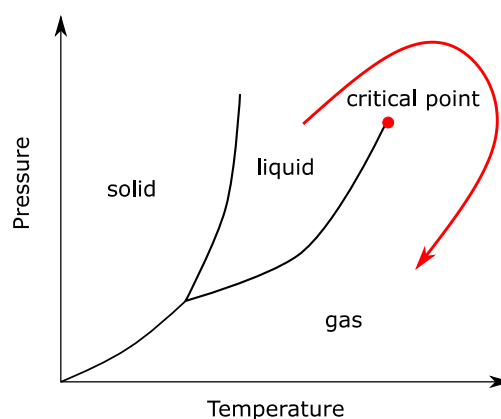


**Figure 4.4:** Schematic of the phase diagram demonstrating the fundamental of the critical point drying through a supercritical fluid phase realized above the critical pressure and temperature.

Along the boundary between liquid and vapor phases it is possible to choose a temperature-pressure combination, where liquid and vapor can co-exist and hence, have the same density. This is known as the critical point.

In the first step of the CPD, the aqueous medium is exchanged with a fluid having preferably a low critical temperature and pressure. The most common is  $\text{CO}_2$  with a critical point at around  $30\text{ }^\circ\text{C}$  achieved at a pressure of approx.  $7 \cdot 10^6\text{ N/m}^2$ .

In a CPD equipment, samples are placed in a chamber filled by liquids having a good solubility in liquid  $\text{CO}_2$ , e.g. isopropanol. Afterwards, the isopropanol is exchanged by the liquid  $\text{CO}_2$  under increased pressure. Next, the temperature is increased to above the critical temperature at a constant pressure. Hence,  $\text{CO}_2$  transforms into a supercritical fluidic. Next, the pressure is gradually decreased at a constant temperature and the supercritical fluid transforms to the gaseous form leaving a dried product [124,125].

## 4.5 Ellipsometry

Ellipsometry is an optical technique that measures a change in polarization as a polarized light beam is reflected or transmitted from a material structure. The nature of the change in the polarization depends on the thickness and the complex reflective index of the material. Figure 4.5 illustrates the setup of an ellipsometer schematically. The beam emitted from a light source is polarized by passing through a linear polarizer. After interaction with the material, the beam is reflected and goes into a second polarizer, referred to as the analyzer. Subsequently, the beam enters a detector, which converts the optical signal to an electronic signal to determine the polarization of the reflected light. The light beam with a linear polarization interacts with the material.

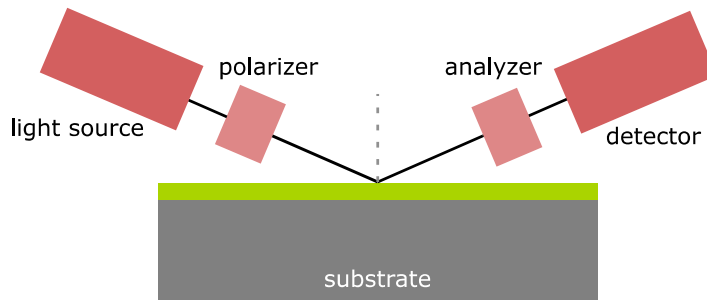


**Figure 4.5:** Schematic of a basic setup of an ellipsometer. Optical constants and the thickness of the film (indicated in green) is determined through measurement of change in the polarization of the incident light after interaction with the material.

The polarization of the output signal is compared to the input signal to determine the polarization change, which is defined by [126]

$$\rho = \tan(\Psi e^{i\Delta}) \quad (4.4)$$

where  $\Psi$  and  $\Delta$  are the amplitude ratio and the phase difference, respectively. Measurement results are presented in terms of  $\Psi$  and  $\Delta$ , as functions of the photon energy or the light wavelength. An ellipsometer is equipped with an analyzing software, through which a model is constructed to describe the structure of the sample and its properties.

## 4.6 Four-Terminal Electrical Measurement

The easiest method to measure the electrical resistivity of a material surface is by using two surface probes, where the electrical current  $I$  is sent through one probe spreads on the surface and is collected through a second probe. The electrical resistance  $R_{\text{tot}}$  is calculated by combining the measured current and voltage  $V$  as  $R_{\text{tot}} = V/I$ . However,  $R_{\text{tot}}$  is not the real electrical resistance of the material surface. It also includes the parasitic contact resistance, i.e. the electrical resistance between the material and the probe touching the surface and the parasitic spreading resistance caused by the current flowing into the sample surface.

In contrast to the two-point probe measurement, the four-terminal method uses four electrical probes, as depicted in Figure 4.6. In this method, two outer probes carry the electrical current, and two additional probes are placed in between, which measure the voltage drop across the material surface. Hence, parasitic resistances, measured by the two-point probe method are eliminated [127].

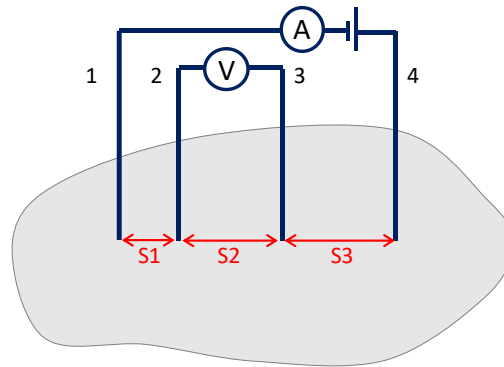


**Figure 4.6:** Schematic of a four-point-probe setup to determine material surface resistivity. Probes 1 and 2 carry the electrical current, whereas probes 2 and 3 measure the voltage.

The electrical resistivity  $\rho$  of a semi-infinite volume of the material is determined by [127]

$$\rho = \frac{V}{I} \frac{2\pi}{\left(\frac{1}{s_1} + \frac{1}{s_3} - \frac{1}{s_1 + s_2} - \frac{1}{s_2 + s_3}\right)} \quad (4.5)$$

where  $s_1$ ,  $s_2$  and  $s_3$  are point spacings between probes, as it is depicted in Figure 4.6.

For a measurement setup with equidistance probes, i.e.  $s_1 = s_2 = s_3 = s$ , the relation 4.5 simplifies to

$$\rho = \frac{V}{I} 2\pi s \quad (4.6)$$

In practice, resistivity measurements are not applied on a semi-finite volume of materials but on a slab or slice of finite thickness. Thus, the real electrical resistivity differs from that in relation 4.6. In fact, the real surface resistivity of the material  $\rho_r$  is defined by [128]:

$$\rho_r = \rho / C.D. \quad (4.7)$$

where  $C.D.$  is the correction divisor for specific cases depending on factors such as the thickness of the substrate, the distance between probes, edge effects, etc. [128–130]. For the case that the film thickness  $t$  is less than half the probe spacing  $s$ , the correction factor is expressed by  $C.D. \approx (2\ln 2)s/t$  [128].



# 5 Fabrication of Vanadium Dioxide-Based Nanostructures

The focus of interest of this thesis is to investigate multifunctional properties of VO<sub>2</sub> at the nanoscale. The gained knowledge promotes the development of novel nanodevices based on VO<sub>2</sub> thin films. To these aims, as a main context of this work, reliable process flows for the flexible fabrication and the tuning of VO<sub>2</sub> nanostructures are established. These techniques are applied for scaling down of the lateral size of structures to the film grain size and to enable systematic studies and characterizations.

First, in section 5.1, the fabrication method of VO<sub>2</sub> films and V<sub>1-x</sub>M<sub>x</sub>O<sub>2</sub> films doped by a third material M is introduced. The fabrication of VO<sub>2</sub>- and V<sub>1-x</sub>M<sub>x</sub>O<sub>2</sub>-based nanostructures is achieved by two main processes. The procedure in section 5.2 describes the method based on the nanomachining of a SOI wafer before deposition of films on created structures. An alternative fabrication method is based on the direct nanomachining of VO<sub>2</sub>-based films on Si-based substrates, which is explained in section 5.3.

Before starting fabrications, samples are cleaned in an acetone bath, then, in an isopropanol bath by using an ultrasonic cleaning device. To prevent recontamination, the whole nanofabrication is performed inside a clean room. The quality of fabrication results is controlled after each process step through different techniques. Thickness of deposited films and spin-coated resists are determined by ellipsometry, as it has been previously described in section 4.5. The morphology of films and the quality of structures require to be controlled by inspection techniques, such as by light microscopy or SEM.

## 5.1 Vanadium Dioxide-Based Thin Films<sup>1</sup>

The fabrication of VO<sub>2</sub> thin films is quite sensitive to deposition parameters, due to the complex phase diagram of VO<sub>x</sub> with different stoichiometries [131]. Synthesizing of pure VO<sub>2</sub> demands for the precise control of the stoichiometry to avoid the formation of oxygen defects and other stoichiometric phases by modifying growth conditions [21,131].

Crystallinity and morphology of VO<sub>2</sub> films are other important properties, which define characteristics of the metal-insulator transition [132].

---

<sup>1</sup> Presented results in this section are partially reproduced from [S. Rastjoo, X. Wang, A. Ludwig, M. Kohl, Top-down fabrication and transformation properties of vanadium dioxide nanostructures, J. Appl. Phys. 125 (2019) 225104.], with the permission of AIP Publishing.

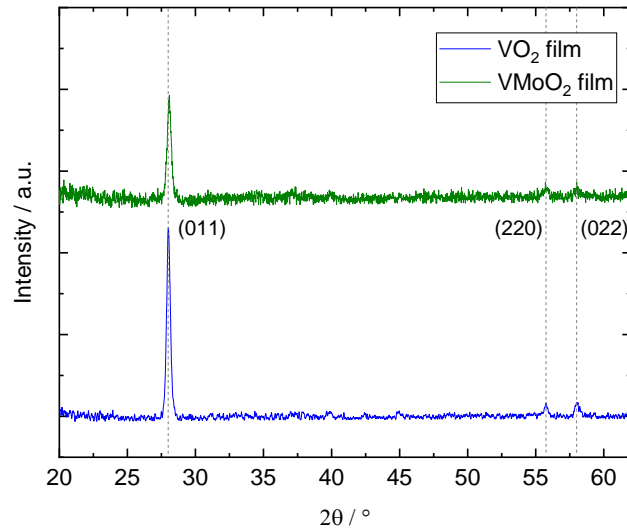


**Figure 5.1:** XRD patterns of VO<sub>2</sub> and VMoO<sub>2</sub> films. Peaks at  $2\theta = 28^\circ$ ,  $55.6^\circ$  and  $57.7^\circ$  correspond to the (011), (220) and (022) crystal-plane orientations of the monoclinic phase M1, respectively. Adapted from [133].

For applications, desired electrical, mechanical and optical properties can be adapted through engineering of deposition parameters and the deliberate modification of film properties.

VO<sub>2</sub> films are fabricated by the reactive magnetron sputtering by our collaborators at Ruhr-Universität Bochum (RUB). VO<sub>2</sub> films are deposited using a vanadium V target with the purity of 99.95 %. The substrate is placed on a rotating plate that is heated to 520 °C. After the sputter chamber is evacuated to  $2 \cdot 10^{-5}$  Pa, 80 sccm of Ar is introduced into the chamber. Then, the pressure is equilibrated to 1.3 Pa. After 5 min of pre-sputtering, the pressure is decreased to 0.4 Pa for the main deposition. Pulsed dc power of 300 W is applied to the target at a pulsing frequency of 10 kHz and a reverse time of 5  $\mu$ s. The O<sub>2</sub> flow rate is dynamically controlled by a PEM system [134]. After deposition, the sample is cooled down to room temperature in vacuum [133].

Fabrication of doped films V<sub>1-x</sub>M<sub>x</sub>O<sub>2</sub> is realized at RUB by the co-sputtering of V and a second metal target under similar process conditions as for pure VO<sub>2</sub> films. V<sub>0.99</sub>Mo<sub>0.1</sub>O<sub>2</sub> (hereafter referred to as “VMoO<sub>2</sub>”) films are deposited by introducing the molybdenum Mo content (1 at. %) through a contamination effect using a shutter. Chemical compositions of films are determined by the Rutherford backscattering spectroscopy (RBS) measurements and crystalline structures of films are studied by the X-Ray diffraction (XRD) crystallography. Figure 5.1 shows XRD patterns of fabricated VO<sub>2</sub> and VMoO<sub>2</sub> films. A dominant diffraction peak occurs at about  $2\theta = 28^\circ$ , which corresponds to the (011) crystal-plane of the monoclinic phase M1.

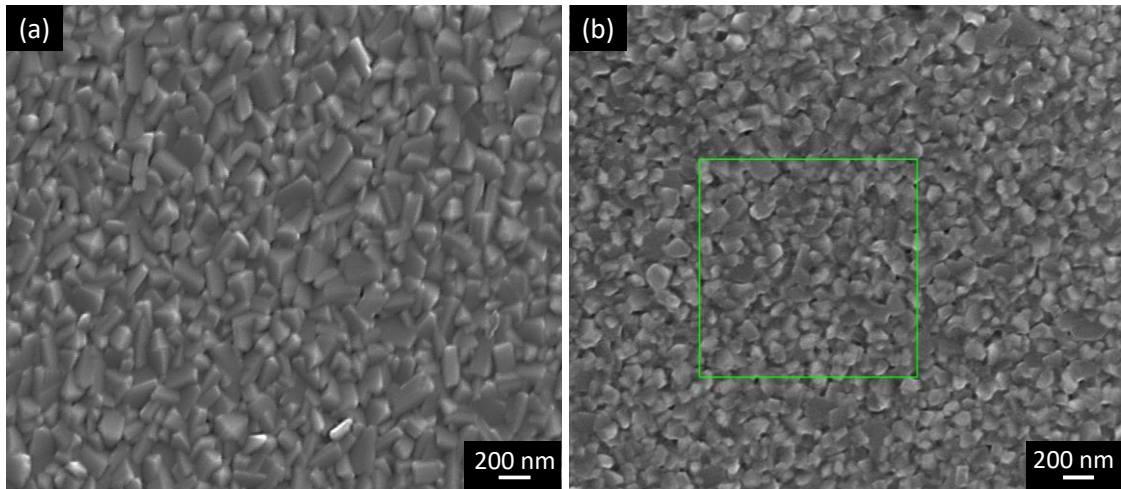


**Figure 5.2:** Scanning electron micrographs of as-deposited films on SiO<sub>2</sub>/Si substrates. (a) A VO<sub>2</sub> film with a grain size of  $125 \pm 5$  nm, and (b) a VMOO<sub>2</sub> film with a grain size of  $100 \pm 5$  nm. The green square indicates a randomly chosen area of  $1.5 \mu\text{m} \times 1.5 \mu\text{m}$ , within which the averaged grain sizes of films are determined.

The quality of fabricated films are investigated by a SEM. The average size of grains is evaluated within a reference area of  $2.25 \mu\text{m}^2$  in SEM images. Figure 5.2a shows the surface of a VO<sub>2</sub> film with a thickness of 100 nm indicating a dense polycrystalline structure with an averaged grain size of  $125 \pm 5$  nm. Whereas in Figure 5.2b, the VMOO<sub>2</sub> film having the same thickness of 100 nm exhibits a less dense surface structure with an averaged grain size of  $100 \pm 5$  nm [133].

Thicknesses of films are determined either from SEM images of cross sections of samples or by optical ellipsometry measurements, as it has been described in section 4.5. Optical properties of films are related to microstructures and the surface roughness of films. Fabricated films in this work indicate typically rough surfaces, which need to be considered in ellipsometry analyses. Further details on ellipsometry models describing the construction of samples are presented in Appendix A.

## 5.2 Nanomachining of Substrate Prior to Film Deposition<sup>2</sup>

The top-down fabrication method introduced in the following is based on the nanomachining of a SOI wafer to realize free-standing structures prior to the film deposition. The process flow on the SOI chip having a 340-nm Si device layer and a 2-μm

<sup>2</sup> Presented results in this section are partially reproduced from [S. Rastjoo, X. Wang, A. Ludwig, M. Kohl, Top-down fabrication and transformation properties of vanadium dioxide nanostructures, J. Appl. Phys. 125 (2019) 225104.], with the permission of AIP Publishing.

SiO<sub>2</sub> box layer is depicted in Figure 5.3. In the first step, the Si device layer is structured by the EBL. Before spin-coating, the substrate is heated to around 120 °C for roughly 10 min to remove adsorbed water from its surface. In order to improve resist adhesion, a monolayer of TI Prime adhesion promoter is spin-coated, followed by spin-coating of a negative tone resist with a thickness of approx. 200 nm. The thickness of the resist is adjusted to be thick enough to withstand the subsequent etching process [135]. After exposure to the e-beam and development, patterns of structures are transferred to the resist layer (Figure 5.3b). For the development of the resist, a spray developer is used, where the sample is placed on a rotating plate and the developer mixed with deionized water is sprayed using the air pressure. The development is stopped with spraying deionized water, followed by spin drying. Next, the Si layer is etched by RIE using process gases HBr and O<sub>2</sub> at a temperature of 60 °C (Figure 5.3c). The remaining resist is removed by an acetone immersion bath, then, rinsed by isopropanol. In the next step, the buried oxide layer is removed by wet-etching using hydrofluoric (HF) acid, followed by a critical point drying step (refer to section 4.4.2) to avoid sticking effects (Figure 5.3d). The HF-acid etching rate in the lateral direction is determined to be 1.3 μm/h. Based on this method, free-standing Si nanostructures with high aspect ratios are fabricated [133,135]. Afterwards, Si thermal oxide is grown on the substrate, followed by the sputtering of V<sub>1-x</sub>M<sub>x</sub>O<sub>2</sub> film from top onto the sample (Figure 5.3e) [133]. Deposition of films on the surface of the thermal SiO<sub>2</sub> leads to the texturing with the c<sub>R</sub>-axis lying in the plane of substrate, which enables the actuation based on the martensitic transformation in VO<sub>2</sub> [44,136]. Figure 5.4a shows a top-view SEM image of a double-beam structure fabricated by this method. Due to the introduced tension between layers after film deposition, the structure is deformed compared to the design pattern, as it is shown in the schematic 3D illustration in Figure 5.3e. The side-view SEM image in Figure 5.4b reveals that, although the VO<sub>2</sub> is deposited from top, the film grows also on side walls of structures, which impede out-of-plane actuation. Furthermore, this process is not appropriate for the fabrication of free-standing VO<sub>2</sub> structures, since the release of the VO<sub>2</sub> film from the substrate is challenging due to side-wall depositions.

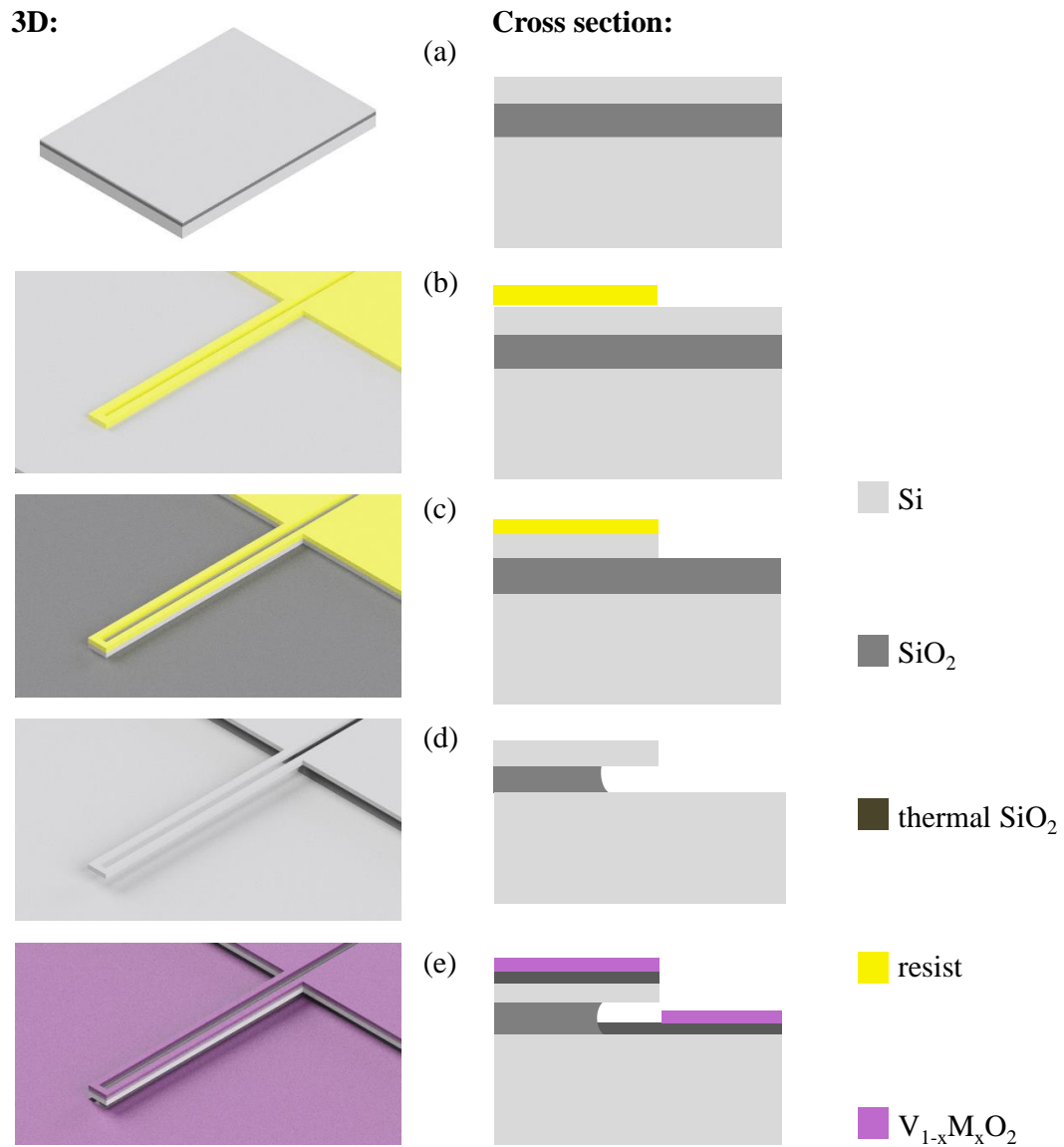


**Figure 5.3:** Schematic of the fabrication process of free-standing structures based on  $V_{1-x}M_xO_2$  films. (a) Starting platform is a SOI wafer. (b) Patterns of structures, here double-beams, are transferred to the resist by the e-beam lithography. (c) Si layer is etched inside a RIE chamber by using HBr and O<sub>2</sub> process gases. (d) Free-standing structures are achieved through the isotropic etching of the SiO<sub>2</sub> buried layer. (e) After growth of a thin layer of Si thermal oxide,  $V_{1-x}M_xO_2$  films is sputtered on top of structures.

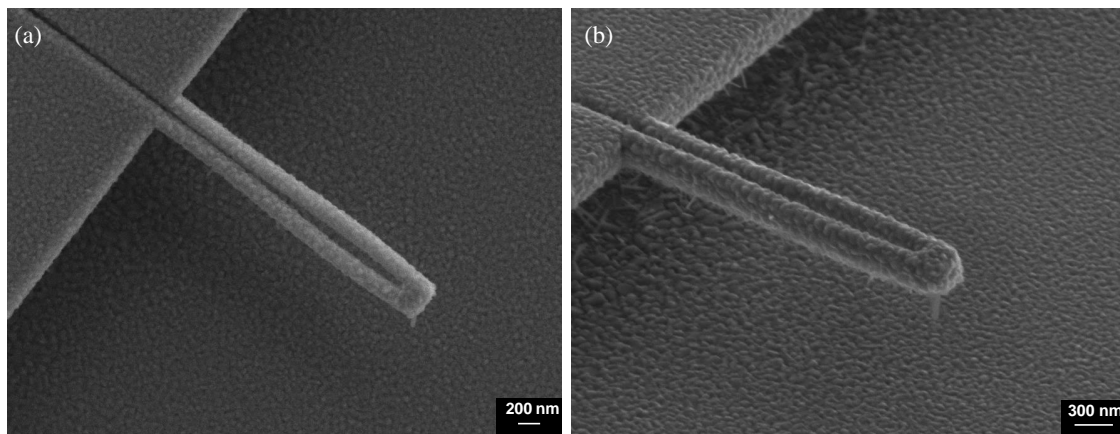


**Figure 5.4:** (a) Top-view and (b) side-view scanning electron micrographs of a free-standing double-beam fabricated by the deposition of a 100-nm thick  $\text{VO}_2$  film on the pre-structured SOI substrates.

### 5.3 Direct Nanomachining of Vanadium Dioxide-Based Films<sup>3</sup>

In this section, a top-down process flow is introduced for fabrication of free-standing structures based on the direct nanomachining of deposited  $\text{V}_{1-x}\text{M}_x\text{O}_2$  films. Fabrication steps are schematically depicted in Figure 5.5. The initial substrate is a Si wafer having a thermally grown  $\text{SiO}_2$  with a thickness of 1.5  $\mu\text{m}$  on top.

The  $\text{V}_{1-x}\text{M}_x\text{O}_2$  film is deposited on the substrate at RUB by dc-pulsed reactive magnetron sputtering (Figure 5.5a), as previously described in section 4.2. The nanofabrication begins with EBL. Before spin-coating, the adsorbed water on the surface of the substrate is removed through heating it on a hotplate to around 120  $^\circ\text{C}$  for about 10 min. After cooling of the substrate to room temperature, a monolayer of TI Prime adhesion promoter is spin-coated to improve the adhesion of the resist on the substrate. Subsequently, a layer of a negative-tone resist with a thickness of approx. 330 nm is spin-coated. After exposure by the e-beam, the resist is developed by a spray developer. Development is stopped by spraying of deionized water and dry spinning of the substrate (Figure 5.5b). The process step in Figure 5.5c demonstrates the pattern transfer from the resist to the  $\text{V}_{1-x}\text{M}_x\text{O}_2$  film by the RIE at room temperature using  $\text{SF}_6$  and  $\text{O}_2$  as process gases. Etching rate depends on the chemical composition of films and is approx. 1.5 nm/s and 4.5 nm/s for  $\text{VO}_2$  and  $\text{VMoO}_2$  films, respectively.

<sup>3</sup> Presented results in this section are partially reproduced from [S. Rastjoo, X. Wang, A. Ludwig, M. Kohl, Top-down fabrication and transformation properties of vanadium dioxide nanostructures, *J. Appl. Phys.* 125 (2019) 225104.], with the permission of AIP Publishing.

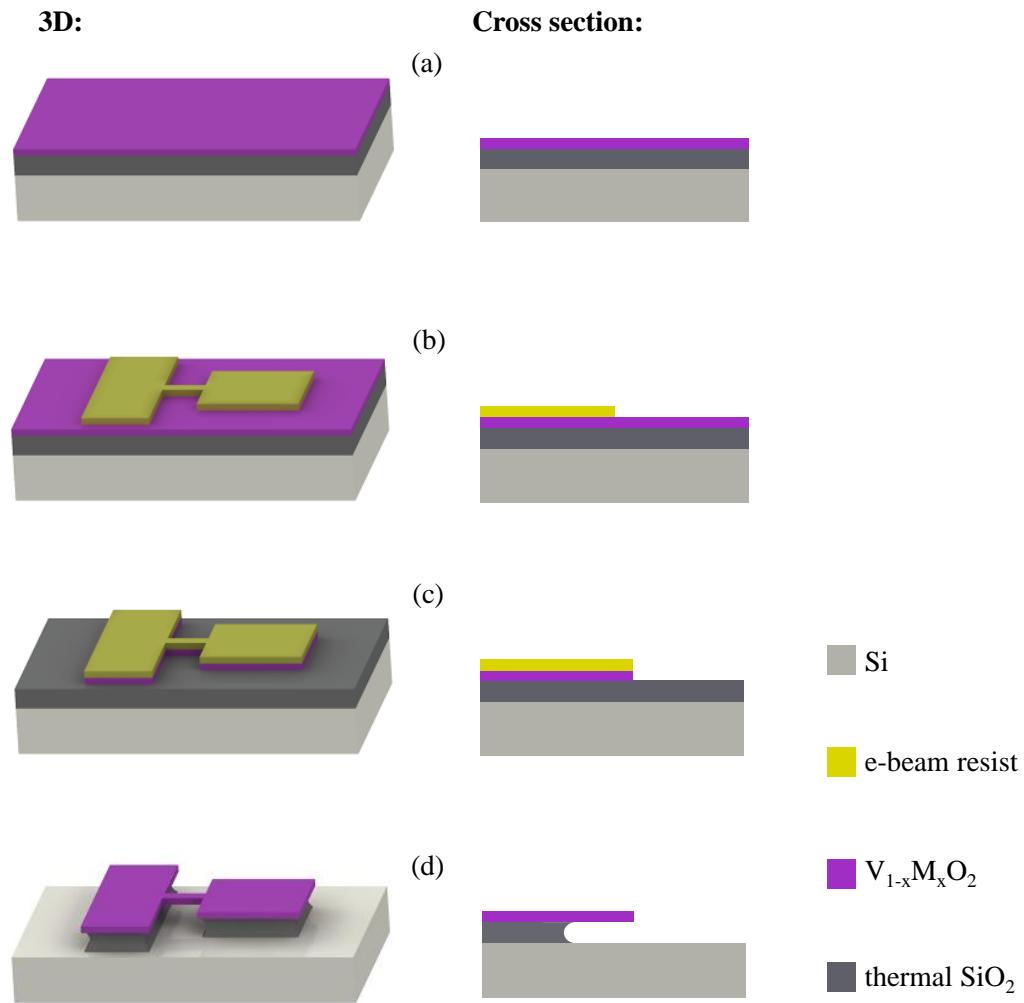


**Figure 5.5:** Schematic of the fabrication flow of the direct nanomachining of as-deposited  $V_{1-x}M_xO_2$  films. After (a) reactive magnetron sputtering of the  $V_{1-x}M_xO_2$  film on the  $SiO_2/Si$  substrate, (b) patterns of structures, here nanobridges, are transferred to the resist by the e-beam lithography. (c)  $V_{1-x}M_xO_2$  film is etched by the RIE. (d) Undercut of the thermal  $SiO_2$  by the fluidic HF acid creates free-standing structures.

Resist is removed, first, through an ultrasonic cleaning inside an acetone bath and the subsequent rinsing by the isopropanol, second, by stripping of resist residuals using the  $O_2$  plasma. Afterwards, the buried oxide layer is etched by immersing the substrate into the HF acid bath (Figure 5.5d). The etching time is adjusted with respect to the lateral width of free-standing structures by considering a lateral etching rate of  $1.3 \mu\text{m/h}$ . Samples are then dried by the critical point drying (refer to the section 4.4.2). Fabricated nanostructures through this method are shown in Figure 5.6. Based on this method, free-standing structures of  $V_{1-x}M_xO_2$  films are fabricated with lateral sizes down to 100 nm indicating sharp edges and uniform sidewalls. The accuracy of patterns transfer to the film is estimated from SEM images to be below 10 nm [133].

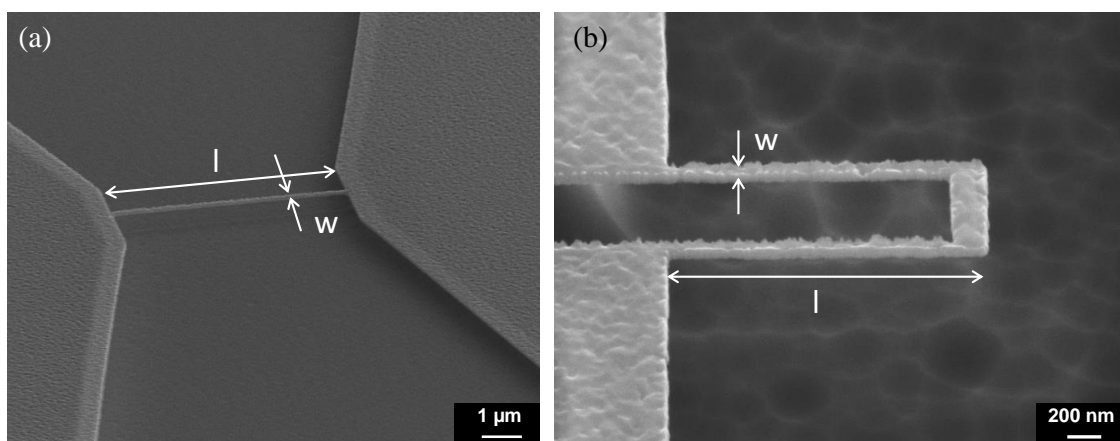


**Figure 5.6:** SEM images of  $\text{VMO}_2$  free-standing structures fabricated by the direct nanomachining of deposited films on  $\text{SiO}_2/\text{Si}$  substrates. (a) A nanobridge with the lateral width of  $w = 100 \text{ nm}$  and the length of  $l = 5 \text{ }\mu\text{m}$ . (b) A Double-beam structure with  $w = 100 \text{ nm}$  and  $l = 2 \text{ }\mu\text{m}$ .

### 5.3.1 Fabrication of Bimorph Nanoactuators

Nanoactuators are realized by fabricating  $\text{Cr}/\text{V}_{1-x}\text{M}_x\text{O}_2$  bimorph structures. Therefore, double-beams depicted in Figure 5.6b, are deposited from top by chromium Cr using the electron beam physical vapor deposition (refer to the section 4.1). A  $\text{Cr}/\text{V}_{1-x}\text{M}_x\text{O}_2$  thickness ratio of 0.37 is considered to gain a maximum out-of-plane actuation, calculated from the beam bending theory of Timoshenko (see Appendix B) [137]. Figure 5.7c shows a fabricated  $\text{Cr}/\text{VMO}_2$  double-beam having a lateral beam width and a length of 100 nm and 3 μm, respectively. Deposition of Cr occurs at temperatures higher than the martensitic transformation of  $\text{VMO}_2$ , when it is in the austenite phase with smaller in-plane lattice constants. After the sample cools down to room temperature, the release of the built-in stress causes the bimorph to bend towards the Cr side [44,138].

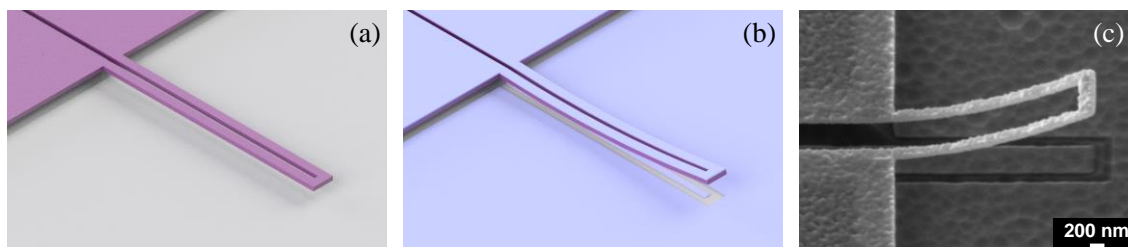


**Figure 5.7:** (a, b) Schematics of the fabrication of a bimorph double-beam nanoactuator. (a) A free-standing  $\text{V}_{1-x}\text{M}_x\text{O}_2$  double-beam generated by the direct nanomachining of the  $\text{V}_{1-x}\text{M}_x\text{O}_2$  film on a  $\text{SiO}_2/\text{Si}$  substrate. (b) The  $\text{Cr}/\text{V}_{1-x}\text{M}_x\text{O}_2$  actuator is realized after deposition of Cr on top of the substrate. (c) Scanning electron micrograph of a fabricated  $\text{Cr}/\text{VMO}_2$  nanoactuator with a lateral beam width and a length of 100 nm and 3 μm, respectively. The thickness of Cr and  $\text{VMO}_2$  layers are 37 and 100 nm, respectively.

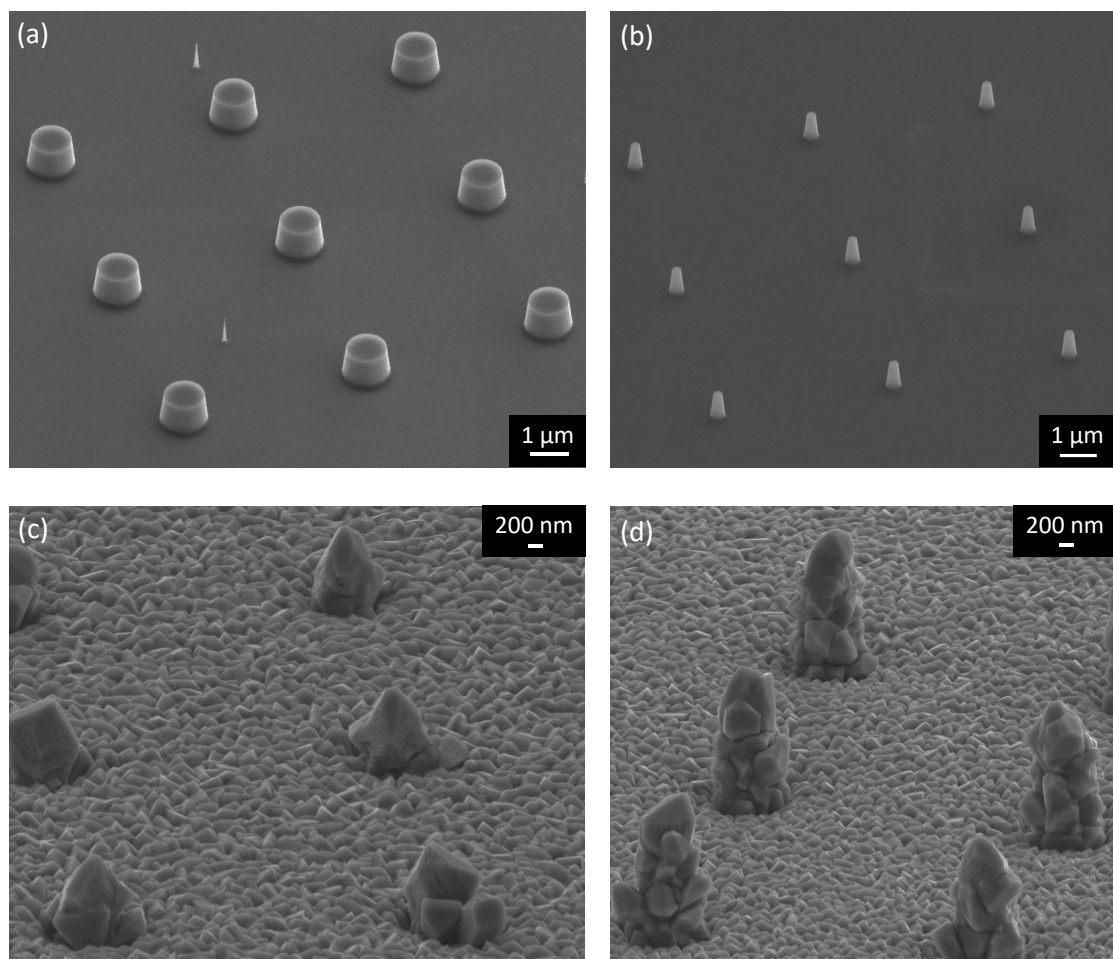


**Figure 5.8:** Scanning electron micrographs of (a) Si pillars with diameters of  $d = 1 \mu\text{m}$  and (b) Si nanopillars with  $d = 100 \text{ nm}$ . Through deposition from top, (c) VO<sub>2</sub> single crystals grow on top of Si nanopillars. (d) Oligocrystalline-like structures are realized for a longer time of the deposition. Crystal growth on Si nanopillars with  $d = 100 \text{ nm}$  results in large grains having diameters of around  $500 \text{ nm}$ .

## 5.4 VO<sub>2</sub> Nanopillars

In addition to top-down fabrications described in previous sections, another approach to realize nanostructures is based on bottom-up processes. The fabrication method comprises the deposition of the VO<sub>2</sub> film on pre-structured nanopillars on a typical Si wafer. Si nanopillars with different diameters and high aspect ratios can be fabricated by EBL and RIE [139]. The layout of the design consists of circles having diameters from 100 to 1000 nm. First, a layer of a negative resist HSQ is spin-coated on a Si substrate. After e-beam exposure, the resist is developed inside the diluted 25 % tetramethylammonium hydroxide (TMAH) bath. Subsequently, the development is stopped with rinsing of the substrate, first, with isopropanol, then, with DI-water. Next, the Si is etched by the cryogenic technique, as it has been explained in section 4.4.1.

Resist residuals are removed by immersing the substrate into the 5 % HF-acid bath. Figure 5.8 a, b show SEM images of fabricated Si pillars. Afterwards, the VO<sub>2</sub> film is deposited onto the sample at RUB by the reactive magnetron sputtering, as described before in section 4.2.

The SEM image in Figure 5.8c depicts preliminary fabricated VO<sub>2</sub> single-crystallins on specific positions defined through Si nanopillars on the substrate. Obviously, growth of VO<sub>2</sub> on Si nanopillars occurs with larger grains compared to the film on the planar substrate. By increasing the deposition time, thus, increasing the thickness, Oligocrystalline-like structures are fabricated, as shown in Figure 5.8d. The size of grains can be attuned by varying diameters of Si pillars and deposition parameters.

### 5.5 Summary

VO<sub>2</sub>-based thin films are fabricated at RUB by the reactive magnetron sputtering. This method allows for the flexible fabrication of doped films such as VMOO<sub>2</sub> films to tune the metal-insulator transformation properties. Two top-down process flows based on the EBL and the RIE are investigated for fabricating free-standing VO<sub>2</sub>-based nanostructures. The method of sputtering of VO<sub>2</sub> on pre-structured SOI substrates indicates deposition on sidewalls. In contrast, the process of the direct nanomachining of deposited films on SiO<sub>2</sub>/Si substrates results in nanostructures having sharp edges and smooth sidewalls. This method benefits from the precise transferring of design patterns to the film, which enables downscaling to the lateral width of 100 nm. In another approach, VO<sub>2</sub> films are deposited on Si nanopillars. Based on this fabrication method, VO<sub>2</sub> nanopillars are fabricated reaching the scale of grain size and oligocrystalline structures. Bimorph nano-actuators are fabricated through a final step of the deposition of Cr on top of samples with free-standing structures using electron beam physical vapor deposition. Quality of fabricated structures depend on the precision of each process step and is investigated by different techniques, mainly by a SEM. More details on challenges of the nanofabrication can be found in Appendix C.

# 6 Electrical and Mechanical Performance of Vanadium Dioxide-Based Nanostructures

Electrical and mechanical characteristics of VO<sub>2</sub>-based nanostructures are investigated by temperature-dependent measurements. The focus of interest is to investigate the influence of down-scaling on the transformation properties by reducing lateral widths down to the grain size.

In section 6.1, electrical resistance characteristics of VO<sub>2</sub>-based thin films are discussed. Next, the measurement setup inside a thermostat is presented for experiments on the temperature-dependent electrical resistance. Electrical characteristics of a series of free-standing nanobridges are systematically investigated with decreasing lateral widths. In section 6.2, out-of-plane deflections of VO<sub>2</sub>-based nanoactuators are studied in-situ inside a SEM. Details of in-situ measurement setups are introduced including the development of a micro heating-cooling stage (MHCS) for homogenous temperature control of samples inside a SEM and Joule heating of nanostructures using nanomanipulators.

## 6.1 Electrical Properties<sup>1</sup>

### 6.1.1 Temperature-Dependent Electrical Resistance Characteristics of VO<sub>2</sub>-Based Films

In this work, electrical characteristics of VO<sub>2</sub>-based thin films are investigated. Films are deposited by reactive pulsed dc sputtering as described in section 5.1. Temperature-dependent electrical resistances are determined inside a thermostat by a four-terminal setup using four equidistant probes with spacing of around 1500 μm. Measurements are performed under quasi-stationary conditions by allowing sufficient waiting time between measurement points. The pressure of the measurement chamber is reduced to around 10<sup>-6</sup> mbar to prevent the oxidation of the film as well as the ice formation on the sample surface due to the air humidity at temperatures below 0 °C. Moreover, the heat transfer via convection is negligible in vacuum, which is essential for keeping a constant set-temperature during measurements.

---

<sup>1</sup> The main part of presented results in this chapter are reproduced from [S. Rastjoo, X. Wang, A. Ludwig, M. Kohl, Top-down fabrication and transformation properties of vanadium dioxide nanostructures, J. Appl. Phys. 125 (2019) 225104.], with the permission of AIP Publishing.

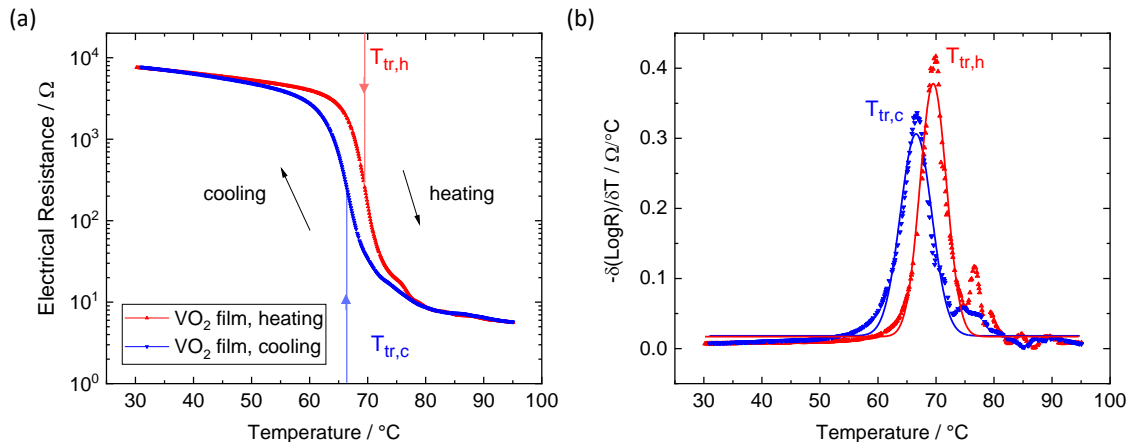


**Figure 6.1:** (a) Electrical resistance of a VO<sub>2</sub> film as a function of temperature. The phase transformation temperatures upon heating  $T_{tr,h} = 69.5$  °C and cooling  $T_{tr,c} = 66.4$  °C are indicated with red and blue arrows, respectively. (b) Transition temperatures are determined by the maximum of Gaussian fit of the first derivative of electrical resistance characteristics. Adapted from [133].

Electrical characteristic of a VO<sub>2</sub> thin film is depicted in Figure 6.1a. The abrupt change in the electrical resistance is in-line with reported results on bulk samples and films showing the semiconductor-metal transition [20,81,140]. The initial temperature-dependent drop of electrical resistance reflects the semiconducting behavior at low temperatures. Phase transformation temperatures of heating ( $T_{tr,h}$ ) and cooling ( $T_{tr,c}$ ) curves are determined from the peak position of Gaussian fit of the first derivative of electrical resistance characteristics on a logarithmic scale by  $-\delta(\log R)/\delta T$ , as indicated in Figure 6.1b.

Figure 6.2 shows the temperature-dependent electrical resistance for a VO<sub>2</sub> film and V<sub>1-x</sub>M<sub>x</sub>O<sub>2</sub> films. As it can be seen, the phase transformation properties of films, i.e. the hysteresis and transition temperatures, clearly alter by doping of films with a transient metal M such as Molybdenum (Mo) and Tungsten (W). Table 6.1 summarizes phase transformation properties of fabricated films in this work compared to those in literatures. In the following, properties of the VO<sub>2</sub> and the VMoO<sub>2</sub> films are discussed in detail.

As given in Table 6.1, the fabricated polycrystalline VO<sub>2</sub> film in this work indicate a transition temperature of  $T_{tr,h} = 69.5$  °C, which is slightly higher than previously reported value of 66 °C for a single crystal VO<sub>2</sub> and of 64 °C for an epitaxial VO<sub>2</sub> film [27,141]. This result can be attributed to the built-in stress in the film due to sputtering conditions and can be explained using Clausius Clapeyron relation (equation 2.2). By considering a Clausius–Clapeyron dependency of  $1.2 \times 10^{-2}$  K/MPa [141], a transition temperature shift of 4.5 K leads to a stress of about 370 MPa.

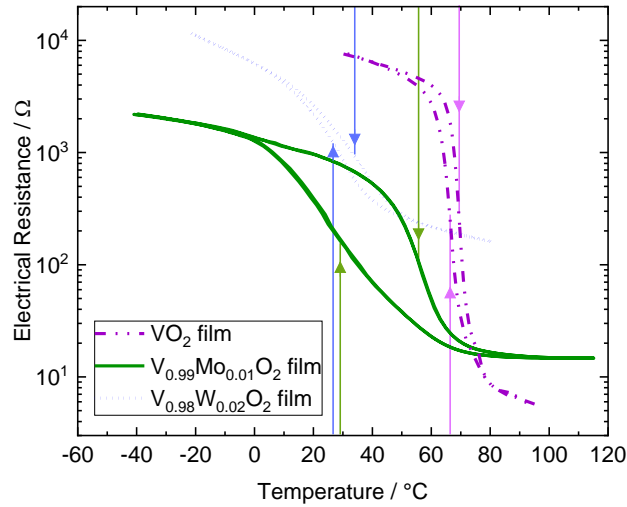


**Figure 6.2:** Electrical resistance as a function of temperature for a  $\text{VO}_2$ ,  $\text{VMoO}_2$  and  $\text{VWO}_2$  film. By doping of films with a third material, their transformation characteristics can be tuned. Transition temperatures for heating and cooling traces are indicated by arrows.

For the sputtered  $\text{VMoO}_2$  film in this work, transition temperatures are determined to be  $T_{\text{tr,h}} = 55.7 \text{ }^\circ\text{C}$  and  $T_{\text{tr,c}} = 29.1 \text{ }^\circ\text{C}$ , which indicate a shift to lower temperatures compared to values for the  $\text{VO}_2$  film. This effect is explained by the substitution of V by Mo, which may break V-V pairs causing local distortion around the added elements [70] and introducing extra electrons [142] to promote the transformation of  $\text{VO}_2$ .

The electrical resistance ratios  $R_{\text{min}}/R_{\text{max}}$  of  $\text{VO}_2$ -based films are listed in Table 6.1.  $R_{\text{min}}$  and  $R_{\text{max}}$  are the minimum and maximum electrical resistance values at the resistance drop, respectively. For the  $\text{VO}_2$  film in this work, the electrical resistance ratio is determined to be  $R_{\text{min}}/R_{\text{max}} = 7.4 \times 10^{-4}$ , which is in-line with values for polycrystalline films in previous studies [143,144]. In comparison, electrical resistance ratios of  $\text{VO}_2$  single crystals and epitaxially grown films are in the order of  $10^{-5}$  [27,141]. For the sputtered  $\text{VMoO}_2$  film, the ratio of  $R_{\text{min}}/R_{\text{max}} = 6.7 \times 10^{-4}$  is about one order of magnitude smaller compared to the resistance ratio of the  $\text{VO}_2$  film. This reduction can be explained by the high-valence cations  $\text{Mo}^{6+}$  that introduce additional electrons to the film and, accordingly, increases the electron concentration of  $\text{VO}_2$  in semiconductor state [142].

In Table 6.1, the transition hysteresis width ( $\Delta T$ ) is defined as the difference between  $T_{\text{tr,h}}$  and  $T_{\text{tr,c}}$ . The full width at half maximum (FWHM) of Gaussian fits of the heating traces are determined to quantitatively describe the phase transition width. The present  $\text{VO}_2$  film exhibits a narrow hysteresis with  $\Delta T = 2.9 \text{ K}$  and a FWHM of  $5.4 \text{ K}$ . These values are comparable with previous reports for polycrystalline films with  $\Delta T = 2.2 \text{ K}$  [143] and FWHM of  $6 \text{ K}$  [144]. The  $\text{VMoO}_2$  film shows an unexpected hysteresis with  $\Delta T = 26.6 \text{ K}$  and a FWHM of  $18 \text{ K}$ .

**Table 6.1:** Transformation properties of VO<sub>2</sub>-based films [133].

Sample	T <sub>tr,h</sub> /°C	T <sub>tr,c</sub> /°C	ΔT/K	FWHM/K	R <sub>min</sub> /R <sub>max</sub>
polycrystalline VO <sub>2</sub> film [this work]	69.5	66.4	2.9	5.4	7.4*10 <sup>-4</sup>
polycrystalline VMO <sub>2</sub> film [this work]	55.7	29.1	26.6	18	6.7*10 <sup>-3</sup>
polycrystalline VWO <sub>2</sub> film [this work]	34	26.7	7.3	24.6	1.4*10 <sup>-2</sup>
polycrystalline VO <sub>2</sub> film [144]	71	...	-	6	6*10 <sup>-4</sup>
polycrystalline VO <sub>2</sub> film [143]	60	...	2.2	...	4.4*10 <sup>-4</sup>
single crystal VO <sub>2</sub> film [141]	66	...	0.5-1	...	1*10 <sup>-5</sup>
epitaxial VO <sub>2</sub> film [27]	64	...	3.9	...	1.1*10 <sup>-5</sup>

The transformation hysteresis can be described according to a study by Lopez *et al.* [145], where they show that the VO<sub>2</sub> phase transformation is associated with heterogeneous nucleation processes, driven by extrinsic defects in films. The hysteresis originates from the nucleation barrier during the phase transformation, and its width is correlated to the microstructure and impurities of the film. For instance, VO<sub>2</sub> films with a small grain size in the range of 100 nm and below indicate a broader transformation hysteresis [145], while elemental addition could reduce the hysteresis width, due to increased defect-induced nucleation sites in the film [142,146,147]. In the present study, the polycrystalline VO<sub>2</sub> film indicates a broader hysteresis width ΔT compared to that of VO<sub>2</sub> single crystal of less than 1 K, due to the small constituent grains. Nevertheless, the VMO<sub>2</sub> film exhibit a wider hysteresis width, which diverges from previous studies. For instance, Liu *et al.* [142] reported that the hysteresis width is monotonically decreased from 7.7 K for a VO<sub>2</sub> film to 1.6 K for a Mo-doped VO<sub>2</sub> film with 12.2 at.%. In Hanlon's study [148], the hysteresis width is narrowed to less than 2 K for 1 at.% Mo. For a better understanding of the transformation hysteresis characteristics, the morphology of films needs to be taken into account. According to SEM images in Figure 5.2, the VMO<sub>2</sub> film has smaller grains with the average size of ~ 100 nm compared to the VO<sub>2</sub> film with the average grain size of ~ 125 nm. Further, the VMO<sub>2</sub> film shows an enhanced surface roughness with a less dense arrangement of grains. This considerably affects the phase transformation and could result in broadening of the hysteresis [133].

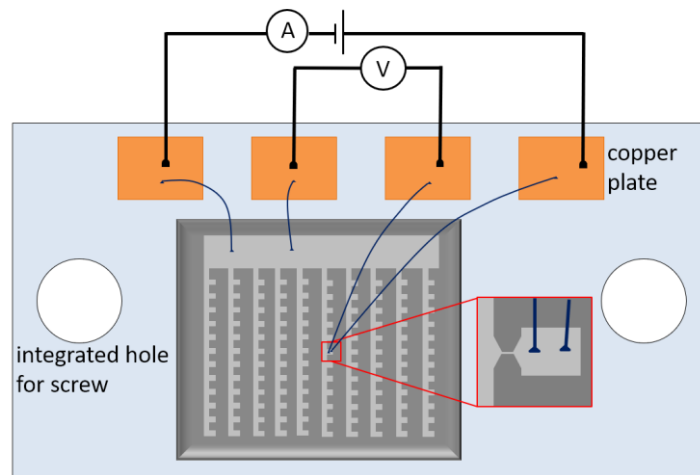


**Figure 6.3:** Schematic of the setup inside a thermostat including electrical connections for four-terminal electrical measurements. Sample is attached on a ceramic plate, which is fixed by screws inside the thermostat. The layout size is  $10 \times 10 \text{ mm}^2$  and consists of nanobridges and contact pads. Nanobridges are electrically connected to four copper sheets via wire bonding. The connection to source and measurement units is provided by a four-port cable, which is soldered to copper sheets.

### 6.1.2 Temperature-Dependent Electrical Resistance of VMoO<sub>2</sub> Nanobridges

In the following, electrical characteristics of free-standing VMoO<sub>2</sub> nanobridges are presented. The influence of the nanofabrication process and down-sizing on transformation properties are discussed in detail.

For electrical resistance measurements inside a thermostat, samples are prepared on a ceramic plate as sketched in Figure 6.3. The ceramic plate will be fixed inside the thermostat by two screws. Four copper sheets are glued to the ceramic plate. Subsequently, four cables are soldered to copper sheets, which are then connected to the power source and measurement units. The sample is fixed on the ceramic plate by conductive silver glue.

Fabricated VMoO<sub>2</sub> nanobridges on a SiO<sub>2</sub>/Si substrate are connected on one side to a large common electrical contact pad and on the other side to a pad having a size of  $0.2 \mu\text{m}^2$ . These pads facilitate separate electrical connection of each nanobridge to the copper sheets by wire-bonding.

For experiments, the temperature is first increased to  $75 \text{ }^\circ\text{C}$  and, subsequently, decreased step-wise down to  $-45 \text{ }^\circ\text{C}$ , while the electrical resistance is recorded after sufficient waiting time to allow for quasi-stationary conditions. The upper limit of the sweep temperature is set to  $75 \text{ }^\circ\text{C}$  to avoid instabilities and, thus, to prevent overheating and destruction of nanostructures. The maximum acceptable temperature range is limited to  $T \pm 0.3 \text{ }^\circ\text{C}$  and the stability range of measurement points is adjusted to  $3 * 10^{-4} \text{ 1/s}$ .

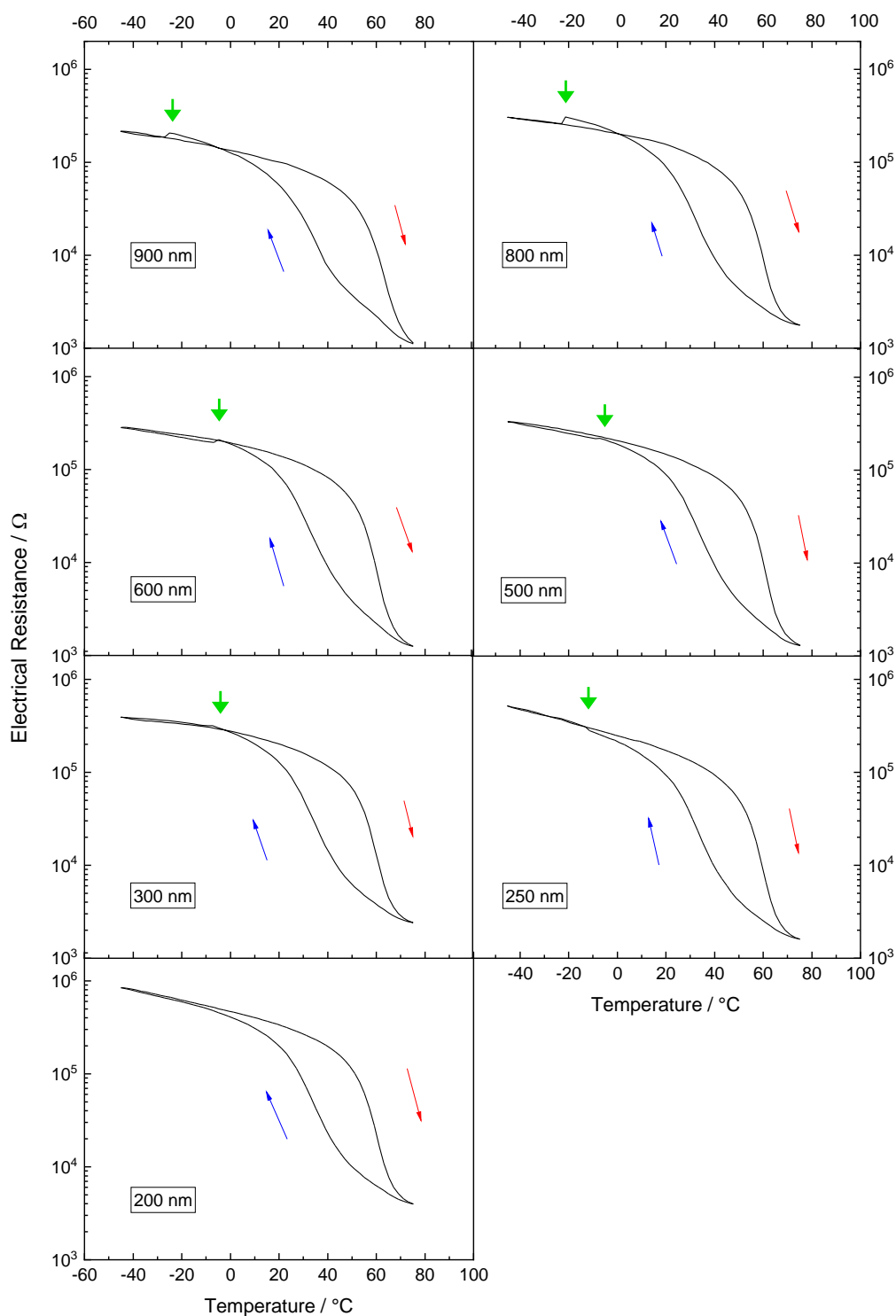


**Figure 6.4:** Electrical resistance as a function of temperature for  $\text{VMO}_2$  nanobridges with widths  $w = 200$  to  $900$  nm, having the same length of  $l = 5$   $\mu\text{m}$ . The metal to semiconductor (R-M) transformation persists for the nanostructures. The change of the electrical resistance due to the M2-M1 phase transformation is indicated by green arrows. Adapted from [133].

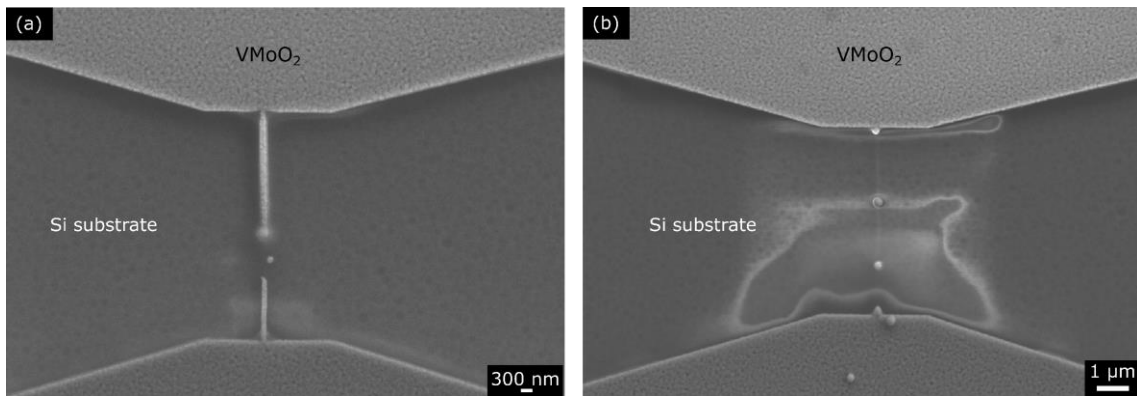


**Figure 6.5:** Scanning electron micrographs of  $\text{VMO}_2$  nanobridges with widths of  $w = 100$  nm and lengths of  $l = 5 \mu\text{m}$  after failed electrical measurements. (a) Local overheating leads to damaging of the nanobridge due to the less dense structure of film grains, and, (b) instabilities in the electrical current results in melting of the entire nanobridge.

The electrical resistance characteristics of  $\text{VMO}_2$  nanobridges with  $l = 5 \mu\text{m}$  and various widths from 900 down to 200 nm are plotted in Figure 6.4. All nanobridges are fabricated on a single chip with identical parameters. Measurements have been repeated several times in each case. The plotted characteristics depict single representative cooling-heating cycles.

The characteristic semiconductor–metal transition is observed for  $\text{VMO}_2$  nanostructures, indicating that the phase transformation persists for nanobridges with lateral widths down to  $w = 200$  nm. For sensible measurements at the nanoscale, inhomogeneities, either in the as-deposited  $\text{VMO}_2$  film or those caused after nanomachining process, could hamper measurements noticeably. Here, the electrical characteristic of the smallest nanobridges with  $w = 100$  nm could not be determined, as overheating due to large abrupt variations in the electrical current at the transition could not be avoided. Figure 6.5 shows SEM images of two damaged nanobridges with widths of 100 nm after electrical resistance measurements.

Transition temperatures of  $\text{VMO}_2$  nanobridges are determined from electrical characteristics in Figure 6.4 by Gaussian fit, as it is described for films in Figure 6.1b. Transition temperatures upon cooling  $T_{\text{tr,c}}$  and heating  $T_{\text{tr,h}}$  are plotted in Figure 6.6 and compared to those of the reference unpatterned  $\text{VMO}_2$  film that is indicated by dashed blue/red lines. Accuracies of measured data are estimated from statistical analysis of multiple measurements taking into account uncertainties due to the instrument precision [133]. Obviously, determined results on  $T_{\text{tr,c}}$  and  $T_{\text{tr,h}}$  of all nanobridges are shifted to higher temperatures compared to the reference film.

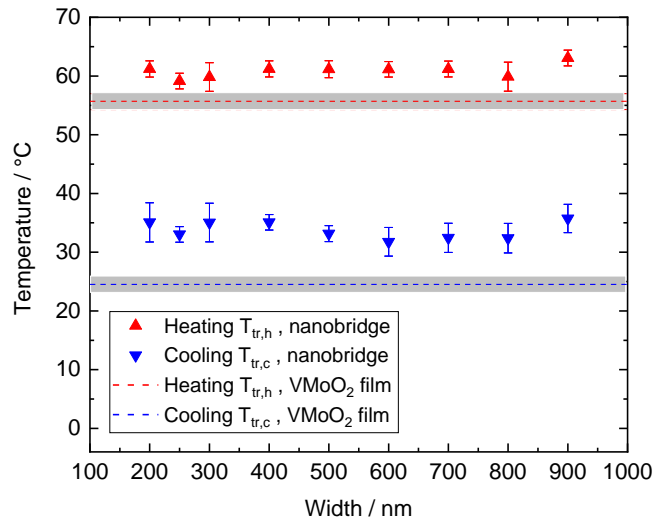


**Figure 6.6:** Transition temperatures of VMO<sub>2</sub> nanobridges of various widths upon heating  $T_{tr,h}$  (red triangles) and cooling  $T_{tr,c}$  (blue triangles). The thickness  $t$  and the length  $l$  of nanobridges are 100 nm and 5  $\mu$ m, respectively. Error bars are determined from statistical analysis of multiple measurements considering uncertainties due to instrument precision.  $T_{tr,h}$  and  $T_{tr,c}$  of the reference VMO<sub>2</sub> film are indicated by red and blue dashed lines, respectively. Corresponding measurement precision is indicated by grey shaded areas. Adapted from [133].

However, transition temperatures upon cooling  $T_{tr,c}$  show a slightly larger shift than  $T_{tr,h}$  values. This is caused by systematic measurement errors, since the limitation of the maximum set-temperature to 75 °C leads to an incomplete phase transition upon heating. Consequently, hysteresis loops decline and the inflection points  $T_{tr,c}$  shift to higher values [133]. However,  $T_{tr,h}$  values are slightly increased, indicating the presence of the built-in stress in nanobridges in contrast to the unpatterned film. For bridge structures with the restriction of fixed ends, a positive uniaxial stress is introduced along the length. Previous studies on the electrical resistance characteristics of VO<sub>2</sub>-based microbridges reveal the presence of this excess stress and its influence on phase transformation properties [68,149,150].

In Figure 6.4, beside main metal-to-insulator transitions, extra small jumps are identified in electrical resistance characteristics in the temperature range of  $-10$  to  $-30$  °C upon cooling, as indicated by green arrows. This jump is more pronounced for nanobridges with widths of 800 and 900 nm. It declines for decreasing width and cannot be resolved for the smallest nanobridge with  $w = 200$  nm. Furthermore, it tends to shift towards higher temperatures for decreasing width [133].

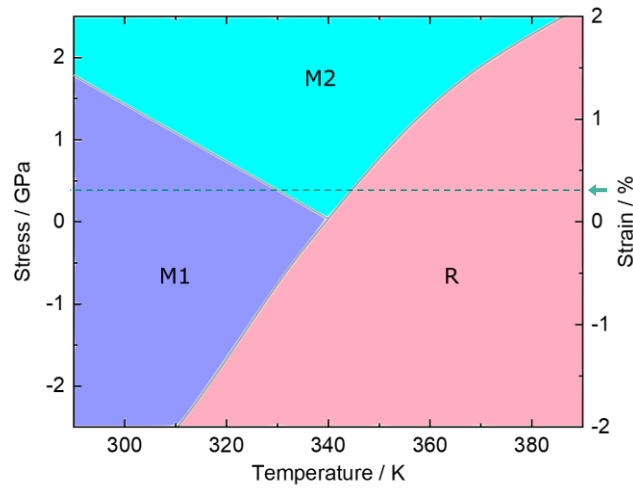


**Figure 6.7:** Schematic of the VO<sub>2</sub> temperature phase diagram, adapted from [149]. In presence of a positive stress, both M1 and M2 insulating phases may coexist, depending on the temperature of the system. For bridge structures under uniaxial stress along their length, an increase in R-M transition temperature is observed, and, by cooling from metal state, R → M2 → M1 transformation occurs. Transformation path is roughly shown by the green arrow and the dashed line.

The extra jump in electrical resistance at lower temperatures is related to the existence of two monoclinic crystal structures M1 and M2, which can occur in VO<sub>2</sub> under application of uniaxial stress [66,68,76,149,151]. Cao *et al.* [149] have studied the electrical resistance across the insulating and metal state over an extended temperature phase diagram of VO<sub>2</sub>. They observed a second jump in the electrical resistance of VO<sub>2</sub> microbridges with end-end clamps in contrast to those of flexibly bendable structures. They correlate this jump to the presence of the M2 phase with the electrical resistivity of about three times larger than of the M1 phase [149]. Figure 6.7 schematically illustrates the stress-temperature phase diagram of VO<sub>2</sub>. As it can be seen, the presence of a positive stress leads to an increase of the metal-to-insulator phase transition temperature R-M. This may result in the coexistence of M1 and M2 phases at low temperatures. By reducing of the temperature at a constant positive stress, the system undergoes the transition R → M2 → M1.

$T_{tr,h}$  values of investigated free-standing nanobridges are increased in average by around 5.4 °C. According to Clausius Clapeyron coefficient of  $\sim 1.2 \times 10^{-2}$  K/MPa [141], a stress increase of  $\sim 400$  MPa is determined, which is shown by the dashed green line in Figure 6.7.

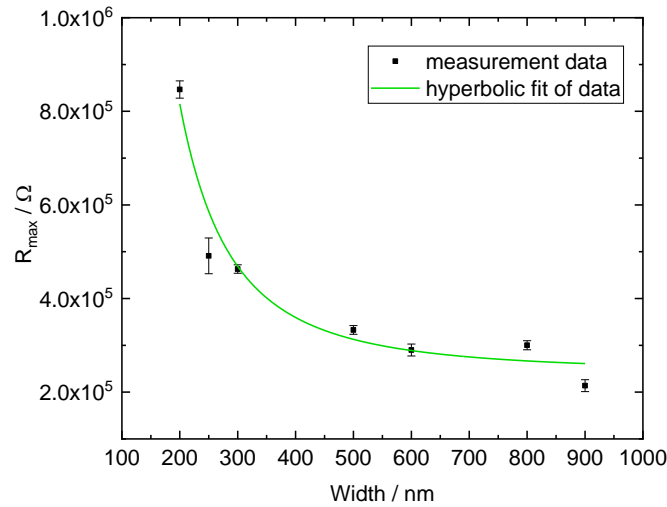


**Figure 6.8:** Electrical resistances measured at a temperature of  $T = -45$  °C for VMoO<sub>2</sub> nano-bridges with lateral widths  $w$  between 200 and 900 nm, the thickness of  $t = 100$  nm and the length of  $l = 5$   $\mu\text{m}$ . The electrical resistance of the semiconductor state shows an inverse dependence to the lateral width revealing homogenous material properties. Error bars are determined from statistical analysis of multiple measurements with considering uncertainties due to instrument precision [133].

Under existence of this stress and through cooling from the metal state first the  $R \rightarrow M2$  transformation occurs, which is then followed by  $M2 \rightarrow M1$  transformation upon further decrease of the temperature. As the M1 phase has a lower electrical resistance compared to M2 phase [149], a jump towards smaller electrical resistance values is detected (Figure 6.4). These results agree with previous reports on beam structures, where a small jump in the electrical resistance in the low-temperature semiconductor was ascribed to the M2-M1 transformation [68,149]. In this work, we extended studies to a broader range of lateral widths down to the nanoscale [133]. As stress relaxation is likely to occur for narrow nano-bridges, the phase transformation may only be stabilized for structures with sufficiently large beam widths [133]. However, as it can be seen in Figure 6.6, transition temperatures  $T_{\text{tr,c}}$  and  $T_{\text{tr,h}}$  do not indicate any significant width-dependence for nano-bridges with lateral widths down to 200 nm.

The range of electrical resistance values of nano-bridges is at least two orders of magnitude larger than that of the reference film. In the semiconducting state at the temperature of  $T = -45$  °C, the absolute value of the electrical resistance of the reference film is  $R_{\text{film}} \approx 2.2 \times 10^3 \Omega$ , while, for instance, the electrical resistance  $R_{\max}$  of nano-bridges increases from  $2.1 \times 10^5 \Omega$  for  $w = 900$  nm to  $8.5 \times 10^5 \Omega$  for  $w = 200$  nm [133]. Mean values of absolute electrical resistance in the semiconductor state as a function of nano-bridges widths are plotted in Figure 6.8.

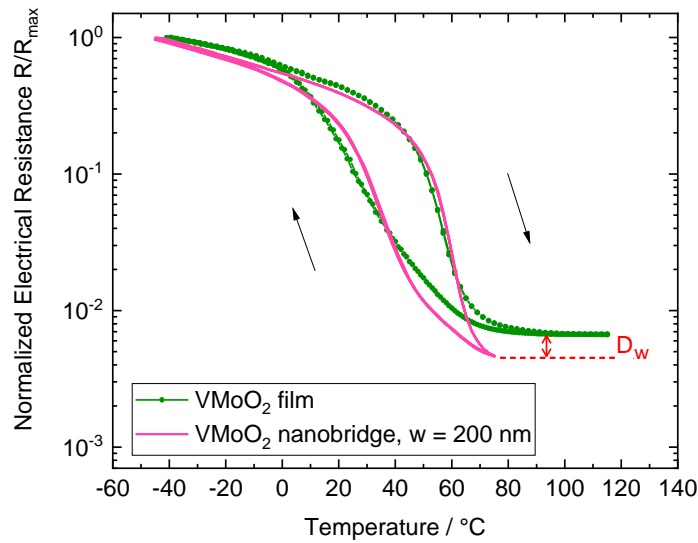


**Figure 6.9:** Electrical characteristics of a VMoO<sub>2</sub> free-standing nanobridge with a width of  $w = 200$  nm, a length of  $l = 5$   $\mu\text{m}$  and the unpatterned reference VMoO<sub>2</sub> film, having the same thickness of  $t = 100$  nm. The difference between the electrical resistance changes of the nanobridge and the film  $D_w$  is indicated by the red arrow. The change  $R/R_{\text{max}}$  is increased for the nanobridge compare to the reference film.

Previous studies on VO<sub>2</sub> thin films indicate that electrical properties are constant within each grain [152]. Thus, no drastic change in transition characteristics due to a size effect is expected for structures with lateral widths larger than the grain size. Therefore, assuming homogeneous material properties, the electrical resistance is expected to scale with the width according to  $R \propto \frac{l}{w}$ , which is in-line with measurement results in Figure 6.8 [133]. Indeed, the observed width dependence of electrical resistances does not indicate any size effect for nanobridges with lateral widths down to 200 nm, which confirms our results obtained from the analysis of width-dependent transition temperatures.

Figure 6.9 shows the temperature-dependent normalized electrical resistance  $R/R_{\text{max}}$  of a representative VMoO<sub>2</sub> nanobridge with the lateral width of  $w = 200$  nm and the length of  $l = 5$   $\mu\text{m}$ , compared to the electrical characteristic of the unpatterned reference VMoO<sub>2</sub> film. Although, the electrical characteristic of the nanobridge at lower temperatures indicates an analogous semiconducting behavior like the electrical characteristics of the reference film, there is a major difference in the magnitude of the electrical resistance change upon phase transformation. This difference is indicated by  $D_w$  in Figure 6.9. In fact, all nanobridges exhibit an enhanced electrical resistance drop compared to the reference film [133].

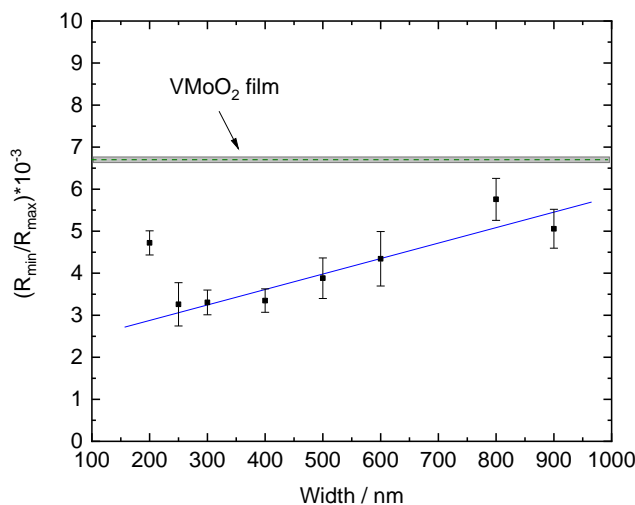


**Figure 6.10:** Width-dependence of the electrical resistance ratio  $R_{\min}/R_{\max}$  of VMO<sub>2</sub> nano-bridges.  $R_{\min}$  and  $R_{\max}$  correspond to the electrical resistance at the metal and the semiconductor state, respectively. Nanobridges have the same length of  $l = 5 \mu\text{m}$  and the same thickness of  $t = 100 \text{ nm}$ . Error bars are obtained from statistical analysis of multiple measurements considering uncertainties due to instrument precision. The ratio  $R_{\min}/R_{\max}$  for the reference VMO<sub>2</sub> film and the corresponding measurement precision are indicated by dashed line and the grey shaded area, respectively. The ratio  $R_{\min}/R_{\max}$  declines for decreasing lateral widths, as indicated by the solid blue line [133].

The enlarged change of the electrical resistance could be understood by the nature of grain boundaries and percolation effects, and is attributed to the reduced film inhomogeneities [132]. It is known that the electrical properties remain constant within each grain. Nevertheless, electrical resistance values ( $R_{\min}$  and  $R_{\max}$ ) are increased at grain boundaries, particularly in the case of disoriented thin films [132,152]. Therefore, by decreasing the lateral width, the absolute number of grain boundaries between electrical contacts reduces leading to a reduction of the electrical resistance mainly in metal state. In fact, experimental results show that the normalized electrical resistance change  $(R_{\max} - R_{\min})/(R_{\max})^{-1}$  in nanobridges increases compared to the reference film (Figure 6.9 and Figure 6.10).

For a better understanding, the electrical resistance ratios  $R_{\min}/R_{\max}$  of VMO<sub>2</sub> nano-bridges are determined and plotted in Figure 6.10. The dashed line indicates the  $R_{\min}/R_{\max}$  ratio of the reference VMO<sub>2</sub> film. As it can be seen,  $R_{\min}/R_{\max}$  values tend to decrease by reducing lateral widths  $w$ . In other words, the drop of electrical resistance over the phase transformation tends to increase by decreasing width of nanobridges. Obtained ratios for 700- and 200 nm- wide nanobridges deviate from this trend. This could be caused by issues, such as local variances in film grains and variations of geometry and structural boundaries due to fabrication tolerances [133].

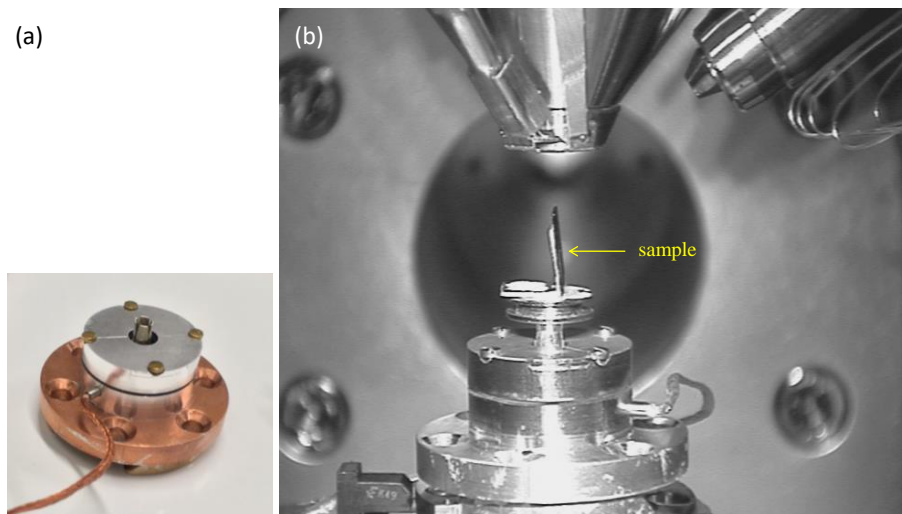


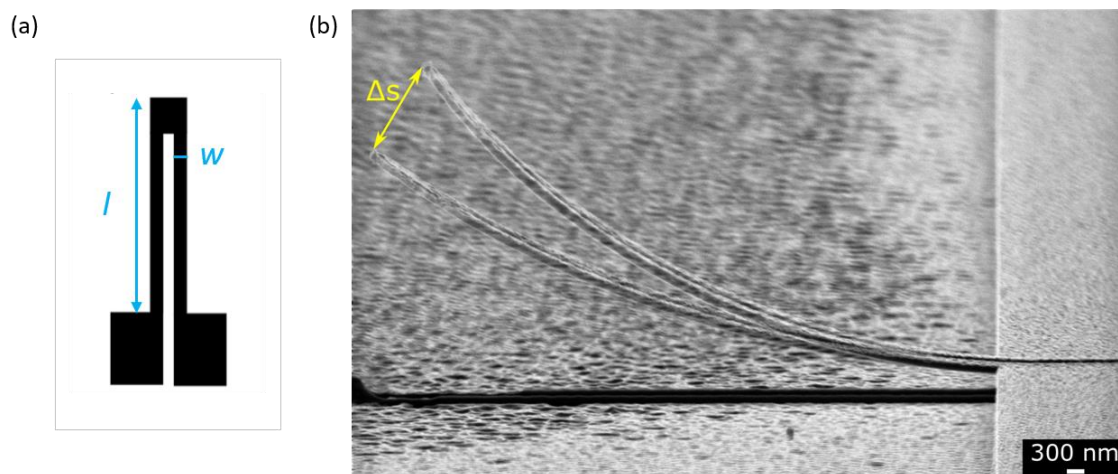
**Figure 6.11:** (a) Micro heating-cooling stage (MHCS) for the homogenous temperature control of samples inside a SEM. (b) Side-view to the SEM chamber. The sample is fixed at an angle of  $80^\circ$  to the MHCS, which is connected via an integrated vacuum/air splitter in the chamber flange to a temperature control unit.

## 6.2 In-Situ Nanoactuation

Actuation characteristics of bimorph Cr/VMoO<sub>2</sub> double-beams are studied. Nano double-beams are fabricated as described in section 5.3. For investigation of mechanical movements at the nanoscale, a specific measurement setup inside a SEM is required. Thermal actuation is either realized by altering the temperature of the sample homogeneously, or by Joule-heating of individual structures.

### 6.2.1 Nanoactuation by Homogeneous Temperature Control

As part of this work, the first prototype of a micro heating-cooling stage (MHCS) for homogenous temperature control of samples inside a SEM is developed in collaboration with Kleindiek Nanotechnik GmbH (see Figure 6.11). The MHCS is equipped with multiple Peltier elements, which are integrated in one unit with a temperature control system to maintain set temperatures stable for several minutes. This allows for measurements under quasi-stationary conditions. As it can be seen in Figure 6.11, the MHCS can be used as a SEM stage. The sample is attached by conductive silver glue to a sample holder at an angle of  $80^\circ$ , which is fixed to the stage in direct connection to the heat source/sink.



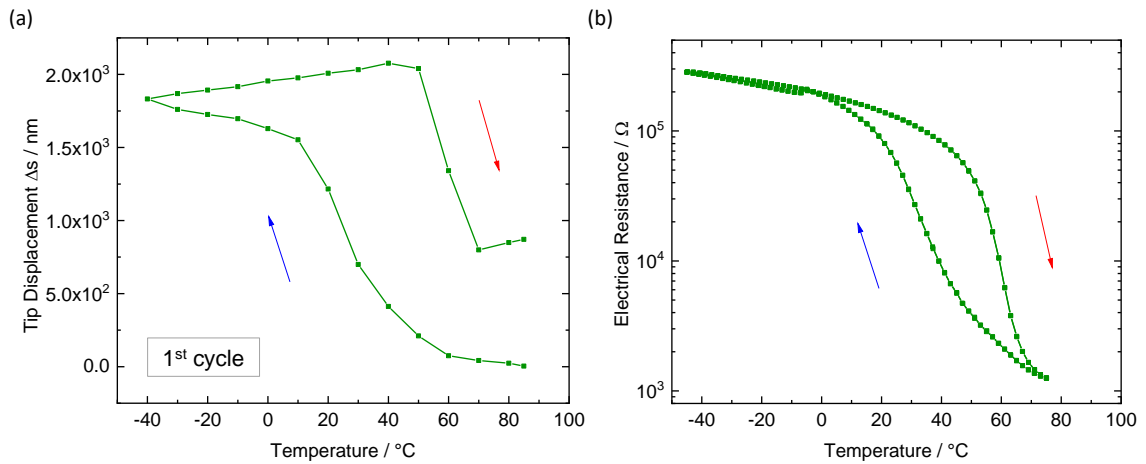
**Figure 6.12:** (a) Top-view schematic of a double-beam nanoactuator with the width of  $w$  and the length of  $l$ . (b) Overlay of two SEM images of a Cr/VMoO<sub>2</sub> double-beam actuator with  $l = 12 \mu\text{m}$  and  $w = 600 \text{ nm}$  at temperatures of  $-40 \text{ }^\circ\text{C}$  and  $85 \text{ }^\circ\text{C}$ . Thickness of Cr and VMoO<sub>2</sub> films are 37 and 100 nm, respectively. An upward deflection  $\Delta s$  is observed upon cooling under quasi-stationary conditions.

Figure 6.12a depicts a top-view schematic of a double-beam nanoactuator with beam length  $l$  and width  $w$ . The fabricated double-beam is a bimorph consisting of a Cr layer on top of the VMoO<sub>2</sub> film having thicknesses of 37 and 100 nm, respectively. For measurements, the nanoactuator is cooled down step-wise from a high temperature, larger than the phase transformation temperature  $T_{tr}$ , to below  $T_{tr}$ , and reheated to the starting temperature to complete the transformation hysteresis loop. Sufficient waiting times at each set temperatures guarantees the quasi-stationary measurement conditions. During heating and cooling of the location of the nanoactuator moves relative to the SEM window. This drift is caused by thermal expansion and compression of the setup and must be corrected after reaching a steady state for each set temperature.

At each set temperature, a SEM image is taken from the nanoactuator. In order to determine the out-of-plane deflection, a motion sequence of successive SEM images is established. The sequence is imported and analyzed by tracking software.

Figure 6.12b shows an overlay of two SEM micrographs of a Cr/VMoO<sub>2</sub> double-beam nanoactuator with width of  $w = 600 \text{ nm}$  and length of  $l = 12 \mu\text{m}$ . By cooling down from  $85 \text{ }^\circ\text{C}$  to  $-40 \text{ }^\circ\text{C}$ , the double-beam bends upwards.

Principally, the temperature-dependent deflection characteristics of SMM-based bimorph beam actuators is a sum of three mechanisms. First mechanism is a bimorph effect due to the different thermal expansion coefficients of materials.



**Figure 6.13:** (a) Out-of-plane deflection of the tip of a Cr/VMoO<sub>2</sub> double-beam actuator with the length of  $l = 12 \mu\text{m}$  and the width of  $w = 600 \text{ nm}$ . Thicknesses of Cr and VMoO<sub>2</sub> films are 37 and 100 nm, respectively. The nonlinearity in the tip displacement at the temperature range of  $0^\circ \text{C} < T < 60^\circ \text{C}$  is caused by the phase transformation of VMoO<sub>2</sub>, which is in agreement with the electrical resistance characteristic of a VMoO<sub>2</sub> nanobridge with the same width of 600 nm, as depicted in (b).

Another effect is a result of phase transformation in the shape memory material, since austenite and martensite exhibit different material properties including different thermal expansion coefficients. The third mechanism includes the effect of self-accommodation in martensite state [135,153]. It has been shown previously that the bending characteristic of SMM-based nanobimorphs reveal a competition between these mechanisms and depends strongly on the thickness ratio of layers [153]. Apparently, the deflection characteristics of the Cr/VMoO<sub>2</sub> double-beam nanoactuator with the thickness ratio of  $t_{\text{Cr}}/t_{\text{VMoO}_2} = 0.37$  is mainly ascribed to the change of the crystal lattice constant upon phase transformation, as it has been previously reported for bending characteristics of Cr on VO<sub>2</sub>-based beams and cantilevers as well [44,138,154,155]. As described in section 2.2.1, VO<sub>2</sub> has a larger lattice constant in the martensite than in the austenite. Thus, by cooling down, the double-beam bends away from the VMoO<sub>2</sub> layer and, consequently, it bends upwards. However, in order to have a better understanding of actuation characteristics, different material properties need to be determined including lattice constants and thermal expansion coefficients of the austenite (A) and martensite (M1, M2) phases of the VMoO<sub>2</sub>.

Figure 6.13a shows the out-of-plane tip displacement  $\Delta s$  of the Cr/VMoO<sub>2</sub> double-beam for the first temperature cycle. Clearly, the tip displacement indicates a non-linear characteristic in the temperature region between  $0^\circ \text{C}$  and  $60^\circ \text{C}$ , which is in the range of phase transformation temperature as determined before by the electrical measurement resistance for a VMoO<sub>2</sub> nanobridge with the same width of 600 nm (see Figure 6.13b).

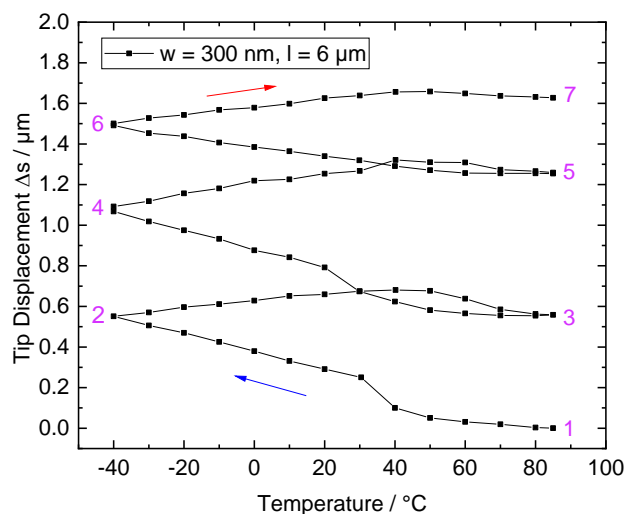


**Figure 6.14:** Out-of-plane tip displacement of a Cr/VMoO<sub>2</sub> double-beam actuator for the first three successive cooling-heating cycles. The relative stroke decreases from 9 % for the first cooling trace 1→2 to around 4 % for the trace 5→6, which corresponds to a decrease of about 58 %. The third cycle demonstrates an almost linear behavior. Through observations by focused electron beam of the SEM, the VMoO<sub>2</sub> forfeits its phase transformation properties.

Due to the phase transformation of VMoO<sub>2</sub>, a large displacement of around 1.7 μm is achieved upon cooling, which corresponds to a large relative actuation stroke of  $\Delta s/l = 1.7 \mu\text{m}/12 \mu\text{m} * 100 \approx 14 \%$ . Nevertheless, the transformation hysteresis is broadened. This could be related to the induced strain across the Cr and VMoO<sub>2</sub> interface. This strain stabilizes a multiple M-R domain structure along the VO<sub>2</sub> layer, which leads to a gradual phase transformation [35,66,138,156]. By heating up back to 85 °C, the double-beam bends downwards. However, it does not return to the initial tip position.

For a better understanding of the actuation characteristic, the tip displacement of a double-beam with  $w = 300 \text{ nm}$  and  $l = 6 \mu\text{m}$  is investigated for three successive cycles in a temperature range of  $-40$  to  $85 \text{ }^\circ\text{C}$ . The tip displacement  $\Delta s$  is shown in Figure 6.14. As before, the actuator demonstrates a non-linear characteristic for the first cooling trace 1→2, with an out-of-plane tip displacement of around  $0.5 \mu\text{m}$ , which corresponds to a relative actuation stroke of around 9 %. Upon heating 2→3, the double-beam does not return to the initial position, and, the second cycle begins at the tip position of  $\Delta s \approx 0.6 \mu\text{m}$ . Upon cooling 3→4, the non-linear tip displacement is again observed. However, the relative actuation stroke is reduced to around 7.6 %. This is also the case for the third cycle, where the stroke is further decreased to around 4 % for the trace 5→6, and, moreover, it exhibits an almost linear actuation characteristic. In total, the relative actuation stroke of the nanoactuation has declined by about 58 %.

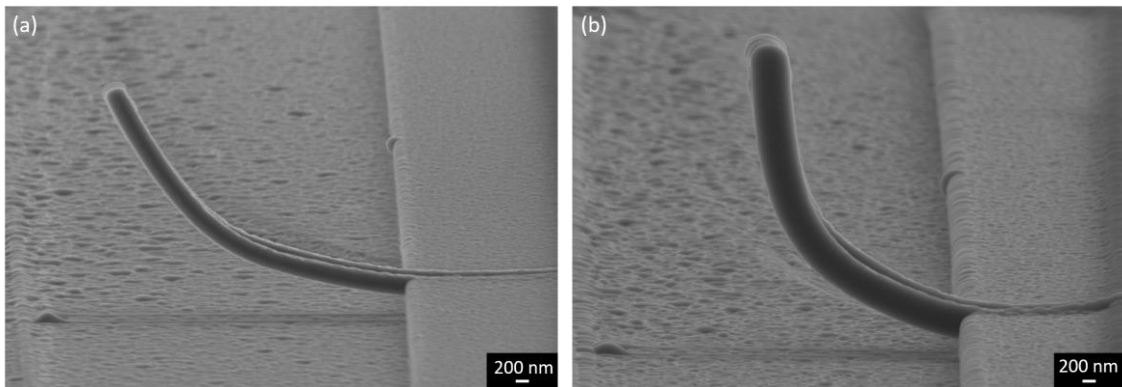


**Figure 6.15:** SEM micrographs of a Cr/VMoO<sub>2</sub> double-beam actuator with  $w = 300$  nm and  $l = 6$   $\mu\text{m}$  at the temperature of  $85$   $^{\circ}\text{C}$ , (a) before starting the measurement, and (b) after three cooling-heating cycles. The focus window of the SEM and the magnification is kept fixed over the entire measurement of exceeding 6 hours. The morphology of the film surface and the double-beam is changed. A thickening effect is observed.

The actuation shows a systematic drift over successive cycles, and, it loses the non-linear characteristic induced by the VMoO<sub>2</sub> phase transformation. As it can be seen in Figure 6.15, the morphology of the structure also drastically changes after finishing the three measurement cycles over a time period of exceeding 6 hours. The form of the actuator is changed permanently, and it does not go back to original form even after several hours or days. Apparently, irreversible changes of the structure of the VMoO<sub>2</sub> material caused by exposure by electrons degrade the actuation.

In order to elucidate any nano scale effects, unpatterned films are investigated under similar conditions. First, the surface of the VMoO<sub>2</sub> film, without Cr coating, is observed in a SEM by a rectangular reduced scanning window at the temperature of  $25$   $^{\circ}\text{C}$  for 10 min (Figure 6.16a). The area of the reduced window appears to be brighter after observation, due to surface charging by electrons. However, the film morphology does not show any significant change. Figure 6.16b depicts the surface of the VMoO<sub>2</sub> film after observations via the reduced scanning window at  $-35$   $^{\circ}\text{C}$  for 10 min. In contrast to Figure 6.16a, film grains are locally inflated around the observation window. Furthermore, the effect is not related to any Cr layer. The alteration of grains is irreversible as it was observed before for the double-beam nanoactuators. However, there occurs no changes in the film surface elsewhere, away from SEM observation area.

This is also the case for structures on the sample in Figure 6.15, i.e. other double-beams, which were not continuously observed by SEM during temperature-dependent measurements, have maintained their original shape.

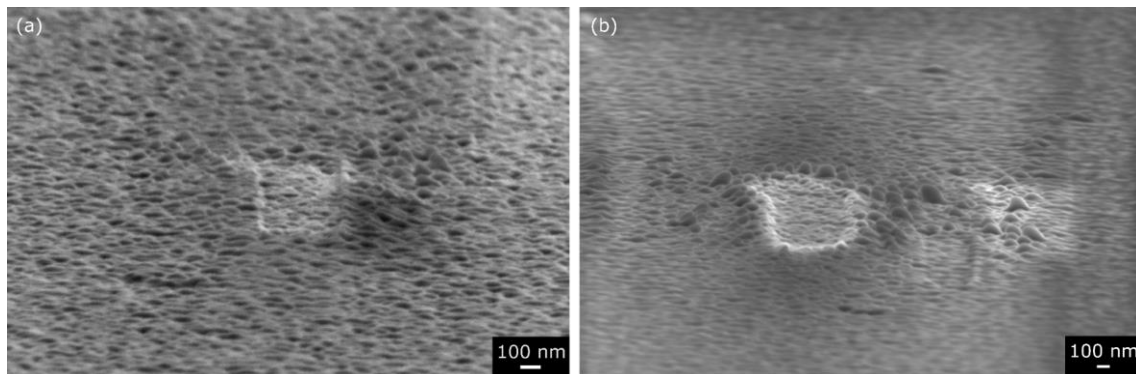


**Figure 6.16:** SEM micrographs of  $\text{VMO}_2$  films after temperature-dependent measurements. The surface of the film after 10 min of exposure to the SEM e-beam through a reduced scanning window at 25 °C. (a) and at  $-35$  °C (b) indicating local change of crystal structure. Reduced scanning windows can be recognized by the brighter rectangular areas in the middle of graphs.

In addition, samples after electrical resistance measurements inside the thermostat do not indicate any shape or morphology alterations as well (section 6.1.1). For those measurements, the temperature is swept between  $-40$  °C and 120 °C. These results indicate that changes in the film are associated with electron exposure at low temperatures. Similar investigations on  $\text{VO}_2$  films reveal the same effect. The change of structure also occurs for  $\text{VO}_2$  films and, thus, it does not depend on the Mo content.

In conclusion, continuous observation of  $\text{VO}_2$ -based films and structures by a SEM at low temperatures leads to irreversible changes of crystal structure. This leads to the degradation of phase transformation properties and, thus, drastically affects the actuation performance of bimorph double-beam actuators. Therefore, temperature-dependent in-situ inside SEM experiments need to be limited to a single cooling track.

Before measurements, the sample is heated up and cooled down in a cyclic manner for several times. Figure 6.17 shows the relative actuation stroke  $\Delta s/l$  of double-beams with an identical length to width ratio of  $l/w = 20$  upon cooling from 85 °C to  $-40$  °C. All three bimorph actuators show non-linear deflection characteristics as a result of the structural phase transformation of  $\text{VMO}_2$ . However, the actuation stroke declines and the slope of the deflection change  $\Delta s/l$  upon the transformation decreases by reducing size. This indicates the increasing influence of the inhomogeneities and defects after nanofabrication.

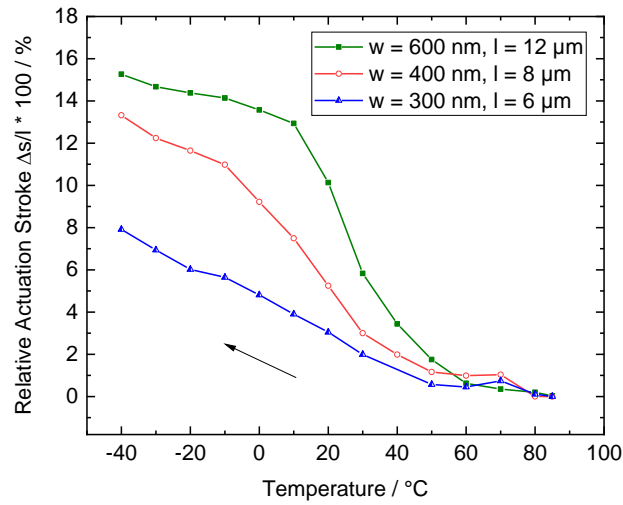


**Figure 6.17:** Relative actuation stroke  $\Delta s/l$  of Cr/VMoO<sub>2</sub> double-beam nanoactuators, while cooling from 85 °C down to -40 °C. Tip displacement  $\Delta s$  is extracted from SEM images by using tracking software. All double-beams have the same layers thickness, i.e.  $t_{\text{Cr}}/t_{\text{VMoO}_2} = 37 \text{ nm}/100 \text{ nm}$ . A large relative actuation stroke of around 15 % is achieved for the double-beam with the length of  $l = 12 \mu\text{m}$  and the width of  $w = 600 \text{ nm}$ . The relative stroke declines by decreasing the size of actuators, due to inhomogeneities and defects in small structures introduced by nanofabrication.

## 6.2.2 Nanoactuation by Joule Heating

The out-of-plane deflection of Cr/VMoO<sub>2</sub> double-beams is also investigated in-situ by direct Joule-heating inside a SEM. A four-point-probe setup is established using nanomanipulators to electrically interconnect individual nanoactuators, as illustrated in Figure 6.18. Three electrical connections are provided by nanomanipulators and the fourth one is a wire-bonded Al wire. An electrical current is applied by an outer positioned nanomanipulator and the Al wire, while the voltage is measured by inner nanomanipulators, which are precisely positioned at both sides of the structure. These are then connected to a source measure unit, which is controlled by a LabVIEW script and enables the real-time determination of the electrical power, current, voltage, resistance and time in milliseconds. Monitoring of the electrical resistance allows for the real-time noticing of the phase transformation progress. As current passes through the double-beam, a temperature gradient occurs along the structure with the maximum at the tip [157]. The out-of-plane deflection of the structure is recorded during measurement. Subsequently, the SEM video is used to determine the tip displacement by tracking software. Figure 6.19 shows the out-of-plane deflection of a double-beam with  $w = 500 \text{ nm}$  and  $l = 10 \mu\text{m}$  after applying a constant electrical power of 0.02 mW. From real-time electrical resistance measurement, it is inferred that the rutile state is fully reached. Through the martensite to austenite phase transformation  $M \rightarrow R$ , the double-beam bends downwards, since the lattice constant in rutile state is smaller than that of in monoclinic state.

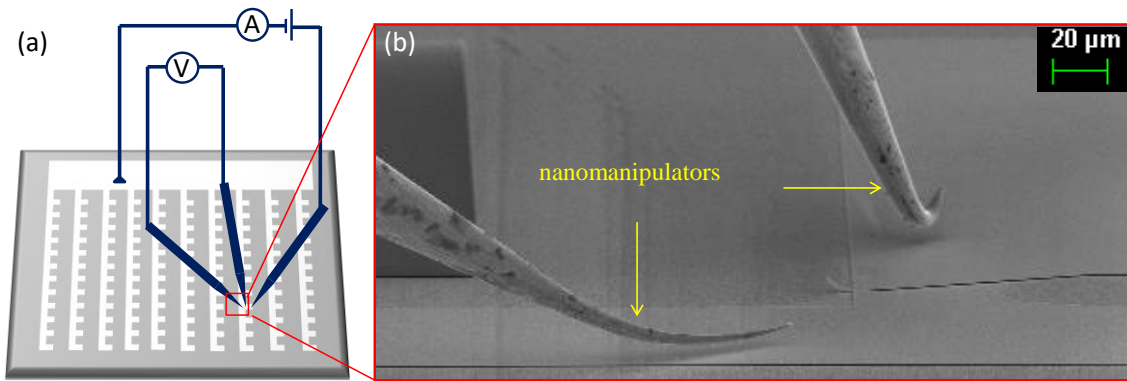


**Figure 6.18:** (a) Schematic of the four-point-probe setup for Joule heating measurements inside a SEM. (b) Scanning electron micrograph of a Cr/VMo<sub>2</sub> double-beam and two nanomanipulators positioned at each side of the structure to measure the voltage.

This result agrees with previous deflection observations by homogenous heating-cooling of samples in subsection 6.2.1. This downward deflection corresponds to the relative actuation stroke of  $\Delta s/l = 4.8\%$ . The actuation stroke is in this case smaller compared to results of homogenous temperature change. This can be explained by the temperature gradient along the double-beam caused by Joule heating. Hence, the phase transformation is partially reached at different section along the structure [135]. At higher temperatures, an upward deflection is observed upon further heating, since the thermal expansion coefficient of VMo<sub>2</sub> in rutile state is larger compared to Cr [33,138,155,158].

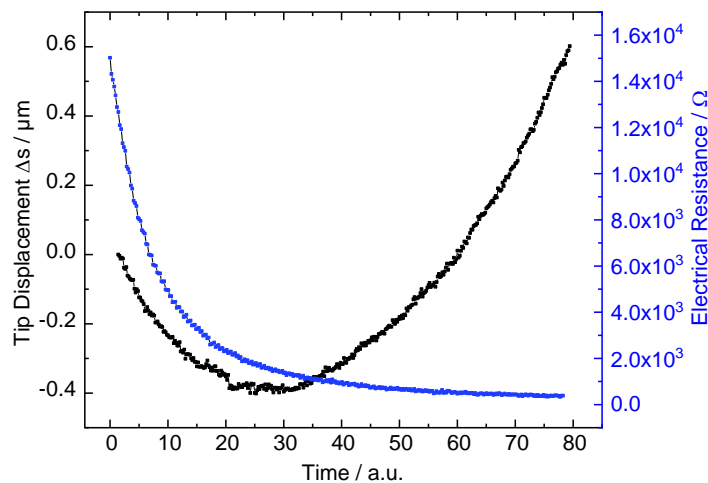


**Figure 6.19:** Tip displacement and electrical resistance of a Cr/VMo<sub>2</sub> double-beam with  $w = 500 \text{ nm}$  and  $l = 10 \mu\text{m}$  determined from Joule heating by applying an initial electrical power of  $0.02 \text{ mW}$ . The electrical resistance shows a large decrease indicating  $M \rightarrow R$  phase transformation. Hence, the double-beam bends downwards with a relative actuation stroke of  $\Delta s/l = 4.8\%$ . As the thermal expansion coefficient of VMo<sub>2</sub> in rutile state is larger compare to that of Cr, an upward deflection is observed upon further heating.

## 6.3 Summary

In this section, phase transformation properties of VO<sub>2</sub>-based thin films, nanobridges and double-beam nanoactuators are studied. Temperature-dependent electrical characteristics of films indicate that the phase transformation properties such as hysteresis width and transition temperature can be tuned by doping of VO<sub>2</sub> with a third material. Temperature-dependent electrical characteristics of free-standing VMoO<sub>2</sub> nanobridges show that the phase transformation persists after nanofabrication even for the smallest lateral width of 200 nm. Transition temperatures of nanobridges do not reveal any significant width dependence. In principle, electrical resistance values of nanobridges in the semiconducting state are inversely proportional to the width indicating the scaling behavior of a homogeneous material. A major effect is the resistance change due to the phase transformation which is enhanced for nanobridges compared to the unpatterned film indicating reduced carrier scattering as the absolute number of grain boundaries decreases. Actuation characteristics of Cr/VMoO<sub>2</sub> nano double-beams are investigated by a SEM and show upward bending upon cooling. The out-of-plane tip displacements are non-linear reflecting phase transformation in VMoO<sub>2</sub> even for the smallest nanoactuator with a beam width of 300 nm. Amplitude and slope of deflection are reduced for smaller double-beams. However, a relatively large actuation stroke of up to 15 % is achieved for the nanoactuator with the length of 12 μm and the width of 600 nm. The continuous observation of VO<sub>2</sub>-based films and structures by SEM at temperatures below 0 C leads to an irreversible anomalous change of crystallinity and, thus, a strong degradation of actuation stroke. Hence, temperature-dependent experiments by SEM need to be limited to a single cooling run. For further investigations of nanoactuation, it is essential to develop new techniques, which enable local sensing of the beam deflection, for instance, by optical methods instead of using SEM.



# 7 Development of Optical Devices Based on Vanadium Dioxide

In this chapter, design and fabrication of photonic devices based on VO<sub>2</sub> thin films are introduced. The focus of interest is to realize novel optical switches and fuses with small footprints, which serve as built-in components in photonic applications, such as photodetectors. The principle of operation is based on the insulator-metal transition in VO<sub>2</sub>. Thereby, VO<sub>2</sub> optical transmittance in IR range varies from transparent to opaque, corresponding to two different switching states *on* and *off*, respectively.

In the following, first, optical properties of VO<sub>2</sub> thin films are presented. The concept of the device design and the operation principle are introduced in section 7.2. The proof-of-concept is studied by finite element method (FEM) simulations, which will be discussed in section 7.3. The nanofabrication method based on sputter deposition of VO<sub>2</sub> films on pre-structured Si-based platforms is described in section 7.4. Experimental results on optical transmission measurements of fabricated devices are discussed in section 7.5.

## 7.1 Optical Properties of VO<sub>2</sub> Films Determined by Ellipsometry

Optical characteristics of VO<sub>2</sub> films are determined by ellipsometry. The measurement model and the analysis method are described in section 4.5. For temperature-dependent measurements, the setup includes a large copper plate as the heat source, which is integrated at the measurement spot of the ellipsometer. In addition, the surface electrical resistances of films are continuously observed during measurements to detect the insulator-metal transition.

The complex refractive index of a VO<sub>2</sub> film with a thickness of 180 nm is determined in the wavelength range of 310 to 2500 nm. Figure 7.1a shows real refractive indices of the VO<sub>2</sub> film in insulator state at room temperature and in metal state at  $T = 150 \pm 5$  °C. The refractive index in insulator state does not indicate a considerable change in the spectral range and increases slightly from 2.77 at the wavelength of 310 nm to 3.45 at the wavelength of 2500 nm. In contrast, the refractive index in metal state exhibits large changes. First, it decreases drastically from 2.77 at the wavelength of 310 nm to a minimum value of 1.38 at the wavelength of 966 nm, then it increases to the value of 4.3 at the wavelength of 2500 nm.

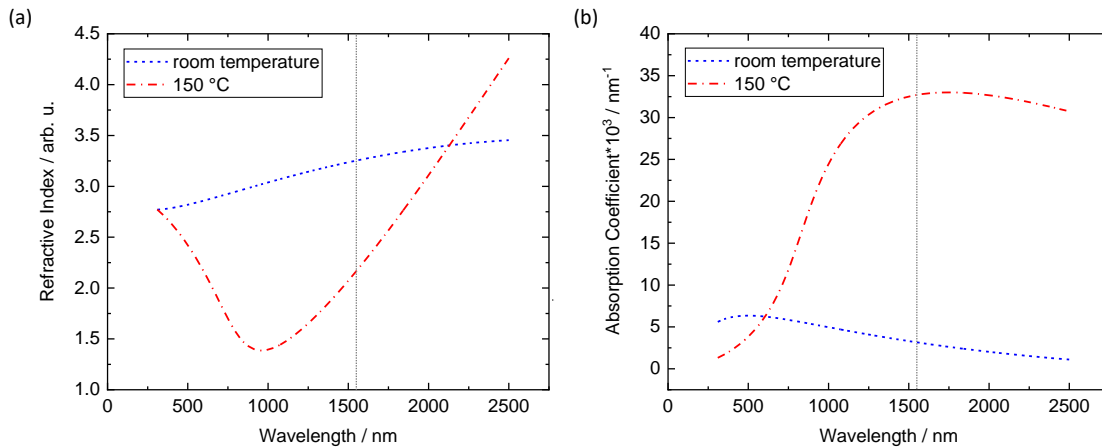


**Figure 7.1:** Optical characteristics of a 180 nm-thick VO<sub>2</sub> film sputtered on a SiO<sub>2</sub>/Si substrate determined by ellipsometry at UV to NIR spectral range for the insulator state at room temperature and the metal state at  $T = 150 \pm 5$  °C. (a) At the wavelength of 1550 nm (indicated by gray dashed line) the refractive index changes from 3.25 in insulator state to 2.2 in metal state. (b) The absorption coefficient at the wavelength of 1550 nm shows a large change from  $32 \cdot 10^3$  cm<sup>-1</sup> in insulator state to  $323 \cdot 10^3$  cm<sup>-1</sup> in metal state.

The maximum difference of refractive indices between insulator and metal states of the VO<sub>2</sub> film is 1.65 at the wavelength of 1007 nm. Absorption coefficients  $\alpha$  are determined from measured extinction coefficients  $\kappa$  by  $\alpha = 4\pi \kappa / \lambda$  [101] and are plotted in Figure 7.1b. In metal state the film shows a maximum absorption coefficient of  $\sim 329 \cdot 10^3$  cm<sup>-1</sup> at the wavelength of 1748 nm. The maximum difference between absorption coefficients between metal and insulator state of about  $330 \cdot 10^3$  cm<sup>-1</sup> occurs at the wavelength of 1760 nm. The real and imaginary part of the refractive index, i.e.  $n$  and  $\kappa$  in equation 3.5, are measured by ellipsometry. At the wavelength of 1550 nm, complex refractive indices are given by  $\tilde{n}_{RT} = 3.25 + 0.39i$  for the insulator state and  $\tilde{n}_{HOT} = 2.05 + 4.28i$  for the metal VO<sub>2</sub>, which are comparable to reported values in literature [159,160]. This large alteration of the optical transmittance between insulator and metal states of the VO<sub>2</sub> film, particularly, the change of around one order of magnitude in extinction coefficients  $\kappa$ , is of a great significance for optical switching, as it is explained in the following section.

## 7.2 Concept of Device Design<sup>1 2</sup>

The simplest VO<sub>2</sub> photonic switch can be realized by deposition of a VO<sub>2</sub> film on a section of a Si waveguide, as depicted in Figure 7.2.

<sup>1</sup> Presented results are partially based on the master thesis of Ms. A. Ewy, which was supervised in the context of this thesis.

<sup>2</sup> Permission provided by: Annika Ewy agrees to the publication of materials from the master thesis, entitled "Plasmonic nano-devices based on vanadium dioxide (VO<sub>2</sub>) thin films".

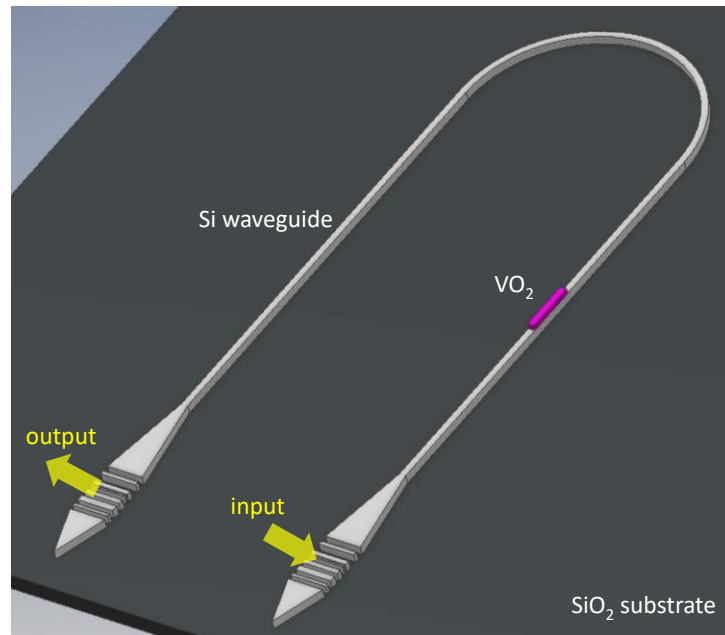


**Figure 7.2:** Schematic of design concept of a photonic switching device using the metal-insulator transition of a VO<sub>2</sub> film covering a section of a Si waveguide. The input optical power either propagates through the waveguide to the output for the VO<sub>2</sub> film in insulator state or absorbed by the VO<sub>2</sub> film in metal state.

As explained in the previous section, the VO<sub>2</sub> film in insulator state shows a relatively low absorption at  $\lambda = 1550$  nm, which allows for light propagation (*on* state), whereas in metal state, it shows a large absorption coefficient that prevents the propagation of light (*off* state). Additionally, the traveling light through the waveguide covered by a VO<sub>2</sub> film in metal state can cause the formation of surface plasmon polaritons (SPP) [28,29,161]. SPPs are electromagnetic excitations existing at metal-dielectric interfaces. They are evanescently confined at the interface with the electric field perpendicular to the direction of the propagating light through the waveguide. Thus, SPPs exhibit principally TM eigenwaves that propagate along the interface with an exponentially decaying intensity inside adjoining materials. Accordingly, light is coupled to the metal VO<sub>2</sub> film and, consequently, is absorbed by the material [162,163].

In insulator state, however, VO<sub>2</sub> is not perfectly transparent at the wavelength of 1550 nm. Thus, a slight part of the input power will be absorbed, which defines the insertion loss of the system in *on* state. Nevertheless, the absorption of the light by the VO<sub>2</sub> in insulator state can be exploited to develop novel photonic fuses using the optically induced insulator-metal transition. As the input power increases, more photons will be absorbed in VO<sub>2</sub> and the energy of photons is converted to thermal energy. Accordingly, the temperature increases causing the transition from insulator to metal state [44,164].

To obtain the desired switching and modulating functionality based on the insulator-metal transition, physical properties of the VO<sub>2</sub>-based structure require to be adjusted (refer to sections 2.2 and 6.1.1). For instance, through doping of the VO<sub>2</sub> film with other materials, the optical absorption or reflectance of the VO<sub>2</sub> film can be optimized according to the operation wavelength of the device. In addition, the required optical energy to trigger the insulator-metal transition can be reduced by decreasing the transition temperature.

The switching characteristic can be improved as well by adjusting geometry parameters, such as the length and the thickness of the VO<sub>2</sub> structure. Therefore, simulations are used for the proof of concept, also, to investigate the optical performance of different designs, before starting fabrication.

### 7.3 Proof-of-Concept by FEM Simulation<sup>3 4</sup>

The concept of photonic switching based on the insulator-metal transition of VO<sub>2</sub> films is investigated through FEM simulation by using the wave optics module of COMSOL Multiphysics® Modeling Software in three-dimensional (3D) space.

To reduce the computational time, the device model includes the VO<sub>2</sub> structure, the Si waveguide and the SiO<sub>2</sub> substrate, whereas grating couplers and bending of waveguides are omitted. The model setup is depicted in Figure 7.3.

In the following, optical performance of two device designs are discussed. The type 1 device has the simplest design and includes a single VO<sub>2</sub> box on top of the waveguide (Figure 7.3b1), whereas in type 2 device, the VO<sub>2</sub> covers top and sidewalls of the waveguide (Figure 7.3b2). Material and geometry parameters used in the simulations are listed in Table 7.1.

**Table 7.1:** Geometry and optical parameters of materials for modeling of optical switches [165]. The wavelength of the input light is 1550 nm.

Parameter	VO <sub>2</sub>	Si	SiO <sub>2</sub>
Length / $\mu\text{m}$	0.05 – 4.0	7	7
Width / $\mu\text{m}$	0.5	0.5	4
thickness	10 – 100 / nm	220 / nm	1 / $\mu\text{m}$
real refractive index n	3.25 ( $T < T_{\text{tr}}$ ), 2.05 ( $T > T_{\text{tr}}$ )	3.48	1.45
imaginary refractive index k	0.39 ( $T < T_{\text{tr}}$ ), 4.28 ( $T > T_{\text{tr}}$ )	0	0

<sup>3</sup> Presented results are partially based on the master thesis of Ms. A. Ewy, which was supervised in the context of this thesis.

<sup>4</sup> Permission provided by: Annika Ewy agrees to the publication of materials from the master thesis, entitled "Plasmonic nano-devices based on vanadium dioxide (VO<sub>2</sub>) thin films".

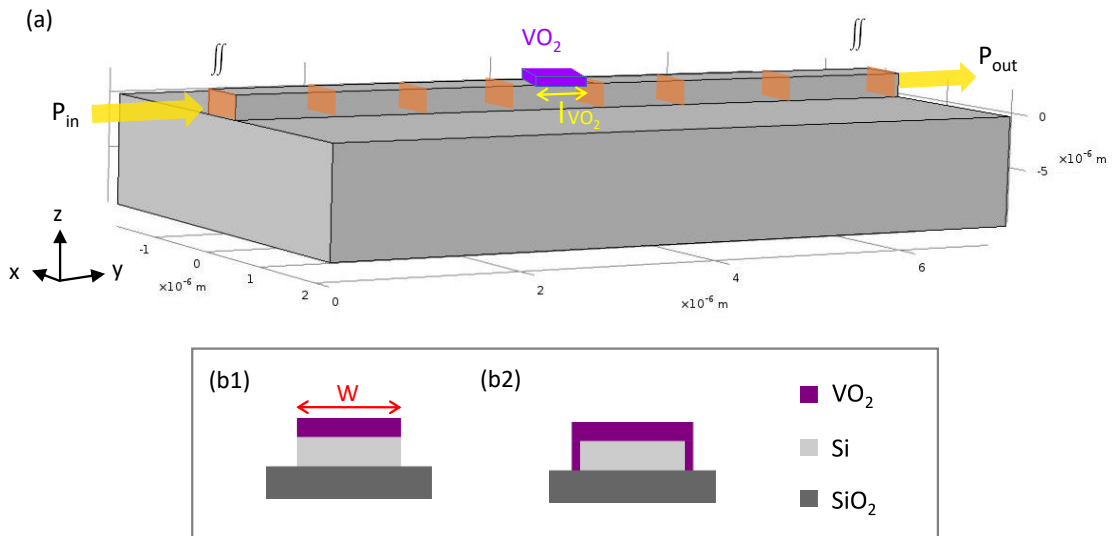


**Figure 7.3:** (a) Three-dimensional (3D) FEM simulation model of a Si waveguide switch including a VO<sub>2</sub> film covering a Si waveguide on a SiO<sub>2</sub> substrate. The representative power integral surfaces along the waveguide are indicated by orange rectangles. (b1) and (b2) depict schematic cross-sections of type 1 and type 2 devices, respectively. The length and width of the VO<sub>2</sub> structure are indicated by  $l_{\text{VO}_2}$  and  $w$ , respectively.

Figure 7.4 shows a simulation of light propagation through a device of type 1 with a VO<sub>2</sub> structure having a length of 1  $\mu\text{m}$  and a thickness of 50 nm. Figure 7.4a shows the normalized electric field for the device in insulator state (*on* state). As it can be seen, light modes beneath the VO<sub>2</sub> structure are not only confined within the Si waveguide, but also travel into the VO<sub>2</sub> and, hence, their propagation is slightly perturbed. Yet, around 90 % of the input light is transmitted to the output.

In *off* state of the device shown in Figure 7.4b, light is clearly absorbed in metal state, hence, only  $\sim 57\%$  of the input is transmitted to the output.

In order to determine the power flow along the waveguide, surface integrals are calculated at cross-sections perpendicular to the light propagation direction, as schematically shown in Figure 7.3a. The magnitude of the power flow vector  $\mathbf{P}$  (refer to section 3.1) is defined as the power flow per unit area and is calculated by

$$\iint |\mathbf{P}| = \iint \sqrt{P_x^2 + P_y^2 + P_z^2} \quad (7.1)$$

The power flow along a type 1 device with the VO<sub>2</sub> structure having a length of 1  $\mu\text{m}$  and a thickness of 30 nm is plotted in Figure 7.5b. Although, the inserted power decreases along the VO<sub>2</sub> structure for both insulator and metal states, the total transmitted power for the device in metal state is further reduced by  $\sim 40\%$  in comparison to the device in insulator state indicating optical switching.

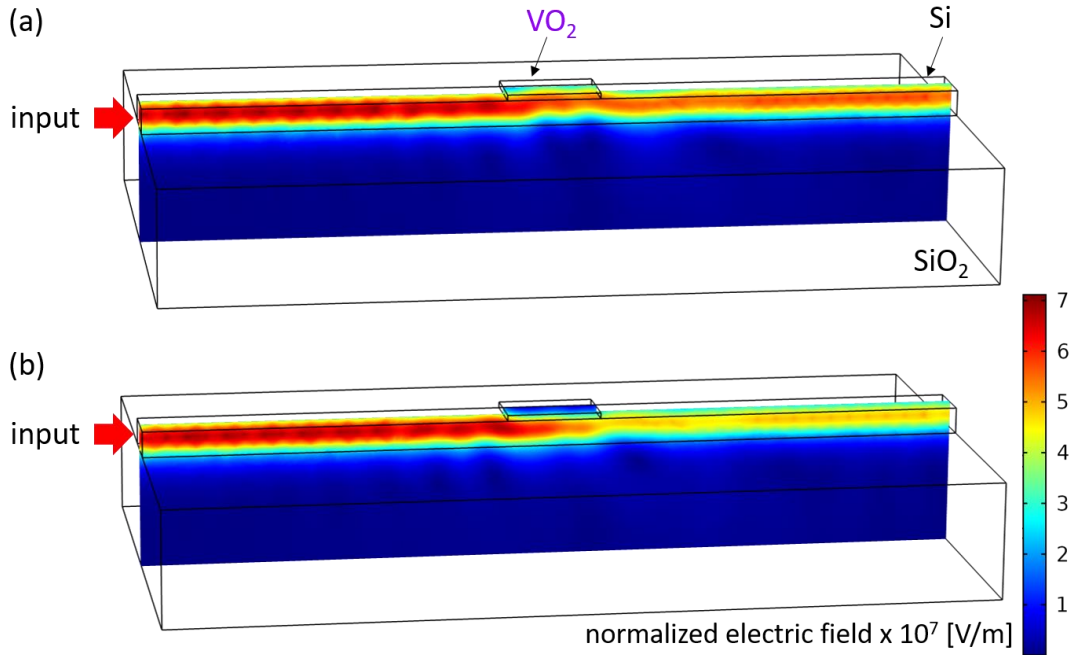


**Figure 7.4:** FEM simulation of the normalized electrical field for the TE mode. The VO<sub>2</sub> structure on top of the waveguide has a length of 0.8 μm and a thickness of 50 nm. (a) The VO<sub>2</sub> is in insulator state ( $T < T_{tr}$ ) and nearly the entire light is transmitted to the output. (b) The input light is largely absorbed by the VO<sub>2</sub> in metal state ( $T > T_{tr}$ ).

Figure 7.6 shows the power flow along the propagation direction for type 1 devices having the same thickness of 30 nm but different lengths from 1 to 4 μm. Clearly, by increasing the length of structures, more light is absorbed by VO<sub>2</sub> and, consequently, the transmission to the output decreases.

For optical switching, two transmitting states need to be distinguished: the total transmission with VO<sub>2</sub> in metal state  $T_M$  and in insulator state  $T_I$ . The optical loss in the *on* state of the system, due to the absorption of light by the insulator VO<sub>2</sub>, is expressed by the insertion loss IL, which is calculated in decibel (dB) by

$$IL = 10 \log T_I \quad (7.2)$$

In addition to IL, the other important parameter for optical characterizations is the extinction ratio ER. ER is also given in dB and defines the difference between the total transmission with VO<sub>2</sub> in metal and insulator states by

$$ER = 10 \log \left( \frac{T_M}{T_I} \right) \quad (7.3)$$

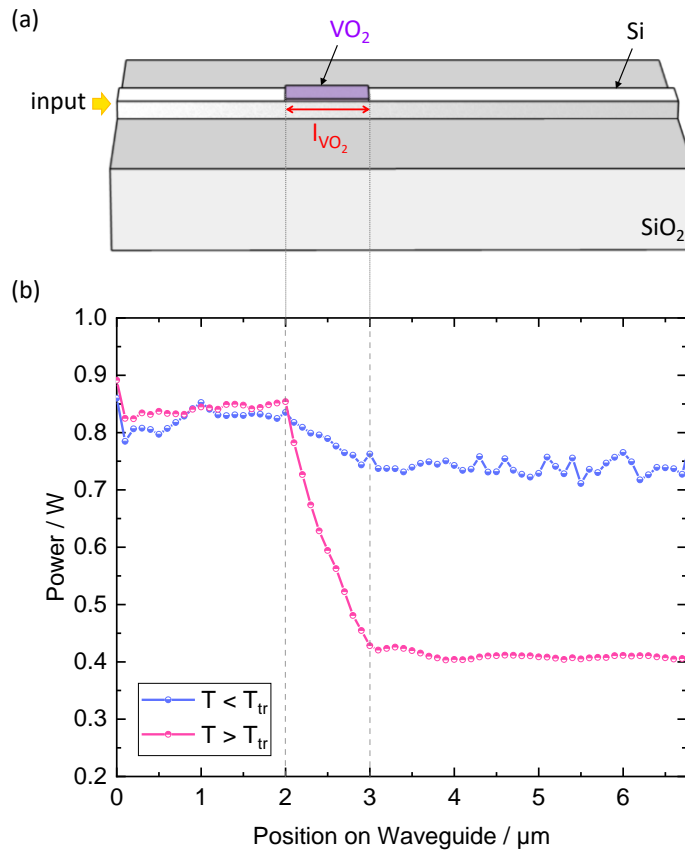


**Figure 7.5:** (a) Geometry illustration of the photonic device type 1 with air cladding. The VO<sub>2</sub> structure on top of Si has a length of  $l_{VO_2} = 1 \mu\text{m}$  and a thickness of 30 nm. (b) Power profile of the TE mode along the propagation direction in insulator state  $T < T_{tr}$  and in metal state  $T > T_{tr}$ . The position at the beginning and the end of the VO<sub>2</sub> structure is indicated by dashed lines.

For an efficient switching, IL needs to be minimized, hence, the power absorption by the insulator state should be as small as possible. Additionally, larger ERs are beneficial and can be achieved, as the power absorption in metal state increases.

In Figure 7.7, the IL and the ER of type 1 devices in dependence of the length of the VO<sub>2</sub> structure  $l_{VO_2}$  are plotted for thicknesses of VO<sub>2</sub> structures from 10 to 100 nm. Clearly, the geometry of the VO<sub>2</sub> structure has a large impact on the light modulation performance of the device. In Figure 7.7a, IL grows with increasing thickness. This is explained by the fact that the overlap of modes with VO<sub>2</sub> enhances for larger thicknesses, which leads to the higher absorption of the guided light into the VO<sub>2</sub> layer. In Figure 7.7b, EL first increases by decreasing thickness down to 30 nm, however, it drops when thickness is further reduced. In fact, for films thinner than 30 nm, overlap of modes with VO<sub>2</sub> and, thus, the absorption by the metal VO<sub>2</sub> is so small that the difference of the total transmitted light between *on* and *off* states declines.

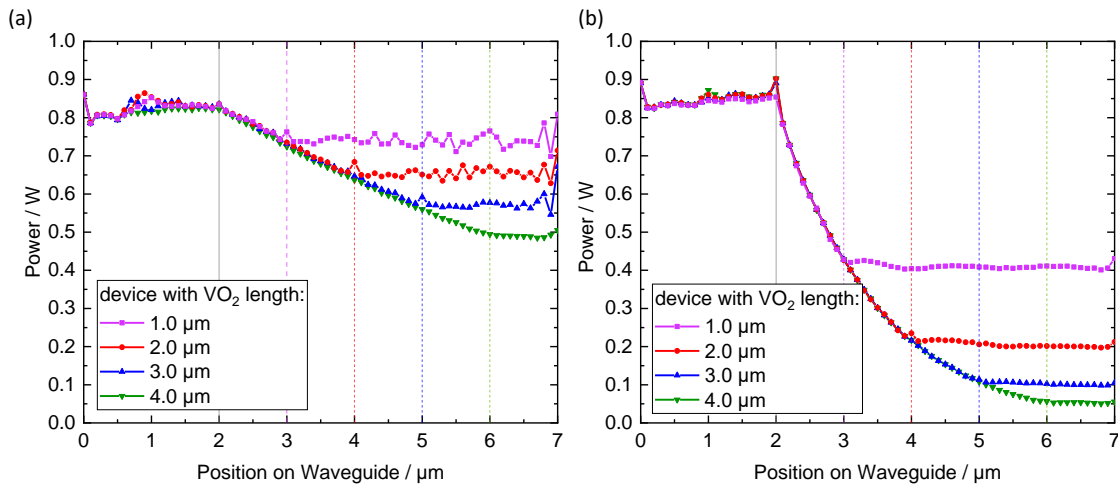


**Figure 7.6:** Simulated optical power flow of the TE mode along the propagation direction of the type 1 device with an air cladding at (a)  $T < T_{tr}$  and (b) at  $T > T_{tr}$ . Different colors indicate devices with VO<sub>2</sub> structures having different lengths. The position of the beginning and the end of VO<sub>2</sub> structures are indicated by dashed lines.

In order to find out the optimized design with a low IL and an improved ER, geometry parameters need to be adjusted. For a better comparison, IL and ER are determined with respect to the length of VO<sub>2</sub> structures  $l_{VO_2}$ . Figure 7.8 shows IL/length and ER/length as a function of VO<sub>2</sub> thickness for TE and TM modes of type 1 and type 2 devices. It is obvious that IL/length increases for all devices with increasing thickness. For type 1 devices and TM mode, the IL/length indicates the largest value of 5.4 dB/μm for the 100 nm thick VO<sub>2</sub> structure. ER/length curves show maxima in all cases. The maximum values of ER/length determined from Figure 7.8 and corresponding values of IL/length and VO<sub>2</sub> thicknesses are listed in Table 7.2. The highest ER/length is determined to be 10.3 dB/μm in TE-mode for device type 2 with VO<sub>2</sub> film thickness of 40 nm. In this case, a relative low IL/length of 2 dB/μm is obtained.

**Table 7.2:** Maximum ER/length and the corresponding IL/length and VO<sub>2</sub> thicknesses for various devices determined from FEM simulations.

Device – Optical Mode	Maximum ER/ $l_{VO_2}$ [dB/μm]	IL/ $l_{VO_2}$ at max. ER/ $l_{VO_2}$ [dB/μm]	VO <sub>2</sub> Thickness at max. ER/ $l_{VO_2}$ [nm]
Type 1 – TE	2.1	1.0	30
Type 1 – TM	4.5	0.6	20
Type 2 – TE	10.3	2.0	40
Type 2 – TM	2.4	1.0	20

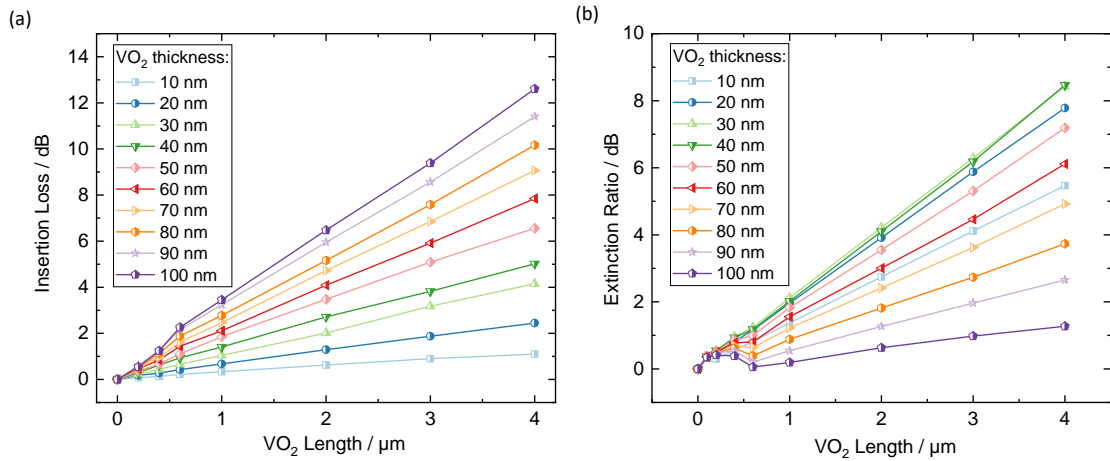


**Figure 7.7:** Simulated (a) insertion loss and (b) extinction ratio of TE modes in type 1 devices with air cladding for VO<sub>2</sub> structures having different lengths and thicknesses.

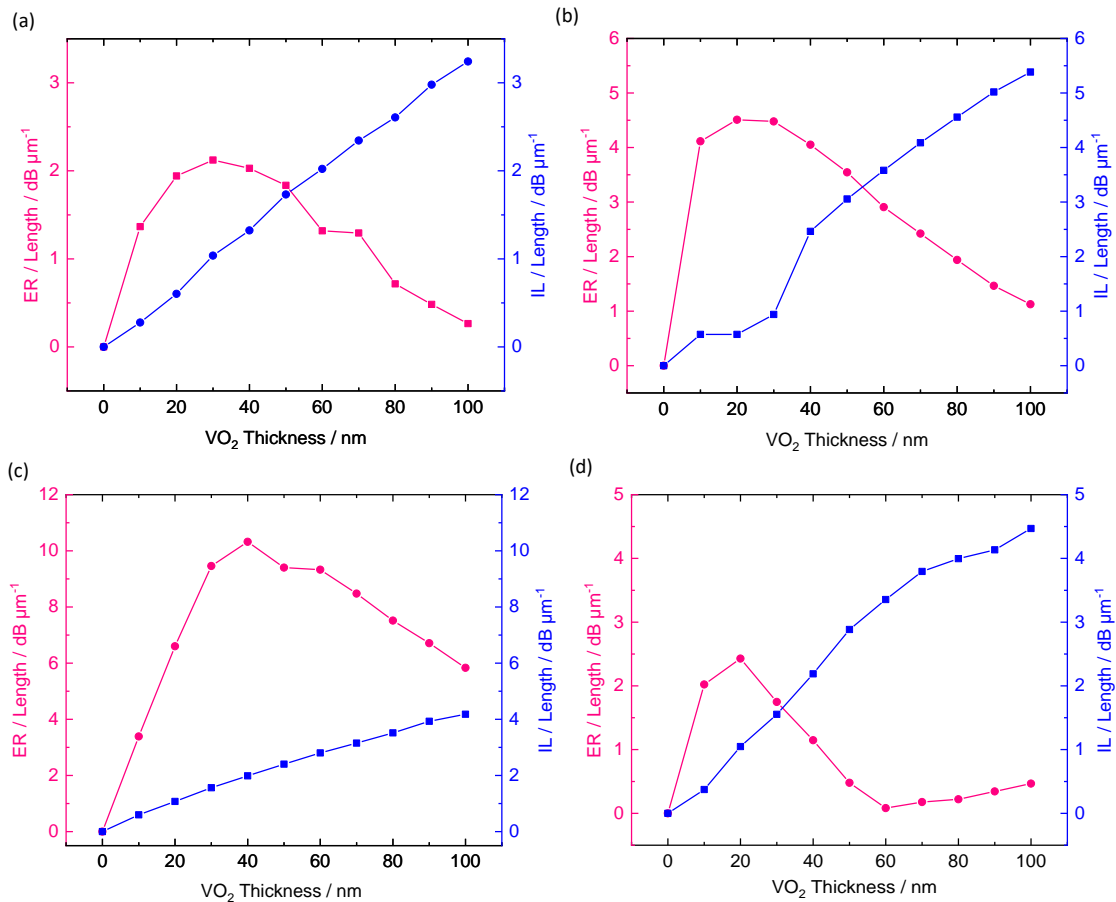


**Figure 7.8:** Simulated extinction ratio ER and insertion loss IL per length  $l_{\text{VO}_2}$  for (a) the TE mode in device type 1, (b) the TM mode in device type 1, (c) the TE mode in device type 2 and (d) the TM mode in device type 2.

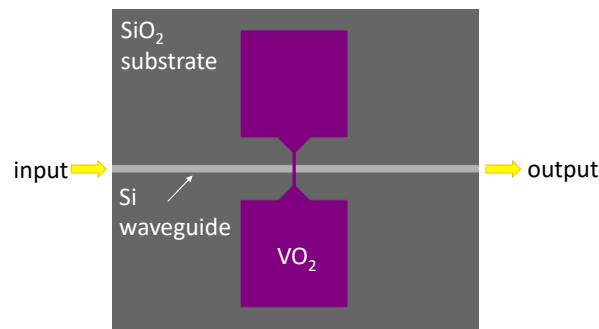


**Figure 7.9:** Schematic of the design of type 2 devices with integrated large pads ( $0.5 \times 0.5 \mu\text{m}^2$ ) for electrical connections.

## 7.4 Fabrication

The layout includes designs of type 1 and type 2 devices, as introduced in section 7.2. In addition, structures of type 2 devices with large  $\text{VO}_2$  pads are included in the layout (see Figure 7.9). These pads cover both sides of the waveguide and are provided for electrical connections via wire bonding or by using pico-probes, through which the metal-insulator transition of  $\text{VO}_2$  can be detected. The length of  $\text{VO}_2$  pads on the waveguide varies from  $l_{\text{VO}_2} = 0.2$  to  $10 \mu\text{m}$ . Two designs for grating couplers are used (see Figure 7.10), which are optimized for out-of-plane coupling of TE [166] and TM modes at the wavelength of  $1550 \text{ nm}$ , which has been previously developed in-house.

The top-down fabrication comprises nanomachining of the substrate prior to the film deposition, comparable to the nanofabrication method explained in section 5.2. Here, the  $\text{VO}_2$  film requires to be locally deposited on defined positions. The fabrication flow is depicted in Figure 7.11. A SOI chip is used as the initial substrate having a  $220 \text{ nm}$ -thick Si device layer and a  $2 \mu\text{m}$  thick buried oxide layer. First, Si waveguides and grating couplers are fabricated through electron beam lithography (EBL) and cryogenic etching of the Si device layer by  $\text{SF}_6$  and  $\text{O}_2$  gases. Consequently, resist is removed by  $\text{O}_2$  plasma (Figure 7.11a,b). In the next step, local openings are defined for deposition of  $\text{VO}_2$ . Therefore, a PMMA bilayer (refer to section 4.3) is spin-coated, followed by the e-beam exposure and development of the resist (Figure 7.11c). The thickness of the bilayers is adjusted with respect to the waveguide thickness of  $220 \text{ nm}$ . The lower PMMA layer is more sensitive to the developer and has a thickness of  $\sim 450 \text{ nm}$ . The upper PMMA layer has a higher molecular weight and a thickness of  $\sim 150 \text{ nm}$ . Afterwards, a  $\text{VO}_2$  film is deposited by reactive sputtering (refer to section 5.1) at room temperature and an oxygen flow rate of  $5.6 \text{ sccm}$  (Figure 7.11d). Subsequently, the PMMA bilayer is removed through a lift-off process inside an ultrasonic bath of acetone. Finally, the sample is post-annealed to the temperature of  $550 \text{ }^\circ\text{C}$  to obtain functional crystalline films (Figure 7.11e). Material deposition at room temperature in step (Figure 7.11d) is essential for effortless removal of the PMMA bilayer by the lift-off process.

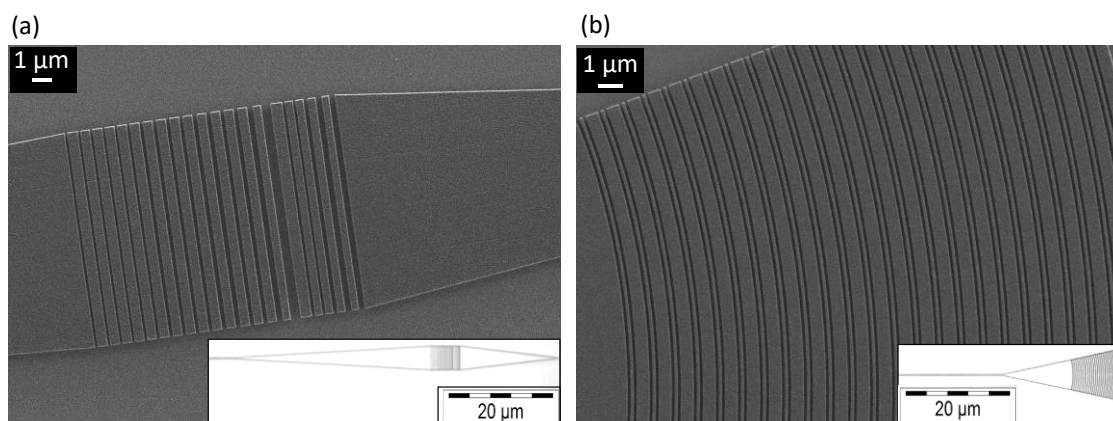


**Figure 7.10:** Scanning electron micrographs of Si grating couplers for out-of-plane light coupling of (a) TE modes and (b) TM modes at the wavelength of 1550 nm.

However, the sputtering of  $\text{VO}_2$  films at room temperature is very sensible to the oxygen flow rate with a tolerance of  $\sim 0.1$  sccm. Based on this method, devices with  $\text{VO}_2$  films of various thicknesses from 20 to 100 nm are fabricated. The SEM image of a preliminary fabricated device with a film thickness of 60 nm is shown in Figure 7.12. Observations indicate that films deposited on top of Si waveguides are homogenous. In contrast, the homogeneity of films on the  $\text{SiO}_2$  substrate is reduced, and, deposition on sidewalls of waveguides is not uniform for most devices. Furthermore, films indicate less dense structures upon decreasing the thickness. Based on this method only type 1 devices could be fabricated with  $\text{VO}_2$  structures covering only the top of Si waveguides.

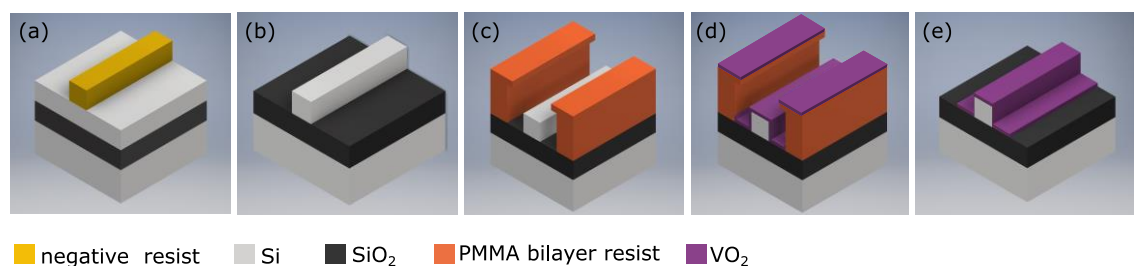


**Figure 7.11:** Fabrication flow of  $\text{VO}_2$ -based photonic switches. (a) Patterns of waveguides and grating couplers are transferred to the Si device layer by e-beam lithography. (b) Si is etched anisotropically through a cryogenic etching process. Afterwards, resist is removed by  $\text{O}_2$  plasma. (c) After spin-coating of a PMMA bilayer, local openings are defined through a second e-beam lithography step. (d)  $\text{VO}_2$  is sputtered from top on the sample. (e) After a lift-off process, samples are post-annealed at 550 °C.

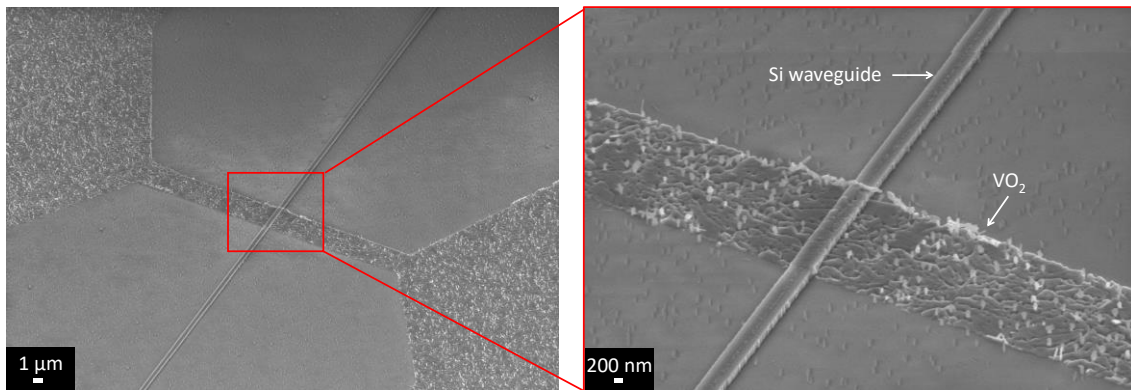


**Figure 7.12:** Scanning electron micrographs of a fabricated type 2 device with large pads for electrical connections. The thickness of the  $\text{VO}_2$  film is 60 nm. Small cylinders distributed on the substrate are black silica structures that are produced by cryogenic Si etching, due to slight fluctuations of etching parameters inside RIE chamber.

## 7.5 Optical Transmission Measurements

The optical performance of test devices is determined by transmission measurements. Prior to measurements, samples are coated with PMMA layers to protect nanostructures from dust particles. The optical setup and routine of measurements are described in the following section.

### 7.5.1 Optical Measurement Setup

The measurement setup is shown in Figure 7.13. It allows for out-of-plane light coupling through integrated grating couplers at inputs and outputs of individual optical devices. A tunable laser is swept in the wavelength range of 1480 – 1580 nm. The polarization is controlled to match coupling conditions of the on-chip grating couplers. The laser light is coupled into an optical fiber, which is aligned on top of the input grating coupler. The transmitted light is collected by a second optical fiber at the output grating coupler and its intensity is recorded by an optical spectrum analyzer (OSA). To avoid coupling losses (refer to the section 3.2), precise alignment of fibers and grating couplers is essential. Therefore, fibers are fixed on multi-axis stages that provide positioning in three translational directions x-y-z with  $\mu\text{m}$  resolution. Also, the inclination of fibers is adjustable with respect to the substrate. The sample is fixed on a rotational stage with  $\mu\text{m}$  precision. The position of fibers and structures on the sample are monitored through a microscope objective (12x) mounted on a CCD camera, which is connected to a PC. In order to perform temperature-dependent measurements, a cooling-heating system by water flow is integrated inside the sample holder capable of tuning the temperatures between 15 °C and 90 °C.

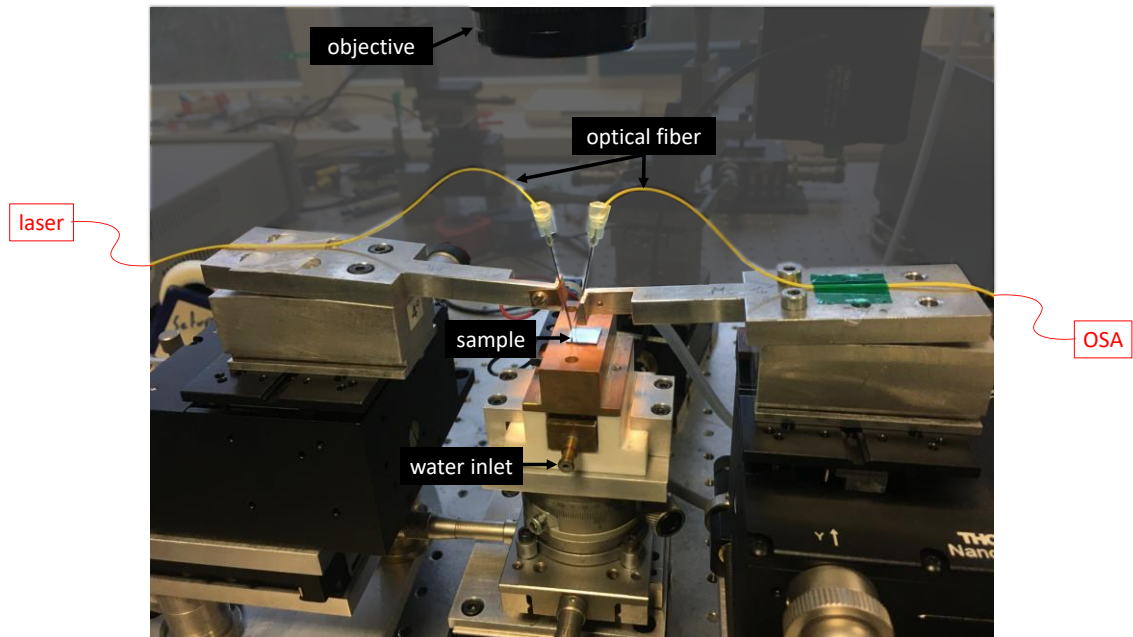


**Figure 7.13:** Optical setup for transmission measurements. Laser light is coupled by an optical fiber through a grating coupler into the waveguide. The transmitted light is coupled out to a fiber through a second grating coupler. The intensity is measured by an optical spectrum analyzer. The sample is placed on a rotational stage. Inlet and outlet ports allow for heating/cooling by injection of water at different temperatures.

### 7.5.2 Measurement Routine

Figure 7.14 shows transmission spectra of a type 1 device with the  $\text{VO}_2$  structure having a thickness of 40 nm and a length of  $l_{\text{VO}_2} = 4 \mu\text{m}$ . The grating coupler of the device was optimized to allow for the operation with TM modes. Devices with TE-mode grating couplers showed rough surfaces due to fabrication problems and could not be measured. The observed minima in transmission curves are caused due to coupling characteristics of grating couplers.

First, temperature is set to 20 °C and the spectrum is recorded for the *on* state (insulator state). Subsequently, the sample is heated to 80 °C above the transformation temperature and another spectrum is measured for the *off* state. Clearly, the transmitted intensity is decreased at 80 °C indicating the higher absorption of light in metal state compared to the transmitted intensity at 20 °C (insulator state). However, measured intensities for both *on* and *off* states are relatively weak, due to different loss mechanisms (refer to section 3.2). Impurities after fabrication in general and, especially, surface and side-wall roughness are main causes of attenuation in waveguides. Additionally, black silica structures and dust particles in the vicinity of waveguides and grating couplers reduce the transmission further.

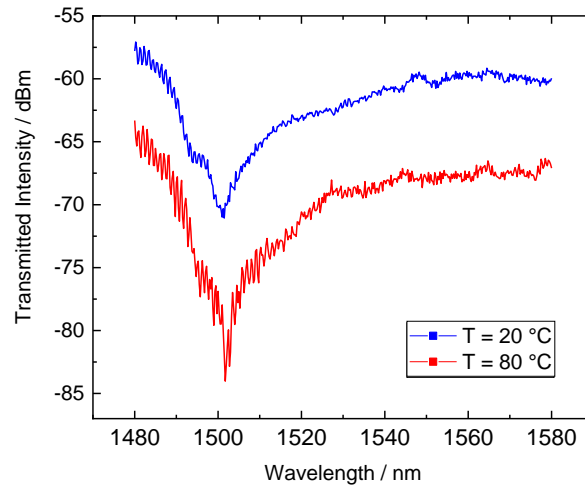


**Figure 7.14:** Transmitted power intensity of a type 1 device operating with TM mode. The VO<sub>2</sub> structures has a thickness of 40 nm and a length of  $l_{\text{VO}_2} = 4 \mu\text{m}$ . After heating of the sample from 20 to 80 °C, the transmission decreases.

Moreover, homogeneous heating of the whole sample leads to further decrease of transmitted intensity due to losses caused by thermal expansions of waveguides and grating couplers and changes in effective refractive indices of device components. Therefore, in the following, measured transmitted intensities at each temperature are normalized with respect to the intensity of a reference device having no VO<sub>2</sub> structure.

Transmission measurements are performed on devices with VO<sub>2</sub> structures having various lengths  $l_{\text{VO}_2}$  and thicknesses of 40 and 60 nm at two different temperatures, i.e. 20 °C and 80 °C. Mean values of normalized transmitted intensities at TM mode for different lengths  $l_{\text{VO}_2}$  are plotted in Figure 7.15. Accuracies of measured values are estimated from statistical analysis of averaged normalized intensities considering uncertainties due to precision of experiments. It is observed that for both hot and cold measurements, transmission decreases by increasing length  $l_{\text{VO}_2}$ , due to larger absorption by VO<sub>2</sub>. As it can be seen in Figure 7.15a for devices with VO<sub>2</sub> thickness of 40 nm, normalized transmitted intensities at 80 °C show a larger decrease by increasing  $l_{\text{VO}_2}$  compared to intensities at 20 °C. This is a result of the higher absorption in metal state indicating optical switching. However, no significant difference is observed between normalized transmitted intensities of hot and cold devices for  $l_{\text{VO}_2} < 2 \mu\text{m}$ , due to the smaller overlap of modes with VO<sub>2</sub>, which results in the weakened switching characteristic. This is also the case for devices with VO<sub>2</sub> structures having a thickness of 60 nm in Figure 7.15b. Nevertheless, existing loss mechanisms in the system play an important role for interpretation of results, particularly, for devices with  $l_{\text{VO}_2} < 2 \mu\text{m}$ .

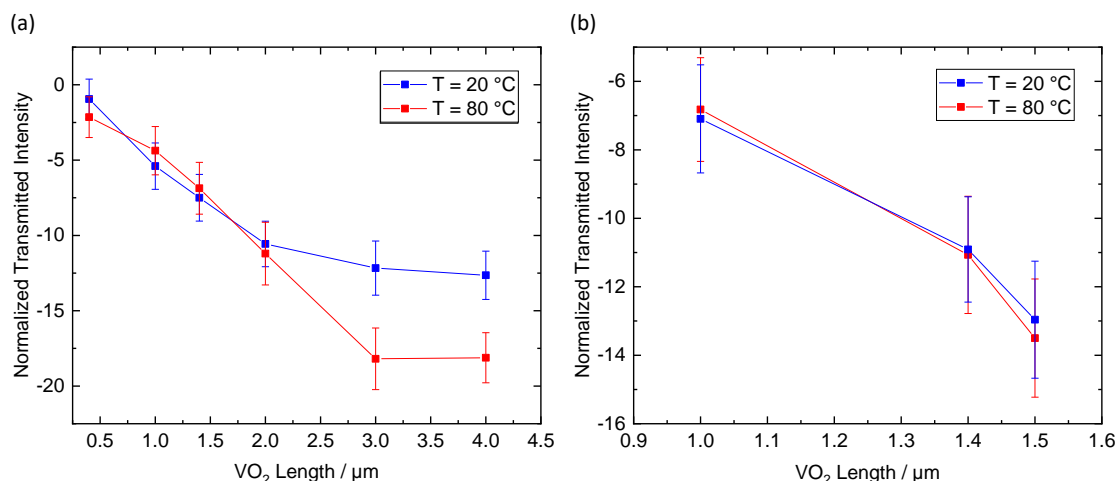


**Figure 7.15:** Normalized transmitted intensities as a function of length of the VO<sub>2</sub> structure  $l_{\text{VO}_2}$ , measured at temperatures of 20 and 80 °C for a type 1 device with the VO<sub>2</sub> having a thickness of 40 nm (a) and a thickness of 60 nm (b). Error bars are determined from statistical analysis of multiple measurements. Transmission measurements on the chip with the VO<sub>2</sub> having a thickness of 60 nm was limited to short VO<sub>2</sub> structures,  $l_{\text{VO}_2} \leq 1.5 \mu\text{m}$ , due to some fabrication errors on parts of the chip.

Losses caused by surface scattering, thermal expansion or change in effective refractive indices of device components due to heating may dominate and compensate the optical switching effect.

## 7.6 Summary

In this chapter, the concept of photonic switching based on the insulator-metal transition of VO<sub>2</sub> films is investigated. The complex refractive indices of films are determined by ellipsometry at temperatures lower and higher than the transformation temperature. The large change of the complex indices, especially at the wavelength of 1550 nm, is a key feature required for switching in photonic circuits. The concept of the design and optical performance of devices are studied by 3D FEM simulations considering various geometries. The highest extinction ratio per length  $ER/l_{\text{VO}_2} \sim 10.3 \text{ dB}/\mu\text{m}$  is measured for a TE-mode device with the VO<sub>2</sub> film covering the top and side walls of the Si waveguide and a film thickness of 40 nm. The developed fabrication flow, based on sputtering of VO<sub>2</sub> films at room temperature and subsequent post annealing, allows for local depositions with defined patterns. Based on this method, functional VO<sub>2</sub> films with thicknesses down to 20 nm are realized. Optical performances of fabricated devices are investigated by temperature-dependent transmission measurements. Devices operating at  $T = 80 \text{ °C}$  indicate lower transmitted intensities for TM-mode compared to devices at  $T = 20 \text{ °C}$  demonstrating optical switching characteristics. The homogeneous heating of the whole sample

leads to different losses, e.g. caused by thermal expansions of waveguides and grating couplers or changes in effective refractive indices of device components. In order to reduce these effects, the temperature of VO<sub>2</sub> structures require to be altered locally either by Joule heating or optically using a free-space laser light.

## 8 Summary and Conclusion

The focus of this thesis is on VO<sub>2</sub>-based test devices for electrical and structural characterization of size effects in the nanoscale. The starting material for nanofabrications are VO<sub>2</sub> thin films that are fabricated by our collaborators at Ruhr-Universität Bochum (RUB). VO<sub>2</sub> films exhibit a reversible martensitic transformation at 67 °C combined with multifunctional properties such as insulator-metal transition or drastic changes in the electrical resistance and optical transmittance in the IR-wavelength range. The first aim of this thesis is the design, development and evaluation of VO<sub>2</sub>-based nanodevices for systematic geometry and size-dependence investigations. Another key point of this research is to study nanoactuation characteristics in bimorph cantilevers based on VO<sub>2</sub> films. Furthermore, these understanding are adapted to establish VO<sub>2</sub>-based demonstrator devices for nanotechnology applications. For this purpose, optical properties of VO<sub>2</sub> films are investigated and the concept of optical switching based on the insulator-metal transition in VO<sub>2</sub> is investigated.

The first part of this work was dedicated to developing fabrication flows to realize nanostructures based on VO<sub>2</sub> thin films. Reactive magnetron sputtering is used for the deposition of VO<sub>2</sub> and V<sub>1-x</sub>M<sub>x</sub>O<sub>2</sub> films doped by a third material (M), such as VMoO<sub>2</sub> films. This method allows for a flexible tuning of film properties such as the morphology and the crystallinity, thus enabling the modification of the metal-insulator transition properties and the transition temperature. Top-down and bottom-up nanostructuring methods are introduced based on the EBL and etching techniques aiming at reproducible fabrication flows which enable scaling down to the grain size of around 100 nm. The two top-down methods include either the nanomachining of SOI substrates prior to the deposition of V<sub>1-x</sub>M<sub>x</sub>O<sub>2</sub> films or the direct nanostructuring of V<sub>1-x</sub>M<sub>x</sub>O<sub>2</sub> films deposited on SiO<sub>2</sub>/Si substrates. Based on the latter process, free-standing double-beam and bridge structures with lateral sizes down to 100 nm are realized indicating smooth sidewalls. Double-beams are deposited with a thin layer of Cr to achieve bimorph nanoactuators. Another fabrication approach consists of the deposition of VO<sub>2</sub> films on pre-structures Si pillar. This method results in columnar growth of VO<sub>2</sub> nanopillars reaching the limit of single-crystalline and oligocrystalline state.

Temperature-dependent electrical characteristics of VO<sub>2</sub> films and nanostructures are studied by four-terminal electrical measurements inside a thermostat to investigate possible size effects. The introduced sample preparation technique and the measurement setup enables a systematic study of a series of nanostructures fabricated with the same parameters on a single chip. Electrical resistance measurements are performed on VMoO<sub>2</sub> nanobridges having the same length of 5 μm and various thicknesses from 900 nm down

to 200 nm. The characteristic insulator-metal transition is also observed for  $\text{VMoO}_2$  nano-bridges indicating that the phase transition persists after the nanofabrication, independent of the lateral width of structures. Detailed analyses reveal that transition temperatures do not indicate any considerable width-dependence down to 200 nm being close to the average grain size of 100 nm. Besides, electrical resistance of nanobridges in the semiconductor state follows the electrical characteristic of homogeneous materials and scales inversely proportional to the lateral widths. Consequently, the width-dependence of electrical resistance does not indicate any size effect down to a width of 200 nm as well. Nevertheless, the electrical resistance change upon the insulator-metal transition increases by decreasing the lateral width. This enhanced change is attributed to the reduced carrier scatterings at grains boundaries, since the absolute number of grains decreases for declining lateral widths of structures.

Actuation characteristics of  $\text{Cr/VMoO}_2$  nanoactuators using double-beam geometry are studied through in-situ measurements inside a SEM. Thermal actuation is realized either by Joule-heating of individual structures or by altering the sample temperature homogeneously. To achieve the latter, a micro heating-cooling stage (MHCS) is developed, which enables in-situ temperature-dependent experiments inside a SEM under quasi-stationary conditions. The out-of-plane deflection of  $\text{VMoO}_2$  nanoactuators exhibit non-linear displacement characteristics during the structural phase transformation. A large actuation stroke of around 15 % is achieved for  $\text{Cr/VMoO}_2$  nanoactuators with length of 12  $\mu\text{m}$  and width of 600 nm.

It is shown that the continuous observation of  $\text{VO}_2$ -based films and structures by the SEM at temperatures below 0 °C leads to an irreversible change of the crystal structure, which results in degradation of phase transformation properties and strongly reduces the actuation stroke. Consequently, temperature-dependent observations inside the SEM need to be limited to a single cooling track. Hence, it is essential to develop new techniques, which involve optical methods instead of using SEM for local sensing of the beam deflection.

Furthermore, optical characteristics of  $\text{VO}_2$  films in insulator and metal states are investigated to develop  $\text{VO}_2$ -based photonic switching devices. The operation concept is to modulate and to switch the propagation of light in Si waveguides based on the metal-insulator transition in  $\text{VO}_2$ . Therefore, two type of devices are considered, in which  $\text{VO}_2$  films cover parts of Si waveguides. The first type of devices is realized by deposition of the  $\text{VO}_2$  film on top of the waveguide, whereas in the second type, the  $\text{VO}_2$  film covers both the top and sidewalls of the waveguide. The concept of the design and the optical performance are studied by 3D FEM simulations, and the performance of devices are investigated experimentally for devices operating with TE and TM optical modes. To find an optimized design, geometry parameters are varied including the thickness and the length of  $\text{VO}_2$  structures. Based on this analysis, the highest extinction ratio per length

$ER/l_{VO_2}$  of  $\sim 10.3$  dB/ $\mu\text{m}$  is achieved for a TE-mode device with a  $VO_2$  structure of 40 nm thickness.

A method to fabricate  $VO_2$ -based photonic switching device is developed based on EBL and RIE techniques, as well as the sputtering of  $VO_2$  films at room temperature followed by a post annealing process. Optical performances of TM-mode devices with  $VO_2$  structures on top of waveguides are investigated by temperature-dependent transmission measurements. Results indicate a reduction of the transmission for the hot (metal) state in comparison to the cold (insulator) state demonstrating *on* and *off* optical switching.



## 9 Outlook

Further investigations on possible size effects in the nanoscale will be achieved by decreasing film thicknesses and reducing lateral widths of fabricated structures to reach oligocrystalline configurations. For this purpose, a novel approach based on the direct nanomachining of films and the growing of VO<sub>2</sub> nanopillars on Si columns shows promising results. However, for future fabrication of VO<sub>2</sub> nanopillars, deposition on the substrate and sidewalls needs to be prevented. Therefore, a second EBL step will be required after fabricating Si nanostructures. For this step, the layout should include design of inverse forms with respect to Si patterns. After spin-coating, e-beam exposure and resist development, the VO<sub>2</sub> film will be deposited. The resist will be then removed by a lift-off process. Hence, VO<sub>2</sub> structures remain only on Si structures.

Electrical resistance measurements on free-standing nanobridges with lateral widths smaller than 100 nm could not be determined due to instabilities and abrupt changes in electrical current. Therefore, more sensitive electrical measurement techniques are required such as in situ methods by electrical connecting using nanomanipulators. An alternative method is by scanning the surface of the structure using a conductive atomic force microscope (AFM) tip [36]. In this method, the displacement current between the sample and the AFM tip is measured, which is converted to a microwave signal that carries information on the conductivity of the sample [36]. The advantage of this technique is that electrical contacts used in two- and four-terminal methods are eliminated. Consequently, no electrical current flows along the structure, thus, overheating and melting can be prevented.

It is shown in section 6.2 that the continuous observation of VO<sub>2</sub>-based films and structures leads to anomalous alteration of morphology and crystallinity. The physical nature of the change in the crystallinity requires to be investigated. Therefore, FIB cut can be applied along the deformed structures to observe their cross sections, e.g. by a SEM, to determine possible structural changes in layers of the bimorph. In addition, transmission electron microscopy (TEM) can be used to investigate changes in the crystallinity by detecting grain boundaries and defects as well as phase analysis.

For a better understanding of actuation characteristics of Cr/VMoO<sub>2</sub> double-beams, different material properties require to be determined including lattice constants and thermal expansion coefficients of the austenite (A) and martensite (M1, M2) phases of the VMoO<sub>2</sub>. Additionally, it is important to determine the exact temperature of the substrate during deposition of the Cr top layer to be able to define the initial bending of the bimorph after cooling down to room temperature. Besides, additional in-situ experiments are required on bimorph double-beams having various film thickness and further downsizing of structures to investigate size effects.

In order to optimize the optical modulation performance of devices introduced in section 7, further design concepts and geometry optimization has to be considered. Generally, it is beneficial to downsize the VO<sub>2</sub> structure, since by reducing the thermal mass, less energy is required to prompt the insulator-metal transition in VO<sub>2</sub>. New device designs could include, for instance, VO<sub>2</sub> coatings with smaller lateral width than the waveguide width. The advantage of this design is the compatibility with the nanofabrication method based on the lift-off process. Alternatively, the design of device may consist of a set of discret VO<sub>2</sub> nano islands deposited on top of a waveguide to achieve nano optical switching.

Learning about the optical performance of nano-structured switches can be achieved by FEM simulations using a physics-controlled fine meshing. Additionally, the model should consider the effect of surface plasmons. Therefore, the plasmon frequency of VO<sub>2</sub> should be determined by ellipsometry.

Furthermore, all optical constants of VO<sub>2</sub> films, e.g.  $n$  and  $\kappa$ , need to be measured by ellipsometry for a continuous temperature range. The obtained data provide input material parameters for simulations, also, they are necessary for the implementation of experimental results.

For the fabrication of photonic devices, the roughness of waveguides must be minimized by improving step parameters of the EBL and the plasma cryo etching. As shown in section 7.4, despite rotation of substrates during sputtering of VO<sub>2</sub> films, almost no deposition occurs on sidewalls of waveguides. Thus, in order to realize type 2 devices with VO<sub>2</sub> covering both the top and sidewalls of the waveguide, it is necessary to sputter VO<sub>2</sub> with defined incidence angles on tilted samples. Afterwards, optical transmission measurements should also be performed also on devices using TE mode.

Aiming at VO<sub>2</sub> nano switches as built-in structures in photonic devices, a fabrication flow is proposed to integrate a VO<sub>2</sub> film in an existing plasmonic photodetector, as discussed in the following.

An internal photoemission plasmonic photodetector (PIPED) has been previously developed [167]. As illustrated in Figure 9.1, the PIPED structure consists of a tapered Si waveguide, which is sandwiched between two different metal pads, i.e. Au and Ti with thicknesses of  $\sim 30$  nm. The Au-Si-Ti junction creates a semiconductor-metal waveguide that allows for the propagation of SPPs. The energy of SPPs is absorbed and generates hot electrons in Ti. Applying a positive electrical potential at the Au pad enables internal photoemission from the Ti pad [167]. Similar to other integrated photonic devices, the functionality is often sensible to small variations in fabrication parameters and to slight fluctuations in the optical setup [168].

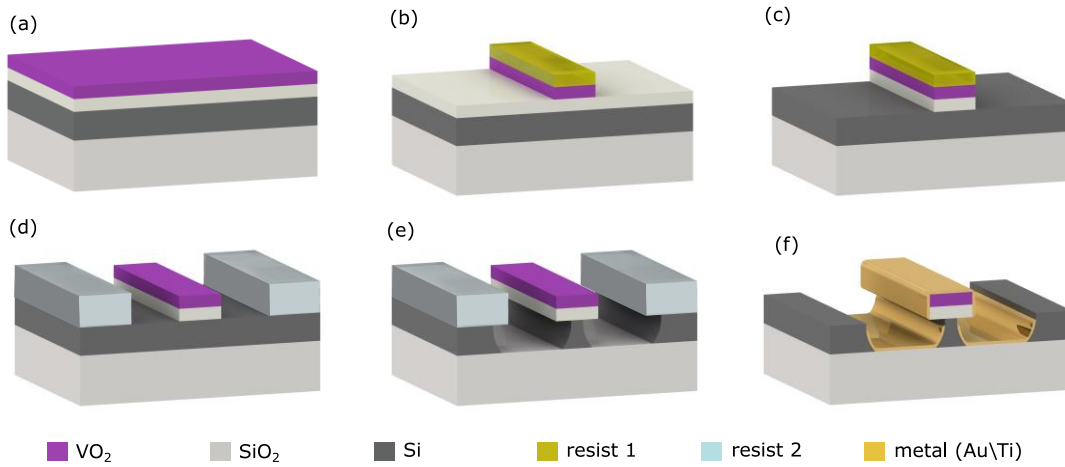


**Figure 9.1:** Schematic of the fabrication flow proposed to realize a PIPED with the integrated VO<sub>2</sub> optical fuse. (a) VO<sub>2</sub> is deposited on a SOI wafer with a SiO<sub>2</sub> coating on top. (b) After EBL, patterns are transferred to the VO<sub>2</sub> layer by RIE. (c) SiO<sub>2</sub> is anisotropically etched by RIE using CHF<sub>3</sub> gas. (d) After patterning of a PMMA bilayer through EBL, (e) tapered Si waveguides are realized by RIE using SF<sub>6</sub> gas at room temperature. (f) Metal pads are generated through EBPVD and lift-off process.

During optical measurements on PIPEDs, it has been observed that the mentioned problems may lead to overheating and, hence, to melting down of metal pads. To avoid these, the design and the fabrication flow of the PIPED could be modified to integrate a thin layer of VO<sub>2</sub>. Through an increase of input power in VO<sub>2</sub> metal state, the film absorbs the exceeding dissipated energy, which impedes further heating of device components, thus, preventing damage.

The suggested fabrication flow comprises multiple EBL and RIE steps. First, the VO<sub>2</sub> film is patterned (Figure 9.1b) and waveguide structures are produced (Figures 9.1a-c), followed by the undercut of the Si device layer to achieve tapered structures (Figures 9.1d-e). Next, metal contact pads are created through EBPVD and lift-off process (Figure 9.1f).

After successful fabrications, studies are required to determine exact operation parameters, such as the magnitude of the applied bias voltage and the threshold of the input optical power leading to a damage. Methods for preventing damages may include the triggering of the insulator-metal transition in VO<sub>2</sub> either optically or electrically. Consequently, the design of the device and the geometry of the VO<sub>2</sub> layer need to be optimized using simulation methods. Finally, transition properties of VO<sub>2</sub>-based films can be modified by doping or attuning of deposition parameters.



# Appendix A

## Ellipsometry Models of VO<sub>x</sub>-Based Films

As determined from SEM investigations, fabricated films in this work demonstrated relatively rough surfaces due to grain structures (see e.g. Figure 5.2). Two different models are used to describe construction of samples for ellipsometry analysis of films properties. Figure A.1a depicts a two-layer model, where the top layer is considered to include the effect of the surface roughness. Both top and bottom layers are based on the Tauc-Lorentz oscillators model, which is commonly used to describe the dielectric constant of amorphous semiconductors [169]. The model in Figure A.1b consists of a main layer of the VO<sub>2</sub> and a thin top layer introducing a random structure based on the effective medium approximation (EMA) of ellipsometric response from the random surface roughness [170,171].

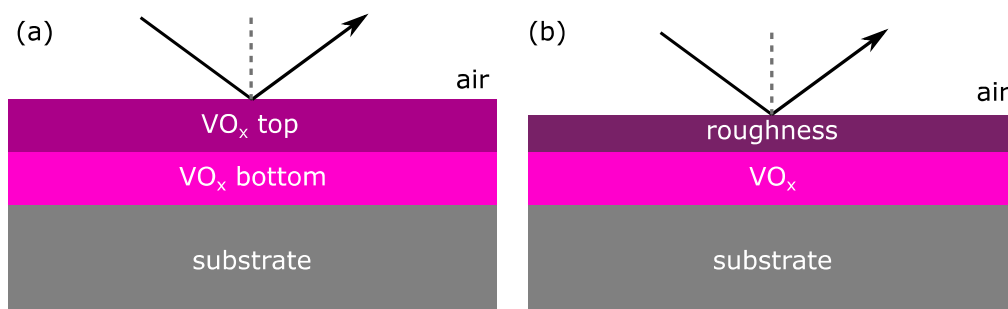


**Figure A.1:** Ellipsometry models of VO<sub>2</sub>-based films. (a) A two-layer model including layers based on Tauc-Lorentz dielectric materials. (b) A one-layer model having a roughness based on EMA.



# Appendix B

## Optimization of Thickness Ratio in Bilayer Cantilevers

The curvature  $\kappa$  of a bilayer cantilever with a rectangular cross section depends on biaxial moduli and thicknesses of the two layers. For a Cr/VO<sub>2</sub> bilayer cantilever the curvature is calculated by [137]

$$\kappa = \frac{6E_{\text{VO}_2}E_{\text{Cr}}t_{\text{VO}_2}t_{\text{Cr}}(t_{\text{VO}_2} + t_{\text{Cr}})}{E_{\text{VO}_2}^2t_{\text{VO}_2}^4 + 2E_{\text{VO}_2}E_{\text{Cr}}t_{\text{VO}_2}t_{\text{Cr}}(2t_{\text{VO}_2}^2 + 3t_{\text{VO}_2}t_{\text{Cr}} + 2t_{\text{Cr}}^2) + E_{\text{Cr}}^2t_{\text{VO}_2}^4} \varepsilon \quad (\text{B.1})$$

where  $\varepsilon$  is the total axial strain.  $t_{\text{Cr}}$  and  $t_{\text{VO}_2}$  are thicknesses of the Cr and the VO<sub>2</sub> layers, respectively.  $E_{\text{Cr}} \sim 280$  GPa and  $E_{\text{VO}_2} \sim 140$  GPa are Young's moduli of Cr and VO<sub>2</sub>, respectively. By considering these values and the spontaneous strain of the Cr/VO<sub>2</sub> bilayer in the order of  $10^{-2}$ , the maximum bending of the Cr/VO<sub>2</sub> cantilever is determined to occur for a thickness ratio of  $t_{\text{Cr}}/t_{\text{VO}_2} = 0.37$  [138].



# Appendix C

## Challenges of Nanofabrication Based on EBL and RIE

Fabrication in the nano-scale regime is challenging and requires profound understanding of all techniques and affecting parameters in theory and in practice, as described below.

For fabrications based on e-beam lithography and etching processes, the type of resist, its quality, thickness and adhesion to the surface of the substrate are important parameters. Moreover, how well the resist can persist the impact of the subsequent process steps plays a significant role. This includes the persistence of the resist against plasma etching and chemical etchants, which strongly depends on the dose of e-beam used to generate patterns (in  $\mu\text{C}/\text{cm}^2$ ). In addition, the e-beam dose and parameters for the resist development require to be adjusted with respect to each other.

As it can be seen in Figure C.1a, the VMoO<sub>2</sub> double-beam fabricated by the procedure described in 5.3 indicates ruffled edges as a result of wrong parameters of the EBL process. This problem was solved by attuning of process parameters such as by applying a thicker resist layer through reducing the rotation speed of spin-coating, also by increasing the e-beam dose for fine patterns. It is common that after analyses of fabrication results, layouts of designs require to be optimized. From experience, free-standing structures with high aspect ratios of the length to the beam width ( $l/w$ ) are more likely to collapse to the substrate. Figure C.1b shows a collapsed double-beam after the final process step of the critical point drying of the substrate. Therefore, in the following fabrications of double-beams with  $w > 400$  nm, a maximum aspect ratio of  $l/w = 20$  is considered.

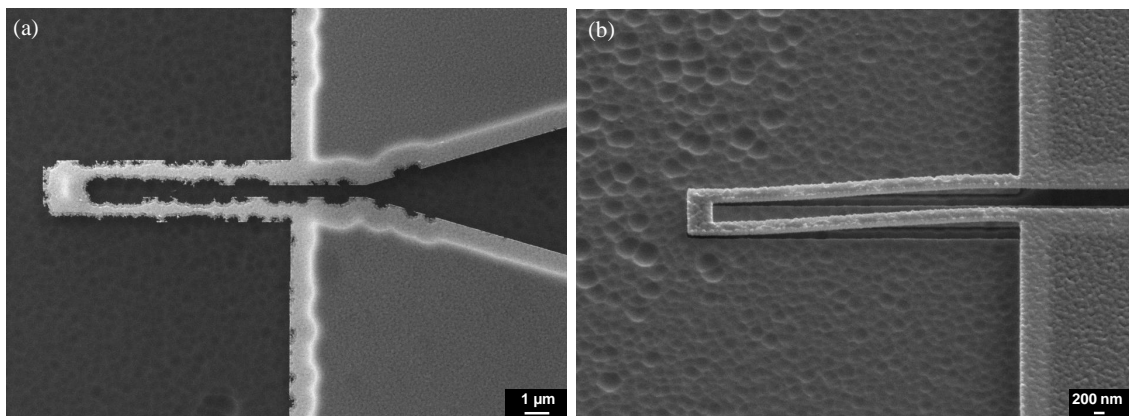


**Figure C.1:** Scanning electron micrographs of nano double-beams fabricated by the direct nanomachining of the VMoO<sub>2</sub> film on a SiO<sub>2</sub>/Si substrate. (a) A structure with rough edges due to incorrect parameters of the EBL process. (b) A collapsed double-beam with a beam width of 200 nm and a length of 6 μm, i.e.  $l/w = 30$ .



# References

- [1] A.B. Frazier, R.O. Warrington, C. Friedrich, The Miniaturization Technologies: Past, Present, and Future, *IEEE Trans. Ind. Electron.* 42 (1995) 423–430.
- [2] S.E. Miller, Integrated Optics: An Introduction, *Bell Syst. Tech. J.* 48 (1969) 2059–2069.
- [3] F. Chollet, Devices based on co-integrated MEMS actuators and optical waveguide: A review, *Micromachines.* 7 (2016) 1–33.
- [4] K. Hogari, T. Matsumoto, Electrostatically driven micromechanical  $2 \times 2$  optical switch, *Appl. Opt.* 30 (1991) 1253.
- [5] S.M.C. Abdulla, L.J. Kauppinen, M. Dijkstra, E. Berenschot, M.J. De Boer, R.M. De Ridder, G.J.M. Krijnen, Mechano-optical switching in a MEMS integrated photonic crystal slab waveguide, in: *Proc. IEEE Int. Conf. Micro Electro Mech. Syst. (MEMS)*, Cancun Mex., IEEE, Cancun, MEXICO (2011) 9–12.
- [6] W.M. Green, M.J. Rooks, L. Sekaric, Y.A. Vlasov, Ultra-compact, low RF power, 10 Gb/s silicon Mach-Zehnder modulator, *Opt. Express.* 15 (2007) 17106.
- [7] T. Tanabe, M. Notomi, S. Mitsugi, A. Shinya, E. Kuramochi, All-optical switches on a silicon chip realized using photonic crystal nanocavities, *Appl. Phys. Lett.* 87 (2005) 1–3.
- [8] C. Errando-Herranz, F. Niklaus, G. Stemme, K.B. Gylfason, Low-power microelectromechanically tunable silicon photonic ring resonator add – drop filter, *Opt. Lett.* 40 (2015) 3556–3559.
- [9] M. Liu, X. Yin, E. Ulin-Avila, B. Geng, T. Zentgraf, L. Ju, F. Wang, X. Zhang, A graphene-based broadband optical modulator, *Nature.* 474 (2011) 64–67.
- [10] C. Koos, P. Vorreau, T. Vallaitis, P. Dumon, W. Bogaerts, R. Baets, B. Esembeson, I. Biaggio, T. Michinobu, F. Diederich, W. Freude, J. Leuthold, All-optical high-speed signal processing with silicon-organic hybrid slot waveguides, *Nat. Photonics.* 3 (2009) 216–219.
- [11] M. Kohl, Shape memory microactuators, Springer, Berlin Heidelberg (2004) .
- [12] M. Kohl, M. Schmitt, A. Backen, L. Schultz, B. Krevet, S. Fähler, Ni-Mn-Ga shape memory nanoactuation, *Appl. Phys. Lett.* 043111 (2014) 2012–2017.
- [13] M. Gültig, Thermal energy harvesting based on metamagnetic shape memory alloys, Ph.D. Thesis, Karlsruhe Institute of Technology (KIT), 2014.
- [14] H. Ossmer, F. Lambrecht, M. Gültig, C. Chluba, E. Quandt, M. Kohl, Evolution of temperature profiles in TiNi films for elastocaloric cooling, *Acta Mater.* 81 (2014) 9–20.

- [15] F. Bruederlin, L. Bumke, C. Chluba, H. Ossmer, E. Quandt, M. Kohl, Elastocaloric cooling on the miniature scale: a review on materials and device engineering, *Energy Technol.* 6 (2018) 1588–1604.
- [16] F. Lambrecht, I. Aseguinolaza, V. Chernenko, M. Kohl, Integrated SMA-based NEMS actuator for optical switching, in: *Proc. IEEE Int. Conf. Micro Electro Mech. Syst.*, Shanghai, China (2016) 79–82.
- [17] C. Lay, I.R. Aseguinolaza, V.A. Chernenko, M. Kohl, In-situ characterization of ferromagnetic shape memory alloy / silicon bimorph nanoactuators, in: *14th IEEE Int. Conf. Nanotechnol.*, Toronto, Canada (2014) 192–195.
- [18] S. Rastjoo, R. Fechner, L. Bumke, M. Kötz, E. Quandt, M. Kohl, Development and co-integration of a SMA / Si bimorph nanoactuator for Si photonic circuits, *Microelectron. Eng.* 225 (2020) 111257.
- [19] R. Fechner, C. Chluba, E. Quandt, M. Kohl, A Shape Memory Alloy 1×2 Optical Waveguide Switch, in: *2018 IEEE 18th Int. Conf. Nanotechnol.*, Cork, Ireland (2018) 1–3.
- [20] F. J. Morin, Oxides Which show a Metal-to-Insulator Transition at The Neel Temperature, *Phys. Rev. Lett.* 29 (1972) 1361–1362.
- [21] Y. Ke, S. Wang, G. Liu, M. Li, T.J. White, Y. Long, Vanadium Dioxide: The Multistimuli Responsive Material and Its Applications, *Small.* 14 (2018) 1–29.
- [22] J. Narayan, V.M. Bhosle, Phase transition and critical issues in structure-property correlations of vanadium oxide, *J. Appl. Phys.* 100 (2006) 103524.
- [23] C. Cheng, K. Liu, B. Xiang, J. Suh, J. Wu, Ultra-long, free-standing, single-crystalline vanadium dioxide micro/nanowires grown by simple thermal evaporation, *Appl. Phys. Lett.* 100 (2012) 103111.
- [24] Y. Jiazhen, Z. Yue, H. Wanxia, T. Mingjin, Effect of Mo-W Co-doping on semiconductor-metal phase transition temperature of vanadium dioxide film, *Thin Solid Films.* 516 (2008) 8554–8558.
- [25] A. Lai, Z. Du, C.L. Gan, C.A. Schuh, Shape Memory and Superelastic Ceramics at Small Scales, *Science.* 341 (2013) 1505–1508.
- [26] H.W. Verleur, A.S. Barker, C.N. Berglund, Optical properties of VO<sub>2</sub> between 0.25 and 5 eV, *Phys. Rev.* 172 (1968) 788–798.
- [27] Y. Zhao, J. Hwan Lee, Y. Zhu, M. Nazari, C. Chen, H. Wang, A. Bernussi, M. Holtz, Z. Fan, Structural, electrical, and terahertz transmission properties of VO<sub>2</sub> thin films grown on c-, r-, and m-plane sapphire substrates, *J. Appl. Phys.* 111 (2012) 053533.
- [28] K.J.A. Ooi, P. Bai, H.S. Chu, L.K. Ang, Ultracompact vanadium dioxide dual-mode plasmonic waveguide electroabsorption modulator, *Nanophotonics.* 2 (2013) 13–19.

- 
- [29] J.D. Ryckman, K.A. Hallman, R.E. Marvel, R.F. Haglund, S.M. Weiss, Ultra-compact silicon photonic devices reconfigured by an optically induced semiconductor-to-metal transition, *Opt. Express*. 21 (2013) 10753.
- [30] A. Pergament, A. Crunteanu, A. Beaumont, Vanadium Dioxide : Metal-Insulator Transition , Electrical Switching and Oscillations . A Review of State of the Art and Recent Progress, Istanbul, Turkey (2015) .
- [31] K. Liu, S. Lee, S. Yang, O. Delaire, J. Wu, Recent progresses on physics and applications of vanadium dioxide, *Mater. Today*. 21 (2018) 875–896.
- [32] R. Cabrera, E. Merced, N. Sepúlveda, A micro-electro-mechanical memory based on the structural phase transition of VO<sub>2</sub>, *Phys. Status Solidi Appl. Mater. Sci.* 210 (2013) 1704–1711.
- [33] K. Liu, J. Wu, C. Cheng, Z. Cheng, K. Wang, R. Ramesh, J. Wu, Giant-amplitude, high-work density microactuators with phase transition activated nanolayer bimorphs, *Nano Lett.* 12 (2012) 6302–6308.
- [34] B.S. Guiton, Q. Gu, A.L. Prieto, M.S. Gudixsen, H. Park, Single-crystalline vanadium dioxide nanowires with rectangular cross sections, *J. Am. Chem. Soc.* 127 (2005) 498–499.
- [35] J. Cao, E. Ertekin, V. Srinivasan, W. Fan, S. Huang, H. Zheng, J.W.L.L. Yim, D.R. Khanal, D.F. Ogletree, J.C. Grossman, J. Wu, Strain engineering and one-dimensional organization of metal–insulator domains in single-crystal vanadium dioxide beams supplementary, *Nat. Nanotechnol.* 4 (2009) 732–737.
- [36] A. Tselev, E. Strelcov, I.A. Luk’yanchuk, J.D. Budai, J.Z. Tischler, I.N. Ivanov, K. Jones, R. Proksch, S. V. Kalinin, A. Kolmakov, Interplay between ferroelastic and metal-insulator phase transitions in strained quasi-two-dimensional VO<sub>2</sub> nanoplatelets, *Nano Lett.* 10 (2010) 2003–2011.
- [37] S. Lee, K. Hippalgaonkar, F. Yang, J. Hong, C. Ko, J. Suh, K. Liu, K. Wang, J.J. Urban, X. Zhang, C. Dames, S.A. Hartnoll, O. Delaire, J. Wu, Anomalously low electronic thermal conductivity in metallic vanadium dioxide, *Science*. 355 (2017) 371–374.
- [38] H. Guo, M.I. Khan, C. Cheng, W. Fan, C. Dames, J. Wu, A.M. Minor, Vanadium dioxide nanowire-based microthermometer for quantitative evaluation of electron beam heating, *Nat. Commun.* 5 (2014) 1–5.
- [39] J.F. Gómez-Cortés, M.L. Nó, I. López-Ferrenõ, J. Hernández-Saz, S.I. Molina, A. Chuvilin, J.M. San Juan, Size effect and scaling power-law for superelasticity in shape-memory alloys at the nanoscale, *Nat. Nanotechnol.* 12 (2017) 790–796.
- [40] M. Schwartz, ed., *Encyclopedia of Smart Materials*, John Wiley and Sons, Inc., New York, USA (2002) .
- [41] A. Lendlein, R.S. Trask, *Multifunctional materials: concepts, function-structure*

- relationships, knowledge-based design, translational materials research, *Multifunct. Mater.* 1 (2018) 010201.
- [42] R. Vaia, R. Bauer, *Adaptive Composites*, *Science*. 319 (2008) 420–421.
- [43] N. Manca, L. Pellegrino, T. Kanki, S. Yamasaki, H. Tanaka, A.S. Siri, D. Marré, Programmable mechanical resonances in MEMS by localized Joule heating of phase change materials, *Adv. Mater.* 25 (2013) 6430–6435.
- [44] K. Liu, C. Cheng, Z. Cheng, K. Wang, R. Ramesh, J. Wu, Giant-amplitude, high-work density microactuators with phase transition activated nanolayer bimorphs, *Nano Lett.* 12 (2012) 6302–6308.
- [45] A. Lai, Z. Du, C.L. Gan, C.A. Schuh, Shape Memory and Superelastic Ceramics at Small Scales, *Science*. 341 (2013) 1505–1508.
- [46] P.K. Kumar, D.C. Lagoudas, Introduction to Shape Memory Alloys, in: D.C. Lagoudas (Ed.), *Shape Mem. Alloy. Eng. Appl.*, Springer, Boston, USA (2018) 63–90.
- [47] K. Otsuka, C.M. Wayman, *Shape Memory Materials*, Cambridge University Press, Cambridge, UK (1998) .
- [48] L.C. Chang, T.A. Read, Behavior of the elastic properties of AuCd, *Trans Met Soc AIME*. 191 (1951) 47–53.
- [49] W.J. Buehler, J. V. Gilfrich, R.C. Wiley, Effect of Low-Temperature Phase Changes on the Mechanical Properties of Alloys near Composition TiNi, *J. Appl. Phys.* 34 (1963) 1475–1477.
- [50] F.E. Wang, W.J. Buehler, S.J. Pickart, Crystal structure and a unique “Martensitic” Transition of TiNi, *J. Appl. Phys.* 36 (1965) 3232–3239.
- [51] S. Miyazaki, K. Mizukoshi, T. Ueki, T. Sakuma, Y. Liu, Fatigue life of Ti-50 at.% Ni and Ti-40Ni-10Cu (at.%) shape memory alloy wires, *Mater. Sci. Eng. A*. 273–275 (1999) 658–663.
- [52] T. Tadaki, K. Otsuka, K. Shimizu, Shape Memory Alloys, *Annual Review of Materials*, *Science*. 18 (1988) 25–45.
- [53] D.C. Lagoudas, ed., *Shape Memory Alloys*, Springer, New York, USA (2008) .
- [54] S. Seelecke, I. Müller, Shape memory alloy actuators in smart structures: Modeling and simulation, *Appl. Mech. Rev.* 57 (2004) 23–46.
- [55] M. Achenbach, I. Mueller, Simulation of material behaviour of alloys with shape memory, *Arch. Mech. (Poland)*. 37:6 (1985) 573–585.
- [56] C. Liang, C.A. Rogers, One-Dimensional Thermomechanical Constitutive Relations for Shape Memory Materials, *J. Intell. Mater. Syst. Struct.* 1 (1990) 207–234.

- [57] J.G. Boyd, D.C. Lagoudas, Shape Memory Composites, *J. Intell. Mater. Syst. Struct.* 5 (1994) 333–346.
- [58] P. Wollants, M. De Bonte, J. Roos, A thermodynamic analysis of the stress-induced martensitic transformation in a single crystal, *Z. Met.* 70 (1979) 113–117.
- [59] B.C. Wu, H. Wei, B. Ning, Y. Xie, New Vanadium Oxide Nanostructures : Controlled Synthesis and Their Smart Electrical Switching Properties, *Adv. Mater.* 22 (2010) 1972–1976.
- [60] J.D. Budai, A. Tselev, J.Z. Tischler, E. Strelcov, A. Kolmakov, W.J. Liu, A. Gupta, J. Narayan, In situ X-ray microdiffraction studies inside individual VO<sub>2</sub> microcrystals, *Acta Mater.* 61 (2013) 2751–2762.
- [61] D.B. McWhan, M. Marezio, J.P. Remeika, P.D. Dernier, X-ray diffraction study of metallic VO<sub>2</sub>, *Phys. Rev. B.* 10 (1974) 490–495.
- [62] Y.F. Wu, L.L. Fan, S.M. Chen, S. Chen, C.W. Zou, Z.Y. Wu, Spectroscopic analysis of phase constitution of high quality VO<sub>2</sub> thin film prepared by facile sol-gel method, *AIP Adv.* 3 (2013) 042132.
- [63] J.M. Longo, P. Kierkegaard, A refinement of the structure of V<sub>2</sub>O<sub>5</sub>, *Acta Chem. Scand.* 24 (1970) 420–426.
- [64] M. Marezio, Structural Aspects of the Metal-Insulator Transitions in Cr-Doped VO<sub>2</sub>, *Phys. Rev. B.* 5 (1971) 2541–2551.
- [65] G. Andersson, Studies on Vanadium Oxides. II. The Crystal Structure of Vanadium Dioxide, *Acta Chem. Scand.* 10 (1956) 623–628.
- [66] A. Tselev, I.A. Luk'Yanchuk, I.N. Ivanov, J.D. Budai, J.Z. Tischler, E. Strelcov, A. Kolmakov, S. V. Kalinin, Symmetry relationship and strain-induced transitions between insulating M1 and M2 and metallic R phases of vanadium dioxide, *Nano Lett.* 10 (2010) 4409–4416.
- [67] J.H. Park, J.M. Coy, T. Serkan Kasirga, C. Huang, Z. Fei, S. Hunter, D.H. Cobden, Measurement of a solid-state triple point at the metal-insulator transition in VO<sub>2</sub>, *Nature.* 500 (2013) 431–434.
- [68] J.P. Pouget, H. Launois, J.P. D'Haenens, P. Merenda, T.M. Rice, Electron localization induced by uniaxial stress in pure VO<sub>2</sub>, *Phys. Rev. Lett.* 35 (1975) 873–875.
- [69] M. Marezio, P.D. Dernier, A. Santoro, Twinning in Cr-doped VO<sub>2</sub>, *Acta Crystallogr. Sect. A.* 29 (1973) 618–621.
- [70] X. Tan, T. Yao, R. Long, Z. Sun, Y. Feng, H. Cheng, X. Yuan, W. Zhang, Q. Liu, C. Wu, Y. Xie, S. Wei, Unraveling metal-insulator transition mechanism of VO<sub>2</sub> triggered by tungsten doping, *Sci. Rep.* 2 (2012) 1–6.
- [71] M. Ghedira, H. Vincent, M. Marezio, J.C. Launay, Structural aspects of the metal-

- insulator transitions in  $\text{VO}_{0.985}\text{Al}_{0.015}\text{O}_2$ , *J. Solid State Chem.* 22 (1977) 423–438.
- [72] J.M. Atkin, S. Berweger, E.K. Chavez, M.B. Raschke, J. Cao, W. Fan, J. Wu, Strain and temperature dependence of the insulating phases of  $\text{VO}_2$  near the metal-insulator transition, *Phys. Rev. B - Condens. Matter Mater. Phys.* 85 (2012) 1–4.
- [73] S. Zhang, J.Y. Chou, L.J. Lauhon, Direct Correlation of Structural Domain Formation with the Metal Insulator Transition in a  $\text{VO}_2$  Nanobeam, *Nano Lett.* 9 (2009) 4527–4532.
- [74] J.I. Sohn, H.J. Joo, D. Ahn, H.H. Lee, A.E. Porter, K. Kim, D.J. Kang, M.E. Wellandt, Surface-stress-induced Mott transition and nature of associated spatial phase transition in single crystalline  $\text{VO}_2$  nanowires, *Nano Lett.* 9 (2009) 3392–3397.
- [75] V. Eyert, The metal-insulator transitions of  $\text{VO}_2$ : A band theoretical approach, *Ann. Der Phys.* 11 (2002) 650–702.
- [76] H. Guo, K. Chen, Y. Oh, K. Wang, C. Dejoie, S. a Syed Asif, O.L. Warren, Z.W. Shan, J. Wu, a M. Minor, Mechanics and dynamics of the strain-induced M1-M2 structural phase transition in individual  $\text{VO}_2$  nanowires., *Nano Lett.* 11 (2011) 3207–13.
- [77] J.E. Huber, N.A. Fleck, M.F. Ashby, The selection of mechanical actuators, *Proc. R. Soc. London. Ser. A Math. Phys. Eng. Sci.* 453 (1997) 2185–2205.
- [78] K. Kawashima, Y. Ueda, K. Kosuge, S. Kachi, Crystal growth and some electric properties of  $\text{V}_6\text{O}_{13}$ , *J. Cryst. Growth.* 26 (1974) 321–322.
- [79] A. Rúa, F.E. Fernández, N. Sepúlveda, Bending in  $\text{VO}_2$  -coated microcantilevers suitable for thermally activated actuators, *J. Appl. Phys.* 107 (2010) 1–4.
- [80] A. Zylbersztein, N.F. Mott, Metal-insulator transition in vanadium dioxide, *Phys. Rev. B.* 11 (1975) 4383–4395.
- [81] J.B. Goodenough, The two components of the crystallographic transition in  $\text{VO}_2$ , *J. Solid State Chem.* 3 (1971) 490–500.
- [82] N.B. Aetukuri, A.X. Gray, M. Drouard, M. Cossale, L. Gao, A.H. Reid, R. Kukreja, H. Ohldag, C.A. Jenkins, E. Arenholz, K.P. Roche, H.A. Dürr, M.G. Samant, S.S.P. Parkin, Control of the metal-insulator transition in vanadium dioxide by modifying orbital occupancy, *Nat. Phys.* 9 (2013) 661–666.
- [83] M. Abbate, F.M.F. de Groot, J.C. Fuggle, Y.J. Ma, C.T. Chen, F. Sette, A. Fujimori, Y. Ueda, K. Kosuge, Soft-x-ray-absorption studies of the electronic-structure changes through the  $\text{VO}_2$ , *Phys. Rev. B.* 43 (1991) 7263–7266.
- [84] A.X. Gray, J. Jeong, N.P. Aetukuri, P. Granitzka, Z. Chen, R. Kukreja, D. Higley, T. Chase, A.H. Reid, H. Ohldag, M.A. Marcus, A. Scholl, A.T. Young, A. Doran, C.A. Jenkins, P. Shafer, E. Arenholz, M.G. Samant, S.S.P. Parkin, H.A. Dürr,

- Correlation-Driven Insulator-Metal Transition in Near-Ideal Vanadium Dioxide Films, *Phys. Rev. Lett.* 116 (2016) 1–6.
- [85] T. Yao, X. Zhang, Z. Sun, S. Liu, Y. Huang, Y. Xie, C. Wu, X. Yuan, W. Zhang, Z. Wu, G. Pan, F. Hu, L. Wu, Q. Liu, S. Wei, Understanding the nature of the kinetic process in a VO<sub>2</sub> metal-insulator transition, *Phys. Rev. Lett.* 105 (2010) 2–5.
- [86] C. Berglund, H. Guggenheim, Electronic Properties of VO<sub>2</sub> near the Semiconductor-Metal Transition, *Phys. Rev.* 185 (1969) 1022–1033.
- [87] S. Shin, S. Suga, M. Taniguchi, M. Fujisawa, H. Kanzaki, A. Fujimiori, H. Daimon, Y. Ueda, K. Kosuge, S. Kachi, Vacuum-ultraviolet reflectance and photoemission study of the metal-insulator phase transitions in VO<sub>2</sub>, V<sub>6</sub>O<sub>13</sub>, and V<sub>2</sub>O<sub>3</sub>, *Phys. Rev. B.* 41 (1990) 4993–5009.
- [88] N.F. Mott, L. Friedman, Metal-insulator transitions in VO<sub>2</sub>, Ti<sub>2</sub>O<sub>3</sub> and Ti<sub>2-x</sub>V<sub>x</sub>O<sub>3</sub>, *Philos. Mag.* 30 (1974) 389–402.
- [89] J.D. Budai, J. Hong, M.E. Manley, E.D. Specht, C.W. Li, J.Z. Tischler, D.L. Abernathy, A.H. Said, B.M. Leu, L.A. Boatner, R.J. McQueeney, O. Delaire, Metallization of vanadium dioxide driven by large phonon entropy, *Nature.* 515 (2014) 535–539.
- [90] F. Gervais, W. Kress, Lattice dynamics of oxides with rutile structure and instabilities at the metal-semiconductor phase transitions of NbO<sub>2</sub> and, *Phys. Rev. B.* 31 (1985) 4809–4814.
- [91] R. Srivastava, L.L. Chase, Raman spectrum of semiconducting and metallic VO<sub>2</sub>, *Phys. Rev. Lett.* 27 (1971) 727–730.
- [92] P. Schilbe, Raman scattering in VO<sub>2</sub>, *Phys. B Condens. Matter.* 316–317 (2002) 600–602.
- [93] S. Kim, K. Kim, C.J. Kang, B.I. Min, Correlation-assisted phonon softening and the orbital-selective Peierls transition in VO<sub>2</sub>, *Phys. Rev. B - Condens. Matter Mater. Phys.* 87 (2013) 1–5.
- [94] D. Fu, K. Liu, T. Tao, K. Lo, C. Cheng, B. Liu, R. Zhang, H.A. Bechtel, J. Wu, Comprehensive study of the metal-insulator transition in pulsed laser deposited epitaxial VO<sub>2</sub> thin films, *J. Appl. Phys.* 113 (2013) 1–7.
- [95] L.D.S. Diana, F.C. Juan, A.R. Escutia, P.S. Kilders, Ultra-compact electro-absorption VO<sub>2</sub>-Si modulator with TM to TE conversion, *J. Opt. (United Kingdom).* 19 (2017) 1–6.
- [96] H. Kakiuchida, P. Jin, S. Nakao, M. Tazawa, Optical properties of vanadium dioxide film during semiconductive-metallic phase transition, *Japanese J. Appl. Physics, Part 2 Lett.* 46 (2007) 112–116.
- [97] E. Chain, Optical properties of vanadium dioxide and vanadium pentoxide thin

- films, *Appl. Opt.* 30 (1991) 2782–2787.
- [98] R. Balu, P. V. Ashrit, Near-zero IR transmission in the metal-insulator transition of VO<sub>2</sub> thin films, *Appl. Phys. Lett.* 92 (2008) 021904.
- [99] L. Pavesi, D.J. Lockwood, *Silicon Photonics, Volume 1*, Springer, Berlin Heidelberg (2004) .
- [100] G. Lifante, Review of the Electromagnetic Theory of Light, in: *Integr. Photonics Fundam.*, John Wiley & Sons, Inc., New Jersey, USA (2005) 24–51.
- [101] G. Lifante, Theory of Integrated Optic Waveguides, in: *Integr. Photonics Fundam.*, John Wiley & Sons, Ltd, New Jersey, USA (2003) 52–97.
- [102] J.H. Harris, R.K. Winn, D.G. Dalgoutte, Theory and Design of Periodic Couplers, *Appl. Opt.* 11 (1972) 2234.
- [103] G. Lifante, Coupled Mode Theory: Waveguide Gratings, in: *Integr. Photonics Fundam.*, John Wiley & Sons, Ltd, New Jersey, USA (2003) 98–135.
- [104] R.G. Hunsperger, Losses in Optical Waveguides, in: *Integr. Opt. Theory Technol.*, Springer New York, (2002) 93–111.
- [105] F. Ladouceur, L. Poladian, Surface roughness and backscattering, *Opt. Lett.* 21 (1996) 1833.
- [106] A.G. Rickman, F. Reed, G. T. , Namavar, Silicon-on-Insulator Optical Rib Waveguide Loss and Mode Characteristics, *J. Light. Technol.* 12 (1994) 1771–1776.
- [107] C.G. Poulton, C. Koos, M. Fujii, A. Pfrang, T. Schimmel, J. Leuthold, W. Freude, Radiation modes and roughness loss in high index-contrast waveguides, *IEEE J. Sel. Top. Quantum Electron.* 12 (2006) 1306–1320.
- [108] G.H. Jin, J. Harari, L. Joannes, J.P. Vilcot, D. Decoster, Numerical analysis of the radiation losses due to surface roughness in integrated optics devices, *IEEE Photonics Technol. Lett.* 8 (1996) 1202–1204.
- [109] D. Marcuse, Radiation Losses of Dielectric Waveguides in Terms of the Power Spectrum of the Wall Distortion Function, *Bell Syst. Tech. J.* 48 (1969) 3233–3242.
- [110] R. Palmer, *Silicon Photonic Modulators for Low-power Applications*, Ph.D. Thesis, Karlsruhe Institute of Technology (KIT), 2012.
- [111] Y.K. Yap, Electron Beam Physical Vapor Deposition (EBPVD), in: *Encycl. Nanotechnol.*, Springer Netherlands, Dordrecht, Netherlands (2016) 3176–3183.
- [112] K. Strijckmans, R. Schelfhout, D. Depla, Tutorial: Hysteresis during the reactive magnetron sputtering process, *J. Appl. Phys.* 124 (2018) 241101.
- [113] K. Reichelt, X. Jiang, The preparation of thin films by physical vapour deposition

- methods, *Thin Solid Films*. 191 (1990) 91–126.
- [114] M. Ohring, Chapter 6 - Chemical Vapor Deposition, in: *Mater. Sci. Thin Film.*, Academic Press, San Diego (2002) 277–355.
- [115] P. Rai-Choudhury, *Handbook of microlithography, micromachining, and microfabrication*, SPIE Optical Engineering Press, Washington, USA (1997) .
- [116] C.N. Anderson, P.P. Naulleau, Deprotection blur in extreme ultraviolet photoresists: Influence of base loading and post-exposure bake temperature, *J. Vac. Sci. Technol. B Microelectron. Nanom. Struct.* 27 (2009) 6–10.
- [117] M. Manheller, S. Trelenkamp, R. Waser, S. Karthäuser, Reliable fabrication of 3nm gaps between nanoelectrodes by electron-beam lithography, *Nanotechnology*. 23 (2012) 125302.
- [118] N. Pala, M. Karabiyik, e-Beam Lithography, EBL, in: *Encycl. Nanotechnol.*, Springer Netherlands, Dordrecht, Netherlands (2012) 623.
- [119] E. Tolstosheeva, E. Barborini, E.M. Meyer, M. Shafi, S. Vinati, W. Lang, Micropatterning of nanoparticle films by bilayer lift-off, *J. Micromechanics Microengineering*. 24 (2014) 015001.
- [120] A. Sarangan, *Nanofabrication*, in: *Fundam. Appl. Nanophotonics*, Woodhead Publishing, Duxford, UK (2016) 149–184.
- [121] R. Dussart, T. Tillocher, P. Lefauchaux, M. Boufnichel, Plasma cryogenic etching of silicon: From the early days to today’s advanced technologies, *J. Phys. D. Appl. Phys.* 47 (2014) 123001.
- [122] F.O.R. Micro, N. Devices, ICP Etching of Silicon for Micro and Nanoscaled Devices, Ph.D. Thesis, CALIFORNIA INSTITUTE OF TECHNOLOGY, 2010.
- [123] A.P. Nayak, M.S. and Islam, Wet Etching, in: *Encycl. Nanotechnol.*, Springer, Dordrecht, Netherlands (2012) 2829–2830.
- [124] C.W. Dyck, J.H. Smith, S.L. Miller, E.M. Russick, C.L. Adkins, Supercritical carbon dioxide solvent extraction from surface-micromachined micromechanical structures, in: *Proc. SPIE - Int. Soc. Opt. Eng.*, Austin, USA (1996) 225–235.
- [125] D. Number, *Technical Brief Critical Point Drying*, Ashfford, UK (2009) .
- [126] R.W. Collins, Ellipsometry, in: *Encycl. Mater. Sci. Technol.*, Elsevier, Oxford, UK (2001) 2753–2761.
- [127] L.B. Valdes, Resistivity measurements on germanium for transistors, *Proc. IRE*. 42 (1954) 420–427.
- [128] B.A. Uhler, The Potentials of Infinite Systems of Sources and Numerical Solutions of Problems in Semiconductor Engineering, *Bell Syst. Tech. J.* 34 (1954) 105–128.
- [129] D.S. Perloff, Four-Point Probe Correction Factors for Use in Measuring Large

- Diameter Doped Semiconductor Wafers, *J. Electrochem. Soc.* 123 (1976) 1745.
- [130] E.J. Zimney, G.H.B. Dommett, R.S. Ruoff, D.A. Dikin, Correction factors for 4-probe electrical measurements with finite size electrodes and material anisotropy: A finite element study, *Meas. Sci. Technol.* 18 (2007) 2067–2073.
- [131] C.H. Griffiths, H.K. Eastwood, Influence of stoichiometry on the metal-semiconductor transition in vanadium dioxide, *J. Appl. Phys.* 45 (1974) 2201–2206.
- [132] J.F. De Natale, P.J. Hood, A.B. Harker, Formation and characterization of grain-oriented VO<sub>2</sub> thin films, *J. Appl. Phys.* 66 (1989) 5844–5850.
- [133] S. Rastjoo, X. Wang, A. Ludwig, M. Kohl, Top-down fabrication and transformation properties of vanadium dioxide nanostructures, *J. Appl. Phys.* 125 (2019) 225104.
- [134] W. Xiao, Y.A.N. Lu, L.I. Ying, C.A.O. Yun-zhen, Sputtering deposition of VO<sub>2</sub> film using plasma emission monitor as reactive gas flow rate feedback control, *J. Inorg. Mater.* 30 (2015) 1228–1231.
- [135] F. Lambrecht, Development of Shape Memory Alloy - Si Bimorph Nanoactuators, Ph.D. Thesis, Karlsruhe Institute of Technology (KIT), 2016.
- [136] F. Rivera, L. Burk, R. Davis, R. Vanfleet, Electron back-scattered diffraction of crystallized vanadium dioxide thin films on amorphous silicon dioxide, *Thin Solid Films.* 520 (2012) 2461–2466.
- [137] B.Y.S. Timoshenko, Analysis of bi-metal thermostats, *J. Opt. Soc. Am.* 11 (1925) 233–255.
- [138] J. Cao, W. Fan, Q. Zhou, E. Sheu, A. Liu, C. Barrett, J. Wu, Colossal thermal-mechanical actuation via phase transition in single-crystal VO<sub>2</sub> microcantilevers, *J. Appl. Phys.* 108 (2010) 083538.
- [139] P.W. Doll, A. Al-Ahmad, A. Bacher, A. Muslija, R. Thelen, L. Hahn, R. Ahrens, B. Spindler, A.E. Guber, Fabrication of silicon nanopillar arrays by electron beam lithography and reactive ion etching for advanced bacterial adhesion studies, *Mater. Res. Express.* 6 (2019) 65402.
- [140] P. Jin, K. Yoshimura, S. Tanemura, Dependence of microstructure and thermochromism on substrate temperature for sputter-deposited VO<sub>2</sub> epitaxial films, *J. Vac. Sci. Technol. A.* 15 (1997) 1113–1117.
- [141] L.A. Ladd, W. Paul, Optical and Transport Properties of High Quality Crystals of V<sub>2</sub>O<sub>4</sub> Near the Metallic Transition temperature, *Solid State Commun.* 7 (1969) 425–428.
- [142] S.-J. Liu, H.-W. Fang, Y.-T. Su, J.-H. Hsieh, Metal-insulator transition characteristics of Mo- and Mn-doped VO<sub>2</sub> films fabricated by magnetron cosputtering technique, *Jpn. J. Appl. Phys.* 53 (2014) 063201.

- [143] K. Okimura, N. Kubo, Preparation of VO<sub>2</sub> films with metal-insulator transition on sapphire and silicon substrates by inductively coupled plasma-assisted sputtering, *Japanese J. Appl. Physics, Part 2 Lett.* 44 (2005) 1150–1153.
- [144] D. Ruzmetov, K.T. Zawilski, V. Narayanamurti, S. Ramanathan, Structure-functional property relationships in RF-sputtered vanadium dioxide thin films, *J. Appl. Phys.* 102 (2007) 113715.
- [145] R. Lopez, T.E. Haynes, L.A. Boatner, L.C. Feldman, R.F. Haglund, Size effects in the structural phase transition of VO<sub>2</sub> nanoparticles, *Phys. Rev. B.* 65 (2002) 224113.
- [146] J. Du, Y. Gao, H. Luo, L. Kang, Z. Zhang, Z. Chen, C. Cao, Significant changes in phase-transition hysteresis for Ti-doped VO<sub>2</sub> films prepared by polymer-assisted deposition, *Sol. Energy Mater. Sol. Cells.* 95 (2011) 469–475.
- [147] S. Zhou, Y. Li, H. Zhu, R. Sun, Y. Zhang, Y. Huang, L. Li, Y. Shen, Q. Zhen, G. Tong, B. Fang, Microstructures and thermochromic characteristics of low-cost vanadium-tungsten co-sputtered thin films, *Surf. Coatings Technol.* 206 (2012) 2922–2926.
- [148] T.J. Hanlon, J.A. Coath, M.A. Richardson, Molybdenum-doped vanadium dioxide coatings on glass produced by the aqueous sol-gel method, *Thin Solid Films.* 436 (2003) 269–272.
- [149] J. Cao, Y. Gu, W. Fan, L.Q. Chen, D.F. Ogletree, K. Chen, N. Tamura, M. Kunz, C. Barrett, J. Seidel, J. Wu, Extended mapping and exploration of the vanadium dioxide stress-temperature phase diagram, *Nano Lett.* 10 (2010) 2667–2673.
- [150] Y. Gu, J. Cao, J. Wu, L.Q. Chen, Thermodynamics of strained vanadium dioxide single crystals, *J. Appl. Phys.* 108 (2010) 083517.
- [151] D. Natelson, Correlated electron Systems, *News Views.* 4 (2009) 406–407.
- [152] J. Kim, C. Ko, A. Frenzel, S. Ramanathan, J.E. Hoffman, Nanoscale imaging and control of resistance switching in VO<sub>2</sub> at room temperature, *Appl. Phys. Lett.* 96 (2010) 65–68.
- [153] F. Lambrecht, N. Sagardiluz, M. Gueltig, I.R. Aseguinolaza, V.A. Chernenko, M. Kohl, Martensitic transformation in NiMnGa/Si bimorph nanoactuators with ultra-low hysteresis, *Appl. Phys. Lett.* 110 (2017) 213104.
- [154] S.E. Mohny, Y. Wang, M.A. Cabassi, K.K. Lew, S. Dey, J.M. Redwing, T.S. Mayer, Measuring the specific contact resistance of contacts to semiconductor nanowires, *Solid. State. Electron.* 49 (2005) 227–232.
- [155] W.E.T. Al, K. Wang, C. Cheng, E. Cardona, J. Guan, K. Liu, J. Wu, W.E.T. Al, Performance limits of microactuation with vanadium dioxide as a solid engine, *ACS Nano.* 7 (2013) 2266–2272.
- [156] J. Wu, Q. Gu, B.S. Guiton, N.P. De Leon, L. Ouyang, H. Park, Strain-Induced Self

- Organization of Metal – Insulator Domains in, *Nano Lett.* 6 (2006) 2313–2317.
- [157] F. Lambrecht, C. Lay, I.R. Aseguinolaza, V. Chernenko, M. Kohl, NiMnGa/Si Shape Memory Bimorph Nanoactuation, *Shape Mem. Superelasticity.* 2 (2016) 347–359.
- [158] Z. Tian, B. Xu, B. Hsu, L. Stan, Z. Yang, Y. Mei, Reconfigurable Vanadium Dioxide Nanomembranes and Microtubes with Controllable Phase Transition Temperatures, *Nano Lett.* 18 (2018) 3017–3023.
- [159] K.J. Miller, K.A. Hallman, R.F. Haglund, S.M. Weiss, Silicon waveguide optical switch with embedded phase change material, *Opt. Express.* 25 (2017) 26527–26536.
- [160] K. Shibuya, Y. Atsumi, T. Yoshida, Y. Sakakibara, M. Mori, A. Sawa, Silicon waveguide optical modulator driven by metal–insulator transition of vanadium dioxide cladding layer, *Opt. Express.* 27 (2019) 4147–4156.
- [161] A. Joushaghani, B.A. Kruger, S. Paradis, D. Alain, J. Stewart Aitchison, J.K.S. Poon, Sub-volt broadband hybrid plasmonic-vanadium dioxide switches, *Appl. Phys. Lett.* 102 (2013) 061101.
- [162] S.A. Maier, Surface plasmon polaritons at metal/insulator interfaces, in: *Plasmon. Fundam. Appl.*, Springer, New York, USA (2007) 21–37.
- [163] Y. Akimov, M.E. Pam, S. Sun, Kretschmann-Raether configuration: Revision of the theory of resonant interaction, *Phys. Rev. B.* 96 (2017) 1–8.
- [164] M.F. Becker, A.B. Buckman, R.M. Walser, T. Lépine, P. Georges, A. Brun, Femtosecond laser excitation dynamics of the semiconductor-metal phase transition in VO<sub>2</sub>, *J. Appl. Phys.* 79 (1996) 2404–2408.
- [165] A. Ewy, Plasmonic nano-devices based on vanadium dioxide (VO<sub>2</sub>) thin films, Master thesis: Karlsruhe Institute of Technology (KIT), 2019.
- [166] M. Antelius, K.B. Gylfason, H. Sohlström, An apodized SOI waveguide-to-fiber surface grating coupler for single lithography silicon photonics, *Opt. Express.* 19 (2011) 3592–3598.
- [167] S. Muehlbrandt, A.M. Elikyan, T.H. Arter, K.K. Öhnlé, A.M. Uslija, P. V Incze, S.W. Olf, P.J. Akobs, Y.F. Edoryshyn, W.F. Reude, J.L. Euthold, C.K. Oos, M.K. Ohl, Silicon-plasmonic internal-photoemission detector for 40 Gbit/s data reception, *Optica.* 3 (2016) 741–747.
- [168] M. Chicoine, A. Francois, C. Tavares, S. Chevobbe, F. Schiettekatte, V. Aimez, J. Beauvais, J. Beerens, Effects of damage accumulation on quantum well intermixing by low-energy ion implantation in photonic devices, in: *Appl. Photonic Technol.* 6, (2003) 423–431.
- [169] L. V. Rodríguez-de Marcos, J.I. Larruquert, Analytic optical-constant model derived from Tauc-Lorentz and Urbach tail, *Opt. Express.* 24 (2016) 28561–28572.

- [170] B. Fodor, P. Kozma, S. Burger, M. Fried, P. Petrik, Effective medium approximation of ellipsometric response from random surface roughness simulated by finite-element method, *Thin Solid Films*. 617 (2016) 20–24.
- [171] Y. Liu, J. Qiu, L. Liu, Applicability of the effective medium approximation in the ellipsometry of randomly micro-rough solid surfaces, *Opt. Express*. 26 (2018) 16560–16571.